

**AD-A233 958**

ONR-URI Composites Program  
Technical Report No. 90-04

UIUC-NCCMR-90-04

**R-CURVE BEHAVIOR FOR SILICON CARBIDE WHISKER  
REINFORCED ALUMINUM OXIDE COMPOSITES**

Christophe Mangin\*

January, 1990

National Center for Composite Materials Research  
at University of Illinois, Urbana - Champaign  
A DoD University Research Initiatives Center funded by the  
Office of Naval Research, Arlington, VA

---

\* Graduate Research Assistant

91 3 27 105

## I. INTRODUCTION

As a structural material, ceramic matrix composites have received a great deal of interest in recent years. The attention has focused primarily on the increase in mechanical reliability of the composites as compared to that of monolithic ceramics, which are extremely brittle materials. To reduce the brittle nature of these monolithic ceramics in environments where they are used for their mechanical reliability, research efforts have concentrated in the domain of ceramic matrix composites. The basic principle is that to prevent catastrophic crack propagation, other phases must be incorporated into the ceramic matrix that can generate obstacles needed to dissipate the crack energy.

The theoretical approach for processing ceramic matrix composites involves a tradeoff between the two mechanical properties that provide the desired degree of mechanical reliability; fracture strength and fracture toughness. The presence of additional phases, if they contribute to the increase in the fracture toughness of the entire composite, generally tend to decrease the fracture strength. The global challenge stands between a significant increase of the fracture toughness to achieve reduced levels of brittleness, while maintaining the fracture strength of the composite.

Recently, it has been reported that the fracture toughness of  $\text{Al}_2\text{O}_3$  can be significantly improved by the addition of SiC whiskers.<sup>1-2-3</sup> The purpose of this research was to investigate the nature of this improvement in the fracture toughness of these

composites. Specifically, a quantitative determination of the crack growth and resistance (R-curve behavior) was performed. The R-curve behavior of the composite as a function of temperature, whisker content, and whisker nature was emphasized.

## II. LITERATURE SURVEY

### II.A. INTRODUCTION

Structural ceramics are an important class of materials because they possess a diverse array of properties<sup>4</sup>. They can provide a broad range of elastic stiffnesses, fracture strengths approaching theoretical values, high hardnesses necessary for outstanding abrasion resistance, extremes in thermal conductivity from insulators to conductors, excellent chemical stabilities, and high melting temperatures.<sup>5</sup>

Despite their many virtues, most structural ceramics have had their use greatly restricted in severe applications because of their most glaring defect, brittleness, which leads to severe failure. The most costly aspect of making structural ceramics deals with nonreproducibility in manufacturing. Also, since structural ceramics are often difficult to make in complex shapes, production of the final shape may require extensive machining, which is difficult, time consuming, and costly.

Ceramic matrix composites form an active expanding field aimed at decreasing the brittleness of structural ceramics. Major advances will be made in the next few years in high temperature structural materials for use up to 2200°C and in structural materials for reciprocating engines at lower temperatures. Other applications at room temperature will evolve as processing costs decline.

Cutting tool bulk materials are examples of such applications that are now in the market place.<sup>6</sup> The introduction of SiC whiskers in  $\text{Al}_2\text{O}_3$  cutting tools creates a superiority, compared to unreinforced  $\text{Al}_2\text{O}_3$ , in wear resistance and fracture toughness, especially in the machining of ferrous and nonferrous metals (see TABLE 1). SiC whisker/ $\text{Al}_2\text{O}_3$  matrix composite cutting tools have substantially increased metal removal rates in machining Ni-based superalloys. Yet, SiC whisker/ $\text{Al}_2\text{O}_3$  matrix composite cutting tools seem to be noncompetitive compared to Sialon cutting tools for the machining of gray cast iron and 1045 and 4340 steels.<sup>7</sup>

## II.B. RAW MATERIALS

The key to successful fabrication of ceramic matrix composites involves controlling the nature of the interface between the fiber and matrix. The matrix must be thermochemically compatible with the fiber and any coatings employed. The appropriate bond strength for activation of strengthening and/or toughening mechanisms must be developed at the interface. Much chemical interaction can occur at the fiber/matrix interface, which strongly influences the resultant bond strength attained. The choice of the ceramic matrix also determines the level of thermal expansion mismatch with a given ceramic fiber. The resulting thermomechanical stresses can effectively enhance or reduce the mechanical bonding.

TABLE 1  
Field Test of Cutting Tool Materials (from Ref. 8)

Parameter	Al <sub>2</sub> O <sub>3</sub>	SiC/Al <sub>2</sub> O <sub>3</sub>
Insert style	RNG-45	RNG-45
Workpiece diameter (mm)	152.4	152.4
Depth of cut by length of cut (mm)	2.5 by 135.9	2.5 by 135.9
Feed rate (mm per revolution)	0.18	0.13
Cutting speed (m/s)	4.6	4.8
Cutting time per piece (min)	0.66	0.75
Pieces per edge	1	3
Tool life per edge (min)	0.66	2.25
Reason for indexing	Chipping	Chipping
Total cost per piece (insert plus machine) (\$)	4.99	1.34
Estimated saving (%)		73

## II.B.1. Aluminum Oxide Powder

### II.B.1.a. Definition and Nomenclature of Aluminum Oxide

The term alumina is used rather indefinitely to denote (1) aluminum containing materials of all types taken collectively, (2) the anhydrous and hydrous aluminum oxides taken indiscriminately, (3) more frequently, the calcined or substantially water free aluminum oxides, without distinguishing the phases present, or (4) corundum or alpha aluminum oxide, specifically. Alumina is often used interchangeably with the molecular formula,  $\text{Al}_2\text{O}_3$ . Corundum, emery, sapphire, and ruby are more or less pure forms found in nature and known from antiquity as abrasives and gem stones. All consist of the phase designated  $\alpha\text{-Al}_2\text{O}_3$ <sup>8</sup>. In TABLE 2 a summary of the available nomenclature of crystalline aluminas is presented.

### II.B.1.b. Processing and Characterization of Aluminum Oxide Powder

The principal sources of  $\alpha\text{-Al}_2\text{O}_3$  are a native corundum and a manufactured form derived from bauxite. The principal methods for preparing  $\alpha\text{-Al}_2\text{O}_3$  are; calcination of the aluminum hydroxides, transition aluminum oxides, and aluminum salts and solidification from melts. The most important method for preparing  $\alpha\text{-Al}_2\text{O}_3$  for ceramic purposes, as well as for metallic applications, is calcination of Bayer aluminum trihydrate.  $\alpha\text{-Al}_2\text{O}_3$  can be prepared in a wide range of properties insofar as they are affected by crystal size,

TABLE 2  
Nomenclature of Crystalline Aluminas (from Ref. 8)

Mineralogical Name	Phase or Form Name				
	Symposium	Alcoa	Haber	British	French
<b>Hydroxides</b>					
Gibbsite	$\text{Al}(\text{OH})_3$	$\alpha\text{-Al}_2\text{O}_3 \cdot 3\text{H}_2\text{O}$	$\gamma\text{-Al}(\text{OH})_3$	$\gamma\text{-Al}_2\text{O}_3 \cdot 3\text{H}_2\text{O}$	
Hydrargillite					
Bayerite	$\text{Al}(\text{OH})_3$	$\beta\text{-Al}_2\text{O}_3 \cdot 3\text{H}_2\text{O}$	$\gamma\text{-Al}(\text{OH})_3$	$\gamma\text{-Al}_2\text{O}_3 \cdot 3\text{H}_2\text{O}$	
Nordstrandite	$\text{Al}(\text{OH})_3$				
Randomite					
Bayerite II					
Boehmite	$\text{AlOOH}$	$\alpha\text{-Al}_2\text{O}_3 \cdot \text{H}_2\text{O}$	$\gamma\text{-AlO}_2\text{H}$	$\gamma\text{-Al}_2\text{O}_3 \cdot \text{H}_2\text{O}$	
Diaspore	$\text{AlOOH}$	$\beta\text{-Al}_2\text{O}_3 \cdot \text{H}_2\text{O}$	$\alpha\text{-AlO}_2\text{H}$		
<b>Aluminas</b>					
	$\chi$	$\chi$		$\chi+\gamma$	$\chi+\gamma$
	$\epsilon$	$\epsilon$		$\gamma$	$\epsilon$
	$\gamma$	$\gamma$	$\gamma$	$\delta$	$\gamma$
	$\delta$	$\delta$		$\delta+\tau$	$\delta$
	$\kappa$	$\kappa$		$\kappa+\tau$	$\kappa+\delta$
Corundum	$\alpha$	$\alpha$	$\alpha$	$\alpha$	$\alpha$
Sapphire					



crystal habit, and purity. Crystal sizes within a range from about 0.03  $\mu\text{m}$  to 30,000  $\mu\text{m}$  or more have been available commercially.<sup>8</sup>

The conventional way to make fine powders is to grind a bulk material and pass it through a fine sieve. A problem with this approach is that, although the powders may be relatively fine, they may not be uniform in size. Furthermore, the very act of grinding the material may introduce metallic or ceramic impurities.

Another method for making pure, superfine, uniformed sized powders is the sol-gel process. As far back as 1941, Körösy<sup>9</sup> used this method to produce glasses. Roy et al.<sup>9</sup> pioneered the use of this technique to make finely divided powders and exceptionally homogeneous glasses of silica and the oxides of aluminum, magnesium, titanium, zirconium, germanium, and other metals. But it was not until researchers at Oak Ridge National Laboratory<sup>10</sup> in the middle 1960s found that the method could be used to make  $\text{ZrO}_2$  pellets for nuclear reactors that the process gained its first large scale industrial use.

The sol-gel method involves the conversion of a sol (a fluid colloidal dispersion of a solid in a liquid) to a gel (a semirigid colloidal suspension of a solid in a liquid). In one typical procedure, a metal is reacted with an alcohol to form a metal alkoxide. The metal alkoxide then is dissolved in an appropriate alcohol. Next, water is added to cause the alkoxide to hydrolyze. After the pH of the solution is adjusted, the material condenses to form a gel. The gel consists of loosely bonded material and a liquid (water and alcohol). This material is heated carefully at 200°C to 500°C to remove the liquid. This converts the gel to a finely divided metal

oxide powder, with particle sizes in the range of 0.003  $\mu\text{m}$  to 0.1  $\mu\text{m}$ . This method can produce extremely homogeneous mixtures of two or more components because the mixing of the ingredients takes place at the atomic level in a liquid rather than in the solid state.

In addition to the sol-gel process, PPG Industries<sup>9</sup> has developed a plasma arc process for making high-purity  $\text{TiB}_2$  powders. Hydrogen gas at atmospheric pressure is passed through a high-voltage electric arc and then ionized at about 2500°C. The resulting hydrogen plasma is directed into a chamber where it quickly heats the gaseous reactants,  $\text{TiCl}_2$  and  $\text{BCl}_3$ , to form  $\text{TiB}_2$ , along with  $\text{HCl}$ . As the products cool rapidly, the  $\text{TiB}_2$  crystallizes out in submicron particles. The process of PPG Industries also has been used to produce  $\text{SiC}$ ,  $\text{Al}_2\text{O}_3$ ,  $\text{TiC}$ ,  $\text{WC}$ , and other powders.

## II.B.2. SiC Whiskers

### II.B.2.a. Introduction

Among the ceramic whiskers of greatest interest are those made of  $\text{SiC}$ . In the early 1970s, Cutler<sup>9</sup> developed a process for growing such whiskers by heating rice hulls, which are excellent sources of silicon and carbon, to nearly 2000°C. In 1976, Cutler sold his process to Exxon Enterprises and Hulco Inc. The joint effort, called Silag Inc., resulted in a plant at Greer, S.C., designed solely to make  $\text{SiC}$  whiskers commercially. In 1982, Arco Metals purchased the company, renamed it Arco Metals/Silag Operation, and since then has been producing  $\text{SiC}$  whiskers under the tradename Silar.

Other organizations likewise make ceramic whiskers. Nippon Carbon Co. manufactures SiC whiskers by pyrolyzing rice hulls. Los Alamos National Laboratory is developing a different process for making SiC whiskers. Versar Inc. produces whiskers of SiC and  $\text{Al}_2\text{O}_3$  and Boeing makes whiskers of  $\text{Si}_3\text{N}_4$ .

## II.B.2.b. Processing and Characterization of SiC Whiskers

### II.B.2.b.1. The Pyrolysis Process

SiC whiskers can be made by a potentially inexpensive process involving the pyrolysis of silicon and carbon produced from ground rice hulls. The whiskers exhibit a number of polytypes which are variations of a one dimensional stacking sequence of closed packed layers. Considerable planar disorder is frequently observed, resulting in a range of planar defect densities and a mixture of structural types. The fringe spacing rarely repeats more than once or twice in any location<sup>10</sup>, indicating an almost random stacking sequence. The layers are extremely thin and the interplanar spacings of polytypes are quite similar. When viewed in the axial direction, the whiskers frequently exhibit a large number of partial dislocations. These defects typically appear in the shape of a "V" or "U" oriented such that the arms extend away from the core region to the whisker periphery. Many of the whiskers contain small cavities which vary in size, number, and distribution from whisker to whisker. Cavities range in size from 1 nm to 20 nm, although the cavity sizes usually do not vary so widely in any single whisker. In

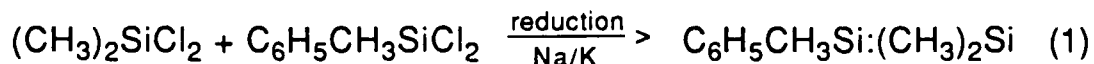
most whiskers, the cavities are located in the core region. The cavities could arise from the entrapment of gases evolved during a rapid growth period.<sup>11</sup> Subsequent lateral growth at slower rates might then account for the absence of cavities outside the whisker core regions. Both the partial dislocations and the cavities are undoubtedly formed during the growth process and they appear to be mutually associated.

In the case of the SiC whiskers produced by Arco Metals<sup>12</sup>, morphological characterization of the whiskers indicated a broad range of both lengths and diameters. Clusters within the whiskers and irregular, serrated-edged whiskers were found to be regular features. The average length and diameter were 17.5  $\mu\text{m}$  and 0.5  $\mu\text{m}$ , respectively.<sup>12</sup> The whiskers had a high density of planar faults lying in close packed planes perpendicular to the growth axis. These faults resulted in a complex arrangement of thin layers of the  $\alpha$  and  $\beta$  polytypes normal to the whisker axis. Furthermore, the core region was generally observed to contain a high density of impurities and/or cavities. The absence of these impurities and/or cavities along the outer periphery and top end of the whiskers indicated a two stage growth process similar to that generally observed in a vapor-liquid-solid process.

#### II.B.2.b.2. The Organic Process

Mazdiyasni et al.<sup>13</sup> used polysilazane and polyphenylmethylsilazane to infiltrate reaction bonded  $\text{Si}_3\text{N}_4$  and in the process synthesized  $\text{Si}_3\text{N}_4$  and SiC, respectively, in the powder

and whisker forms. The specific mixture used to form  $\beta$ -SiC whiskers was prepared by adding a small amount of phenylmethyl-dichlorosilane to dimethyldichlorosilane in tetrahydrofuran solution and then reducing with a Na/K alloy for 36 hours. This process yielded a polymer by the reaction:



The reaction mixture was chilled with hexane and slowly and carefully treated with water to yield 96 percent polymer, which was a gum or meltable resinous material. The phenylmethylsilane was thermally decomposed into a highly transparent greenish black mixture of straight whiskers with no beads or whiskers in a rosary bead morphology. Most whiskers were free of any amorphous coating and had one dimensional disorder with a strong  $\beta$ -SiC component. Energy dispersive X-ray analysis indicated occasional traces of one or more of the elements Al, Na, K, and Ca. From TEM observations, beads contained large amounts of oxygen and probably no carbon. The synthesis of SiC whiskers produced by thermal conversion of any polymeric organosilicon precursor is subject to impurity carryover from the chemical reactions (Na,K), solvent drying agents (Ca,Mg), and refractory container material used at high temperatures (Al).<sup>14</sup> Alkali metals and alkali earth metals in the presence of halogen and carboneous atmospheres will cause rapid SiO diffusion by vapor transport with the subsequent formation of low temperature silicate glasses. Polymer derived fibers also suffer from rapid

diffusion through their open low density amorphous structure and from high reactivity with the atmosphere.

#### II.B.2.b.3. The VLS Process

$\beta$ -SiC whiskers have also been grown by a vapor-liquid-solid (VLS) process, which produced a very high purity, high strength single crystal whisker about 6  $\mu\text{m}$  in diameter and 5 mm to 100 mm long.<sup>15</sup> X-ray diffraction (XRD) confirmed the whiskers to be pure  $\beta$ -SiC with growth in the  $\langle 111 \rangle$  direction. They exhibited a smooth surface, a rounded-triangular cross section, and a light green color.

In the VLS process, V stands for Vapor feed gases, L for Liquid catalyst, and S for Solid crystalline whisker growth. The role of the catalyst is to form a liquid solution interface with the crystalline material to be grown and feed from the vapor through the liquid-vapor interface. The catalyst solution is a preferred site for deposition of feed from the vapor which causes the liquid to become supersaturated. Crystal growth occurs by precipitation from the supersaturated liquid at the solid-liquid interface. In view of this mechanism, catalyst selection is partially based upon the fact that the catalyst must display the affinity, when molten, to take into solution the constituent atoms of the whisker to be grown. The catalyst must be a material that forms a eutectic system in which SiC has a primary crystallization field. For SiC whisker growth, transition metals and iron alloys satisfy this requirement. At approximately 1400°C the solid catalyst particle melts and forms the liquid catalyst ball. Carbon and silicon atoms in the vapor feed

are accreted to the surface by the liquid catalyst, which soon becomes supersaturated, and solid SiC precipitates from the liquid catalyst onto the growth substrate. As precipitation continues, the whiskers grow, lifting the catalyst ball from the substrate and forming a whisker which is proportional in size to the catalyst ball. It is also possible to control the whisker diameter because a fixed size relationship exists between it and the droplet. By manipulating the gas phase composition and the degree of supersaturation, significant control can be exercised over the growth of the SiC whiskers.

In the Los Alamos VLS process<sup>15</sup>, the SiC whiskers are grown on parallel plates of graphite that have been previously coated with a uniform dispersion of sized catalyst particles (30  $\mu\text{m}$  type 304 stainless steel). These plates are placed in a graphite reactor that contains a gas manifold for the uniform distribution of the methane-hydrogen gases. The SiO is generated by the following reaction:



This is accomplished by placing sections of porous insulation brick, which have been impregnated with a fine powder mixture of  $\text{SiO}_2$  and carbon, into the reactor. To moderate and control the rate of release of SiO, CO is added to control the active gaseous species supersaturation level and to stimulate the VLS reaction. Once prime whiskers are nucleated, they do not decrease in diameter even though the liquid/solid wetting angle decreases with increasing C/Si ratio in the droplet.

VLS processed  $\beta$ -SiC whiskers have been evaluated for their tensile mechanical properties by Petrovic et al.<sup>16</sup> The VLS processed whiskers exhibited superb mechanical properties. An average fracture strength of 8.4 GPa at 5 mm gauge length with a Young's modulus of 580 GPa were considerably stronger and stiffer than continuous fibers. The whiskers also had excellent stability and compatibility with matrices at high temperatures.<sup>17</sup>

Tensile fracture from an internal defect allowed measurement of the fracture toughness,  $K_{IC} = 3.23 \text{ MPa m}^{1/2}$ , and fracture surface energy,  $\gamma = 9.06 \text{ J/m}^2$ , for a single crystal  $\beta$ -SiC whisker with  $\langle 111 \rangle$  crystallographic orientation in the tensile direction<sup>16</sup>. From a fracture mechanics viewpoint, this phenomenon may be viewed at first approximation as fracture in tension from an internal penny-shaped flaw. For fracture of an internal penny-shaped flaw in an infinite medium in uniaxial tension, the fracture toughness,  $K_{IC}$ , is given by:

$$K_{IC} = \frac{2}{\pi} \sigma_F (\pi a)^{1/2} \quad (3)$$

where  $\sigma_F$  is the fracture stress and  $a$  is the flaw radius.<sup>§</sup> The fracture surface energy,  $\gamma$ , may be calculated from the relation (plane-stress conditions):

---

§ Similarly, the fracture toughness for a penny-shaped flaw in a finite round solid rod in tension is:  $K_{IC} = F_1(\frac{a}{b}) \sigma_F(\text{net}) (\pi a)^{1/2}$ ;  $\sigma_F(\text{net}) = \frac{P_F}{\pi(b^2 - a^2)}$ ;  $F_1(\frac{a}{b}) = (1 - \frac{a}{b})^{1/2} G(\frac{a}{b})$ ;  $G(\frac{a}{b}) = \frac{2}{\pi} [ 1 + \frac{1}{2} \frac{a}{b} - \frac{5}{8} (\frac{a}{b})^2 + 0.421 (\frac{a}{b})^3 ]$  where  $b$  is the radius of the rod and  $P_F$  is the fracture load.



$$\gamma = \frac{K_{IC}^2}{2E} \quad (4)$$

where E is the Young's modulus.

## II.C. PROCESSING OF WHISKER REINFORCED CERAMIC MATRIX COMPOSITES

Traditionally, the production of most structural ceramics has involved four basic steps; powder preparation, forming, densification, and finishing. Powder preparation is crucial for advanced structural ceramics because particle sizes and size distributions must be carefully controlled to produce a material with uniform density and specific flaw size. Thus, the trend in research on structural ceramics has been to move to smaller (submicron) and more uniform particle sizes.

The newer powder preparation techniques involve colloidal methods. These processes have been used to make whisker reinforced composites. The processing method, called coarcervation, involves suspending submicron sized particles of two distinct materials in a liquid and then changing the chemistry of the liquid phase to precipitate an intimate mixture of the two materials.<sup>18</sup> Soft agglomerates can be broken apart with surfactants. The size of hard agglomerates can be reduced to a desired level by sedimentation of the powder in a liquid in suspension. It is well known that flocculated suspensions redisperse at high shear rates. High shear rates can be achieved

using either ultrasonics or special stirrers.<sup>19</sup> But prolonged ultrasonic mixing without stirring can cause segregation.

The most investigated ceramic matrix composite to date has been based on  $\text{Al}_2\text{O}_3$  matrices reinforced with SiC whiskers. Important characteristics of the available  $\text{Al}_2\text{O}_3$  powders are shown in TABLE 3. SiC whiskers are perhaps the most promising reinforcement so far, since they retain their high strength up to at least  $1600^\circ\text{C}$ .<sup>20</sup> The stability of SiC whiskers in the  $\text{Al}_2\text{O}_3$  matrices during the processing at temperatures up to  $1900^\circ\text{C}$  is remarkable. SiC whiskers are very stable at elevated temperatures because they are single crystals and, therefore, do not degrade at temperatures greater than  $1200^\circ\text{C}$  by the grain growth that commonly occurs in microcrystalline continuous SiC fibers. Stability is also enhanced because they have a very low oxygen content which, if present, could react with the SiC, resulting in decomposition of the whiskers.<sup>21</sup>

Scanning electron microscopy studies of various whiskers usually reveal that the whiskers contain particulate material both in the form of large irregular crystals and in the form of large bundles of fibers.<sup>20</sup> These particles act as defects in ceramic matrix composites. The goal is to eliminate those defects before starting the processing of the composite by a sedimentation-flocculation technique. The purpose is to remove large particles and agglomerates by sedimentation without recreating agglomerates during drying of the processed whiskers. The whiskers are first dispersed at high zeta potential (positive or negative) and then flocculated in the pH range where the zeta potential is close to zero.

TABLE 3  
Characterization of  $\text{Al}_2\text{O}_3$  Matrix Powders (from Ref. 22)

Manufacturers	Types of $\text{Al}_2\text{O}_3$	Median Particle Size ( $\mu\text{m}$ )	Surface Area ( $\text{m}^2/\text{g}$ )
Alcoa	A-16-SG	0.73	6.5
Alcoa	XA-139-SG	0.66	
Reynolds Chemicals	RC-HP DBM	0.48	7.5
Baikowski	CR-10	1.06	10
Baikowski	CR-30	1.65	30
Philadelphia Quartz Co.	Dispal M	0.04-1.0	>200

The sedimentation time for particles with a certain size can be calculated using Stoke's equation:

$$v = \frac{2r^2 (\rho_s - \rho_l) g}{9\eta} \quad (5)$$

where  $v$  is the stationary state sedimentation velocity,  $\rho_s$  is the density of the solid,  $\rho_l$  is the density of the liquid,  $\eta$  is the liquid viscosity, and  $r$  is the equivalent spherical radius. Sedimentation is subsequently carried out for the calculated time, after which the supernatant liquid is syphoned off. The different whisker size fractions are then individually flocculated at the appropriate pH. The flocculated whiskers form a loose sediment, which is dewatered by centrifuging. This flocculated sediment can be stored wet, since hard agglomerates will only form if the whiskers are completely dried. It is possible by this method to obtain a whisker fraction free from both fine and coarse particulate material.

The liquid processing technique was utilized by Homeny and Vaughn<sup>3</sup> to produce composites from SiC whisker (30 volume percent) and  $\text{Al}_2\text{O}_3$  powder mixtures. First, the  $\text{Al}_2\text{O}_3$  powder and SiC whiskers were added to deionized water. While stirring, the pH was adjusted to greater than 10 with  $\text{NH}_4\text{OH}$  to deflocculate the slurry. The slurry was then ultrasonically dispersed. While stirring, the pH was then reduced to 7 with  $\text{HNO}_3$  to flocculate the slurry. Next, the slurry was simultaneously heated and stirred to increase the total solids content through evaporation of the water. The resulting

viscous mass was dried and hot pressed at 1900°C at 31.2 MPa for 60 minutes under an ultrahigh purity argon atmosphere.

If a sintering aid is incorporated into the composite, such as MgO or  $Y_2O_3$ , at sintering temperatures of 1700°C-1800°C a liquid phase was formed, which aids densification. Becher et al.<sup>22</sup> showed that there is no reaction between the whiskers and the liquid phases during pressureless sintering. They also demonstrated that lowering the aspect ratio of the whiskers and/or using smaller diameter  $Al_2O_3$  powders increased the packing efficiency and improved the green density. The sintered densities generally decreased with increasing SiC whisker content. During sintering, the whiskers were essentially lying in planes parallel to one another, which permitted shrinkage of the compacts and reduced inhibition to the rearrangement of the whiskers.

The procedure introduced by Porter et al.<sup>23</sup> involved mixing components as dispersed slurries, press filtration of the slurries to produce green bodies, and hot pressing the green bodies in close fitting graphite dies (see TABLE 4). Grain growth inhibitors were not necessary, as the SiC whiskers acted to inhibit abnormal grain growth. A 3 weight percent  $Al_2O_3$  dispersion in water at pH 2 and a 5 weight percent dispersion of whiskers in water at pH 11 were separately ultrasonicated and allowed to settle for 10 minutes and 24 hours, respectively. Processing flaws, such as whisker clumps and agglomerates of matrix grains, were eliminated in the final product. The final microstructure contained a uniform distribution of whiskers within the matrix.

TABLE 4

Effect of Filtration Pressure and Slurry pH on Green Density and Final Density of Composites with 15 weight percent Whisker Loading (from Ref. 23)

Filtration	Slurry pH	Filtration Pressure (MPa)	Green Density (%)	Final Density (%)
2		7.8	35	99.5+/- 0.5
2		7.8	59	
2		0.78	60	

It is important to achieve full density in ceramic matrix composites. Porosity is generally detrimental since it (1) provides paths for environmental attack, (2) lowers the matrix fracture strength and fracture toughness, and (3) potentially results in reduced reinforcement/matrix interfacial area for load transfer.

The development of hot pressed SiC whisker reinforced  $\text{Al}_2\text{O}_3$  has resulted in composites with fracture toughness values  $\approx 8.7 \text{ MPa}\cdot\text{m}^{1/2}$  at 20 volume percent SiC whiskers.<sup>3</sup> Whisker orientation during processing leads to anisotropy in both fracture toughness and fracture strength. Fracture strengths are also limited by the ability to disperse the SiC whiskers, however, use of both fine  $\text{Al}_2\text{O}_3$  powders and ultrasonic dispersion techniques yields strengths  $\approx 800 \text{ MPa}$ . Becher and Wei<sup>1</sup> obtained fully dense composites with fine grained matrices ( $\leq 4\mu\text{m}$ ) by hot pressing a mixture of  $\text{Al}_2\text{O}_3$  powder containing 20 volume percent SiC whiskers at  $1850^\circ\text{C}$ . Because of the high average aspect ratios ( $30 \mu\text{m}$  long by  $0.7 \mu\text{m}$  diameter) of the whiskers, hot pressing caused the whiskers to be oriented with the length of the whisker essentially randomly oriented in the plane perpendicular to the hot pressing axis. The dispersibility of the SiC whiskers was improved both by ultrasonic dispersion techniques and by the use of finer  $\text{Al}_2\text{O}_3$  particles. The densification rate during the final stage of hot pressing depended on the hot pressing temperature and pressure. As expected in all cases, the average SiC whisker lengths were reduced<sup>12</sup> from  $17.5 \mu\text{m}$  in the as received condition to about  $5 \mu\text{m}$  in the hot pressed material. Since sheared or fractured SiC whiskers were generally not observed in the consolidated structure, it can be assumed that most of the whiskers fractured

during the powder processing cycle. No evidence of interfacial reaction at the SiC whisker/ $\text{Al}_2\text{O}_3$  matrix interface was observed. A continuous, thin glass phase was found along the whisker/matrix interface. This amorphous phase was clearly visible by utilizing a special dark field imaging technique and also when the whisker/matrix interface was approximately parallel to the incoming beam. Appropriate tilting experiments clearly indicated a continuous amorphous film around the periphery of the SiC whisker/matrix interface. The interfacial film was due to the presence of an oxide rich layer on the surface of the as received SiC whiskers.

## II.D. FRACTURE MECHANICS CONSIDERATIONS

### II.D.1. Introduction

It is desirable to design ceramic microstructures with improved resistance to fracture and hence some tolerance to defects. In ceramic matrix composites, the fibers are added with the aim of increasing the fracture toughness, sometimes at the expense of the fracture strength. The most severe strength degradation is caused by matrix/interface cracks. Cracks generally originate from stress concentrations. Elastic contact damage is most likely to occur in service as a result of mechanical attachment or sliding/rolling contact. Damage in these applications can be minimized by increasing the contact area, decreasing the friction coefficient, and increasing the fracture toughness. When the



thermal contraction of the inclusion during cooling is larger than that of the matrix, the inclusion experiences residual tension and cracking occurs either across the inclusion or at the interface of the matrix and inclusion.<sup>24</sup> The size, shape, orientation, and spatial distribution of the constituent phases all play a large role in the resulting properties and provide parameters which can be varied in order to optimize the behavior of the composite. Moreover, the nature of the interfaces (chemical and mechanical) greatly influences properties and response, especially under dynamic loading conditions or under severe chemical or thermal environments.

In all ceramic matrix composites, the failure strain of the reinforcing fiber ( $\epsilon \approx 1-1.5\%$ ) is much greater than that of the matrix (0.1-0.2%). Therefore, under an applied stress the matrix will *always fail first*.<sup>25</sup> The critical point on the composite stress-strain curve is the point of first matrix microcracking, sometimes referred to as the microcrack yield stress or the proportional limit. Below this point, the composite does not in general exhibit environmental interaction and degradation.

Certainly, it is now universally recognized that the nature of the fiber/matrix interface is the main determinant of ceramic matrix composite behavior. The degree of toughness in a composite is commonly qualitatively judged in terms of the fiber pullout length, as this is related to the interfacial bonding. If a coating is applied to the fiber, it must be multifunctional, in that it must provide the necessary bond strength and oxidation resistance, while acting as a barrier to the diffusion of elements detrimental to the fiber and matrix.

Whisker reinforcement has the potential for improving high temperature mechanical properties of structural ceramics. Microcracking, fiber debonding, and especially whisker pullout are key contributors to the fracture toughness. Whisker/matrix bonding must be limited and, generally, chemical bonding must be avoided to have good fracture toughness. A very important aspect of the whisker/matrix bonding is the effect of exposure at high temperatures, due to sintering effects and chemical interaction between the whisker and the matrix, as well as effects of high temperature environment, e.g., oxidation. Important among these are the use of various coatings on whiskers to vary their degree of bonding and possibly to allow use of greater whisker/matrix property differences, as well as otherwise chemically reactive whisker/matrix combinations.

#### II.D.2. Definitions and Comments on Fracture Mechanics Parameters

##### II.D.2.a. Strain Energy Density Factor

In most structural components, the flaws or cracks are seldom aligned perpendicular to the direction of loading. If the stress state is triaxial in nature, it must be described by at least three parameters;  $k_1$ ,  $k_2$ , and  $k_3$ .<sup>26</sup> It should be emphasized that the effect of misalignment between the crack and the applied load could lead to serious errors in the prediction of the fracture strength. A more general treatment of the fracture mechanics problem is needed. This treatment assumes that the material in the immediate vicinity

of the crack tip is free from defects of the same order of magnitude as the crack tip radius and that the defects are distributed uniformly throughout the material outside the core region of radius  $r_0$ .

The amount of energy stored in one of these defects can be expressed by:

$$\frac{dW}{dA} = \frac{1}{r} (a_{11}k_1^2 + 2a_{12}k_1k_2 + a_{22}k_2^2 + a_{33}k_3^2) \quad (6)$$

$$a_{11} = \frac{1}{16\mu} (3-4\nu-\cos\theta) (1+\cos\theta)$$

$$a_{12} = \frac{1}{16\mu} (2\sin\theta) [\cos\theta - (1-2\nu)]$$

$$a_{22} = \frac{1}{16\mu} [4(1-\nu)(1-\cos\theta) + (1+\cos\theta)(3\cos^2\theta-1)]$$

$$a_{33} = \frac{1}{4\mu}$$

where  $r$  is the radius coordinate,  $\nu$  is defined as the Poisson's ratio,  $\mu$  is defined as the shear modulus of elasticity,  $\theta$  is defined as the angular coordinate of the defect, and  $\frac{dW}{dA}$  is the local strain energy density function.

The intensity of this energy field, which varies along the periphery of circle  $r = r_0$ , will be denoted by  $S$  and referred to as the strain energy density factor:

$$S = a_{11}k_1^2 + 2a_{12}k_1k_2 + a_{22}k_2^2 + a_{33}k_3^2 \quad (7)$$

Equation (7) requires two assumptions. First, crack initiation is assumed to take place in a direction determined by the stationary value of the strain energy density factor, as shown below:

$$\frac{\partial S}{\partial \theta} = 0 \text{ at } \theta = \theta_0 \quad (8)$$

Second, crack extension is assumed to occur when the strain energy density factor reaches the critical value defined below:

$$S_c = S(k_1, k_2, k_3) \text{ for } \theta = \theta_0 \quad (9)$$

where  $S_c$  is also a measure of the resistance of a material against fracture.  $S_c$  determines simultaneously the fracture toughness of the material and the direction of crack initiation.

The physical meaning of  $S_c$  can best be explained by resolving the strain energy density factor into two component parts, one part associated with the change in volume and the other part associated with the distortion or change in shape of the volume element:

$$S = S_v + S_d \quad (10)$$

where  $S_v$  is the energy density of volume change:

$$S_v = b_{11}k_1^2 + 2b_{12}k_1k_2 + b_{22}k_2^2 + b_{33}k_3^2 \quad (11)$$

and  $S_d$  is the energy density of distortion:

$$S_d = c_{11}k_1^2 + 2c_{12}k_1k_2 + c_{22}k_2^2 + c_{33}k_3^2 \quad (12)$$

according to the fact that  $a_{ij} = b_{ij} + c_{ij}$ .

This approach provides a simple procedure for providing the worst crack at a given stress level without causing fracture. The basic idea is to keep the worst crack below a certain size so that design can proceed on the basis of a known allowable stress.

#### II.D.2.b. Fracture Toughness and Stress Intensity Factor

The existing theories of fracture mechanics are theoretically limited to brittle fracture where the surfaces after material separation have a smooth appearance denoting low energy absorption during crack propagation. Thus far, there exists no suitable theory to explain ductile fracture characterized by fracture surfaces with a rough and fibrous appearance.

The stress concentration factor,  $K$ , is not a criterion of failure, but merely indicates the ratio of the elevation of the local stress to that of the applied stress.  $K_c$  is usually assigned to represent  $\sigma_c \sqrt{\pi a}$  from the Griffith theory and is called the fracture toughness of the material. The quantity  $K_c$  can be interpreted as the critical value of the intensity of the stress field in the immediate vicinity of a sharp crack tip.  $K_c$  is said to be independent of crack geometry and loading and may be regarded as an intrinsic material constant.

The factor  $K_c$  can be related to the critical energy release rate,  $G_c$ , which represents the amount of energy released during an incremental increase in crack area. For thin specimens:

$$G_c = \frac{K_c^2}{E} \quad (\text{plane stress}) \quad (13)$$

For thick specimens:

$$G_c = \frac{K_c^2}{E} (1-\nu^2) \quad (\text{plane strain}) \quad (14)$$

where  $E$  is the Young's modulus.

When the load or crack size is kept below the threshold point of unstable crack extension, the magnitude of this stress field is measured by  $K$  as follows:<sup>26</sup>

$$\begin{aligned} \sigma_x &= \frac{K}{\sqrt{2\pi r}} \cos\theta/2 (1 - \sin\theta/2 \sin 3\theta/2) \\ \sigma_y &= \frac{K}{\sqrt{2\pi r}} \cos\theta/2 (1 + \sin\theta/2 \sin 3\theta/2) \\ \tau_{xy} &= \frac{K}{\sqrt{2\pi r}} \cos\theta/2 \sin\theta/2 \cos 3\theta/2 \end{aligned} \quad (15)$$

The distance  $r$  is always kept small, but finite as the stresses are bounded.  $K$  is also restricted to symmetric systems where the applied tension is perpendicular to the crack plane.

Fracture mechanics allows for the calculation of the resistance of a material to crack growth due to the many possible stresses imposed on a flaw.  $K_I$  refers to the stress intensity factor of the crack under a tensile stress perpendicular to the crack face.  $K_{IC}$  for ceramics is the point at which the crack is travelling at a relatively high velocity, 0.01 m/s to 1.00 m/s. The fracture energy

of ceramics is related to  $K_{IC}$  and is affected by the microstructure (e.g. grain size, grain shape, porosity, fracture propagation mode, etc.).

### II.D.3. Toughening: Mechanisms and Modelling

#### II.D.3.a. Definition and Introduction

Toughness is a generic term which includes the critical stress intensity factor,  $K_{IC}$ , the critical strain energy release rate,  $G_c$ , and the critical fracture surface energy,  $\gamma_c$ . In general, regarding composites, only the two latter terms,  $G_c$  and  $\gamma_c$ , can be discussed.

The toughening of ceramics by incorporating non-linear microstructural elements has been commonly reported in the recent literature. The development of a new generation of tough ceramics has been achieved because of a close coupling between processing and characterization of microstructural features and mechanical testing and micromechanics. All processes that provide good toughness have the common feature that material elements close to the crack experience non-linear, hysteretic stress-strain behavior upon crack growth.<sup>27</sup>

#### II.D.3.b. Transformation Toughening

The transformation toughening in partially stabilized  $ZrO_2$  (PSZ) involves the elemental stress-strain behavior referred to as nonassociated flow. Specifically, the transformation appears to be

activated principally by a shear stress, but results primarily in a residual dilatation. Extensive twinning of the transformed particle, coupled with orientation randomness and spacing uniformity, relaxes long range shear strains, resulting in a crack tip field dominated by the residual dilatation. According to Evans<sup>27</sup>, a theory is in evolution to explain quantitatively the transformation toughening in PSZ and this investigation seems to be in good agreement with the experimental evidence.

For other transformation toughened materials such as tetragonal  $\text{ZrO}_2$  polycrystals (TZP) and  $\text{ZrO}_2$  toughened  $\text{Al}_2\text{O}_3$  (ZTA), the agreement of the theoretical results with the experimental results is not as evident, but seems to be consistent with the interpretation of a dilatation zone.

#### II.D.3.c. Microcrack Toughening

Residual dilatation and modulus reduction are the main contributions to the toughness. Nevertheless the contributions have a different influence depending on the material; this is particularly true in the case of the residual stress induced by the microstructure and the relative fracture resistance of the interface. The major problem in this situation for the theory is the nonadditive effects of the two separate contributions. Microcracks form an initial compression zone which is incompatible with the residual dilatation. The association of the reduction in elastic modulus with microcracks is responsible for the decrease of the stress intensity at the crack tip. So, the understanding of the microcracks as



toughening elements requires a systematic study of degradation effects on the overall microstructure.

Microcracking occurs only when a certain critical stress,  $\sigma_m$ , is attained in the microstructure. Thus, at the crack tip of a loaded crack a microcracked zone will develop bounded by this stress level. The reduced stress intensity at the crack tip,  $K_m$ , caused by microcracking can be expressed by <sup>26</sup>:

$$K_m = K' - AvK' - BE\delta\sqrt{h} \quad (16)$$

where  $K'$  is the stress intensity in the absence of microcracking,  $v$  is the measure of the microcracking density,  $A$  is a coefficient that depends on the shape of the zone,  $B$  is a coefficient that is related to the zone shape,  $h$  is the opening of the crack, and  $\delta = \frac{16(1-v^2)vS_r}{3E}$ , where  $S_r$  is the residual stress normal to the microcrack plane.

For composites reinforced with whiskers, it is assumed that each whisker forms two penny-shaped microcracks for  $\sigma > \sigma_{\text{critical}}$ . For  $B \approx 2r$ :

$$v = \frac{8nV_w r}{\pi l_w} \quad (17)$$

where  $n$  is the number of microcracks forming per whisker,  $V_w$  is the whisker content,  $r$  is the whisker radius, and  $l_w$  is the whisker length.

#### II.D.3.d. Ductile Dispersion Toughening

Ductile dispersions are effective only if they attract and locally entrap the matrix crack. This behavior is certainly obtained when the particles have an appreciably lower elastic modulus than the matrix. Residual tangential stress in the matrix can also encourage such tendencies. Once the crack is induced to intercept the particles, their high toughness allows them to remain intact in the crack wake. The intact particles exert tractions on the crack surface, inhibit crack opening and, thereby, increase fracture toughness. Such toughening requires intimate interfacial bonding, large particle size, and high strength particles devoid of hard precipitates that may act as ductile fracture nuclei. Such intimate bonding requirements contrast starkly with the weak interfaces needed for toughening by fiber pullout mechanisms.

#### II.D.3.e. Fiber/Whisker Toughening

The mechanisms by which fibers or whiskers reinforce ceramic matrices are an area of intense interest. First, when the crack tip encounters a fiber that it cannot break or get around, it is either impeded or deflected off in another direction. Thus, the crack is prevented from propagating through the structure. Second, if the bond between the reinforcement and the matrix is not too strong, crack propagation energy can be absorbed by pullout of the fiber from its original location. Third, fibers can bridge a crack, holding

the two faces together, thus preventing further propagation. The degree to which a fiber can absorb the energy of a developing crack depends on the nature of the fiber/matrix interface. Generally, the interface should be strong enough to transfer the load from the matrix to the fibers to produce high strength, but weak enough to fail locally rather than catastrophically. One of the common net effects of the several possible mechanisms is to divide a crack into two or more cracks.

The toughening behavior of whisker reinforced ceramics is analyzed in terms of a whisker bridging zone immediately behind the crack tip. The theoretical results based on both the stress intensity and the energy change introduced by bridging whiskers reveal the dependence of toughening upon the matrix, whisker, and interface properties.

The development of a high toughness composite from two brittle ceramic constituents (matrix and fibers) requires that the interface exhibit a non-linear response to the extending crack. The only available modes of interfacial non-linearity are debonding and sliding. Weakly bonded interfaces, capable of debonding and subsequent frictional sliding, are more tractable. Consequently, both sliding and debonding generally require consideration in the design and analysis of tough composites. The presence of sliding interfaces typically permits the fibers to remain intact in the crack wake, resulting in a bridging zone.

The toughening afforded by interfaces having a low shear resistance can only be achieved if initially bonded interfaces have previously debonded. Debonding is thus a central issue in the fiber

and whisker toughening of ceramics. Consequently, studies of interface fracture are expected to become a major research theme for the next decade, with the role of segregants, interphases, and residual stresses being of paramount importance.

In summary, potential mechanisms in the case of fiber/whisker toughening include crack deflection, fiber pullout, and wake toughening.

#### II.D.3.e.1. Crack Deflection

Thermal expansion mismatches determine the type of crack-microstructure interactions. If  $\alpha_{\text{fiber}} > \alpha_{\text{matrix}}$ , hoop compression and radial tension are created in the matrix, while the fiber is put in tension. In this situation, the crack deflects around the fiber. Additionally, the thermal expansion mismatch creates an interfacial tension, which decreases the effective shear resistance of the fiber/matrix interface. If  $\alpha_{\text{fiber}} < \alpha_{\text{matrix}}$ , hoop tension and radial compression exist in the matrix and the fiber is under compression. In this case, the crack is attracted to the fiber. Interfacial compressive stresses are also created, which increases the effective shear resistance of the fiber/matrix interface. The hoop tensile stresses which develop may promote matrix microcracking. Modeling of crack deflection toughening, performed by Faber and Evans<sup>28-29</sup>, describes the effectiveness of second phases in the form of rods or fibers in increasing the fracture surface area. The crack that deviates from the main plane of fracture by deflecting around fibers must exhibit a combination of crack front tilting and

twisting. As the fracture path becomes more tortuous, the plane is no longer normal to the applied stress. An increase in the applied stress is then necessary to cause the crack tip intensity to become large enough for further crack growth. Thus, crack deflection can result in significant toughening. However, a prudent strategy would seem to be to attempt to keep the matrix expansion slightly lower than that of the fiber. In this manner the fiber is in residual tension, as residual stress effects are kept to a minimum.

To assess the effects of these local deviations on toughening, Warren and Sarin<sup>30</sup> suggest a summation of the local contributions of the modes I, II, and III of fracture to give an effective virtual strain energy release rate,  $G_T$ , using the usual relation:

$$G_T = V_w \int_0^{u_0} \sigma(u) du \quad (18)$$

where  $\sigma(u)$  is the stress function and  $u_0$  is the upper limit of the displacement. The toughness of the deflecting material,  $G_c$ , is given by:

$$G_c = \frac{G_u}{G_T} G_c' \quad (19)$$

where  $G_u$  is the virtual strain energy release rate for the undeflected crack and  $G_c'$  is the toughness of the nondeflecting material. The degree of toughening to be expected merely from the increase in crack surface area associated with deflection is significantly lower

than that due to the entire reduction of the strain energy release rate.

#### II.D.3.e.2. Fiber Pullout

This mechanism requires fibers with a high transverse fracture toughness or weak fiber/matrix interfaces so that failure occurs along the fiber/matrix interface. Toughening results from the additional work required when fiber pullout occurs. The stress transferred to the fiber must be less than the fracture strength of the fiber, but the interfacial shear stress generated must be greater than the shear resistance of the fiber/matrix interface. The shear resistance is controlled by the degree of chemical and/or mechanical bonding. Thus, the interfacial shear resistance between the fiber and the matrix is important in determining the preferred fracture paths and ultimately fiber pullout. At elevated temperatures and at strains higher than that for the first matrix microcracking the air environment is permitted to penetrate to interfacial regions. This leads to removal of the carbon interface, oxidation of the fiber (increasing notch sensitivity), and accelerated fiber/matrix bonding with associated return to brittle behavior. This phenomenon is commonly referred to as the oxidation embrittlement.<sup>25</sup>

Marshall<sup>31</sup> suggested a technique for measuring frictional stresses between the reinforcement and matrix in ceramic matrix composites based on an indentation technique. Mecholsky and Baker<sup>32</sup> suggested a technique which can measure the resistance to

fracture in a tensile mode of failure for dissimilar materials. The effect of surface coatings, heat treatments, and chemical modifications to reinforcement on fracture have been analyzed.

Warren and Sarin have suggested a model for the pullout of the whiskers.<sup>30</sup> The model is simplified by considering a system of fully debonded whiskers, aligned uniaxially and normal to the crack plane. The whiskers are assumed to have a uniform length,  $l_w$ , that is less than  $l_c$ , the critical length for fracture. The whisker stress,  $\sigma_w'$ , lies between 0 and  $\frac{2\tau}{r} [\frac{l_w}{2} - u]$ . The average whisker stress,  $\sigma_w'(\text{average})$ , is then:

$$\sigma_w'(\text{average}) = \frac{\sigma_w'(\text{max})}{2} = \frac{\tau}{r} [\frac{l_w}{2} - u] \quad (20)$$

where  $\sigma_w'(\text{max})$  is the maximum value of the whisker stress,  $l_w$  is the whisker length, and  $\tau$  is the interfacial shear stress. The effective volume fraction of whiskers involved,  $V_{w \text{ eff}}$ , decreases in proportion to  $u$ , since increasing numbers of whiskers become completely pulled out:

$$V_{w \text{ eff}}(u) = [\frac{l_w}{2} - u] \frac{2}{l_w} V_w \quad (21)$$

The deviation of the toughness for the defecting material,  $\Delta G_c$ , becomes:

$$\Delta G_c = \frac{\tau V_w}{2 l_w r} \int_0^{u_0} (l_w - 2u)^2 du \quad (22)$$

For  $l_w < l_c$ :

$$\Delta G_c = \frac{\tau V_w l_w^2}{12r} \quad (23)$$

For  $l_w = l_c$ <sup>\$</sup> :

$$\Delta G_c = \frac{V_w \sigma_{wf}^2 r}{12\tau} \quad (24)$$

Since  $l_c$  represents the longest whisker that can be pulled out,  $\Delta G_c(l_w = l_c)$  represents the maximum possible toughening by pullout. This equation indicates the apparent benefits of high whisker strength and radius as well as low interfacial friction.

The toughening contribution is of a similar magnitude to that of bridging and exhibits a similar dependence on whisker content. Thus, to some extent these two processes can be considered to complement each other when estimating the effects of whisker content on the level of toughening.

#### II.D.3.e.3. Wake Toughening

Another toughening mechanism, somewhat related to fiber pullout, occurs when fibers bridge across the crack faces in the wake region of the extending crack. Nonlinear composite stress-strain continues as the matrix exhibits multiple microcracking with attendant composite modulus decrease. At this point some

---

<sup>\$</sup> In the literature, the coefficient 12 is referred as a coefficient 6. This must be

considered as a misprint;  $\Delta G_c = V_w \int_0^{u_0} \left( \frac{l_w}{2} - u \right) \frac{2}{l_w} \frac{\tau}{r} \left( \frac{l_w}{2} - u \right) du$ .

So  $\Delta G_c = \sqrt{F(\tau V_w, 2r l_w)} \sqrt{B(-\sqrt{F(1,6)}) [(l_w - 2u_0)^3 - l_w^3]}$ . For  $u_0 = \sqrt{F(l_w, 2)}$ ,  $\Delta G_c = \frac{\tau V_w l_w^2}{12r}$  and  $l_w = l_c = \frac{\sigma_{wf} r}{\tau}$ , yielding  $\Delta G_c = \frac{V_w \sigma_{wf}^2 r}{12\tau}$



fiber/matrix debonding occurs, exerting closure forces to restrict matrix crack opening.

#### II.D.3.e.3.1. Bridging Zone Characteristics

In order to establish a zone behind the crack tip in which the whiskers remain intact, the crack tip propagates through the matrix without fracturing the whiskers. In the case of SiC whisker reinforced  $\text{Al}_2\text{O}_3$ , the deflection of the crack as it approaches the interface due to differences in elastic properties is negligible ( $E_{\text{Al}_2\text{O}_3} = 400 \text{ GPa}$  and  $E_{\text{SiC}} = 550 \text{ GPa}$ ). The second process which would avoid whisker fracture involves debonding of the whisker/matrix interface as the crack approaches or just reaches the whisker. The matrix cracks propagate past the whiskers and result in bridging whiskers in the wake of the crack tip. Those mechanisms require that the interfacial fracture energy is much lower than that of the matrix or the whisker.

#### II.D.3.e.3.2. Analysis of Whisker Toughening

The toughening contributions derived from whisker reinforcement can be analyzed first in terms of the effects of the formation of a bridging zone of whiskers on the stress intensity of the composite system utilizing the concept similar to a Dugdale zone model.<sup>33</sup> While elastic-plastic analysis to determine the plastic region at a crack tip had been available, an explicit expression of the crack opening displacement was needed in order to

advance the Crack-Opening-Displacement concept. This was provided in 1960 by Dugdale<sup>34</sup>, in which he developed a closed-form solution applicable for plane stress conditions. Dugdale supposed that for a thin sheet loaded in tension, the yielding will be confined to a narrow band lying along the crack line. Mathematically, this idea is identical to placing internal stresses on the portions of the crack faces near the tip, the physical crack being the remaining stress free length. The magnitude of the internal stresses were taken to be equal to the yield stress of the material. In order to determine the length over which they acted, Dugdale postulated that the stress singularity must be abolished. For a crack of length  $2a$  in an infinite medium under uniform tension  $\sigma$ ,

$$\frac{a}{c} = \cos \left( \frac{\pi}{2} \frac{\sigma}{\sigma_y} \right) \quad (25)$$

where  $c=a+d$  and  $d$  is the length of the plastic zone at each crack tip. For small-scale yielding conditions<sup>\$</sup>:

$$d \approx \frac{\pi}{8} \left( \frac{K}{\sigma_y} \right)^2 \quad (26)$$

In addition, a separate approach adopted from the analysis by Piggot<sup>34-35</sup> is employed to define the toughening effects based on

---


$$\$ \frac{a}{c} = \frac{a}{(a+d)} = \cos \left( \frac{\pi\sigma}{2\sigma_y} \right) \text{ so } d = 2a \frac{\sin^2(\pi\sigma/4\sigma_y)}{\cos(\pi\sigma/2\sigma_y)}; \text{ for } \pi\sigma/4\sigma_y, d \approx \frac{a}{8} \left( \frac{\pi\sigma}{\sigma_y} \right)^2; \text{ from the}$$

$$C. \text{ffith theory, } K = \sigma\sqrt{\pi a} \text{ then } d = \frac{\pi}{8} \left( \frac{K}{\sigma_y} \right)^2$$

the energy change for crack growth in the presence of a whisker bridging zone. The stress transfer between whisker and matrix is ignored. The crack-opening displacement is assumed to be much smaller than the debonding length,  $l_{DB}$ . The interfacial shear stress,  $\tau$ , is held constant within the debonding length,  $0 < y < l_{DB}$ . The force required for the whisker to slide against the matrix is  $2\pi r(l_{DB}-y)\tau$  and the force exerted by the whisker is  $\pi r^2 \sigma(y)$ . The equilibrium conditions imply:

$$\sigma(y) = \frac{2(l_{DB}-y)\tau}{r} \quad (27)$$

The elastic energy,  $dU_e$ , stored in an element  $dy$  of the whisker due to bridging is\*:

$$dU_e = \frac{2\pi(l_{DB}-y)^2 \tau^2}{E^w} dy \quad (28)$$

where  $E^w$  is the Young modulus of the whisker. The work done in the element due to sliding of the whisker against the matrix is:

$$dU_s = 2\pi r \tau u \, dy \quad (29)$$

where  $u$  is the displacement of the whisker element relative to the matrix. If  $u$  is defined as:

---

\*  $dU_e = \frac{\sigma^2(y)}{2E^w} dV$ ; with  $dV = \pi r^2 dy$ , and  $\sigma(y) = \frac{2(l_{DB}-y)\tau}{r}$

$$u = \int_y^{l_{DB}} \varepsilon(y) dy = \frac{(l_{DB}-y)^2 \tau}{E^w r} \quad (30)$$

then#:

$$dU_s = \frac{2\pi(l_{DB}-y)^2 \tau^2}{E^w} dy = dU_e \quad (31)$$

where  $\varepsilon(y)$  is the strain function. The total energy change,  $\Delta G$ , is the sum of the stored elastic energy,  $U_e$ , and the work done by whisker sliding,  $U_s$ :

$$\Delta G = 2N \int_0^{l_{DL}} (dU_e + dU_s) = \frac{8\pi N \tau^2 l_{DB}^3}{3E^w} \quad (32)$$

where  $N$  is the average number of sliding whiskers. The maximum toughening occurs at the maximum strength of the whisker:

$$\sigma_f^w = \frac{2l_{DB}\tau}{r} \quad (33)$$

so:

$$\Delta G = \frac{\sigma_f^w V_W r G^m}{9E^w G^i} \quad (34)$$

where  $G^m$  is the toughness of the matrix and  $G^i$  is the toughness of the inclusion. For plane strain condition in the case of thick specimens:

---

#  $u_{max} = \frac{2\pi l_{DB}^2 \tau^2}{E^w}$  is equivalent by definition to half-opening displacement.

$$G = G^0 + \Delta G = \frac{K^2(1-\nu^2)}{E^c} \quad (35)$$

where  $G^0$  is the toughness of the composite without cracking and  $E^c$  is the Young's modulus of the composite. With  $K = K^0 + \Delta K$ :

$$\Delta K = \sqrt{K^{02} + \frac{(\sigma_f^w)^2 V_f r E^c G^m}{9(1-\nu^2) E^w G^i}} - K^0 \quad (36)$$

where  $\Delta K$  is the variation of stress intensity factor and  $K^0$  is the stress intensity factor of the composite without cracking.

While the bridging stress is assumed to be uniform in the Dugdale approach, in the Piggot approach the bridging stress varies along the debonding length, from zero at the end of debonding to the tensile strength of the whisker,  $\sigma_f$ , at the crack surface. The toughening contribution resulting from a bridging zone of length  $D_B$  behind the crack tip for a crack in an infinite plate is:

$$\Delta K = 2 \sqrt{\frac{c}{\pi}} \int_0^{D_B} \frac{\sigma(x)}{\sqrt{c^2 - (c-x)^2}} dx \quad (37)$$

where  $\sigma(x)$  is the stress acting on the bridging zone,  $c$  is half of the total crack length, and  $x$  is the distance behind the crack tip.

Other bridging models account for the fact that each bridging whisker exhibits a tensile stress distribution over its length, the

form of which depends on the extent of debonding. A corresponding counterstress distribution then exists in the matrix around the whisker.<sup>30</sup> Three distinct cases can be identified as follows:

(1) Case 1- The debond length is equivalent at  $2r$ . Although this may not be very realistic, it does permit the inclusion of all whiskers regardless of orientation. If the strain in the debond length is  $\epsilon = \frac{u}{2r}$ , then:

$$\Delta G_c = \frac{V_w}{2r} \int_0^{u_0} E_w u du = \frac{V_w E_w}{4r} u_0^2 \quad (38)$$

where  $u_0 = \epsilon_0 2r = 2r \frac{\sigma_{wf}}{E_w}$ . Substituting for  $u_0$  yields:

$$\Delta G_c = V_w r \frac{\sigma_{wf}^2}{E_w} \quad (39)$$

(2) Case 2- For debonded fibers in which the debond length increases linearly with distance behind the crack tip:

$$\sigma_w' = 4E_w \tau \frac{u}{r} \quad (40)$$

where  $\tau$  is the frictional slipping stress.  $\Delta G_c$  has then the following expression:

$$\Delta G_c = V_w r \frac{\sigma_{wf}^3}{6E_w} \quad (41)$$

(3) Case 3- For a rigidly bonded whisker:

$$K_c \approx 1.1 \sigma_{wf} [V_w r (1 - \sqrt{V_w}) (1 - V_w)] \quad (42)$$

Significant fracture toughness increases can be expected even with strongly bound whiskers, if they retain their high strength values.

#### II.D.3.f. Synergism

An exciting prospect for the coming years is the potential for synergism among toughening mechanisms. Synergistic toughening seems feasible by combining either ductile particles or fibers with transforming particles and possibly with microcracking particles, or continuous fibers with particulates or with short fibers. Such multiple toughening is not necessarily simply additive since depending on circumstance the presence of whiskers might either reduce or enhance another toughening process.

#### II.D.3.g. Effect of Reinforcement Orientation

Chopped fiber and whisker reinforced composites can be either transversely isotropic or isotropic. When these composites are fabricated and the fibers or whiskers are randomly distributed parallel to a single plane, then they are transversely isotropic. This means that only four independent elastic constants are required for their stress-strain description. If the fibers or the whiskers are distributed randomly in three dimensions, then the composite would be isotropic and require the determination of two elastic constants for a complete stress-strain description.<sup>32</sup>

When whiskers are employed as two-dimensional or three-dimensional randomly oriented short fibers, the toughening increments possible are severely limited to approximately 1/2 or 1/3 of that possible for the toughness direction in uniaxial composites. The major toughening increment is probably limited to that obtainable from crack-particle interaction toughening.<sup>36</sup>

#### II.D.4. R-Curve

##### II.D.4.a. Introduction

Pabst<sup>37</sup> and Buresch<sup>38</sup> were, respectively in 1972 and 1973, the first to suggest that polycrystalline ceramics exhibit an increased resistance to crack growth with increasing crack extension. Experiments have confirmed that as cracks extend in many polycrystalline ceramics and ceramic matrix composites, their resistance to further growth increases. The phenomenon has been described as rising R-curve behavior. Rising R-curve behavior is in large part responsible for the specimen size effects and the scatter of fracture toughness values that have been reported for brittle ceramics.<sup>39</sup>

##### II.D.4.b. Signification of R-Curves

The letter R represents the potential energy derived crack growth resistance defined by the potential energy dissipation per unit area of fracture surface. Typically, the R-curves are



represented as a graph where  $R$  is a function of  $\Delta a$ , the crack extension.

Three types of crack growth resistance or  $R$ -curves can be identified (see FIGURE 1). The flat  $R$ -curve is represented by a flat, straight line. It is characteristic of a perfectly brittle linear elastic material. This type of behavior is noticed in glasses and in most fine grain size structural ceramics. For large grain size ceramics, especially those with tabular or high aspect ratio grains, the flat  $R$ -curve gradually becomes a rising  $R$ -curve as the grain size increases.<sup>40</sup> Considering the fact that  $R$ -curves continue to increase for natural cracks and that this phenomenon sustains a cumulative toughening mechanism or process, it seems reasonable to conclude that the mechanisms responsible for the rising  $R$ -curve occur behind the advancing crack tip, the so called wake region.

At this stage it is important to emphasize that nonphase transforming ceramic materials have a different behavior in generating  $R$ -curves compared to metals where a front process zone, the plastic zone, is responsible for the rising  $R$ -curve behavior.

#### II.D.4.c. The Chevron-Notched Specimen

In the measurement of the  $R$ -curve behavior it is necessary to achieve sufficiently stable crack growth. In the case of brittle materials, conventional testing procedures are not adequate. Recently, Chevron-notched specimens in a number of configurations have successfully been used to determine plane-strain fracture toughness.

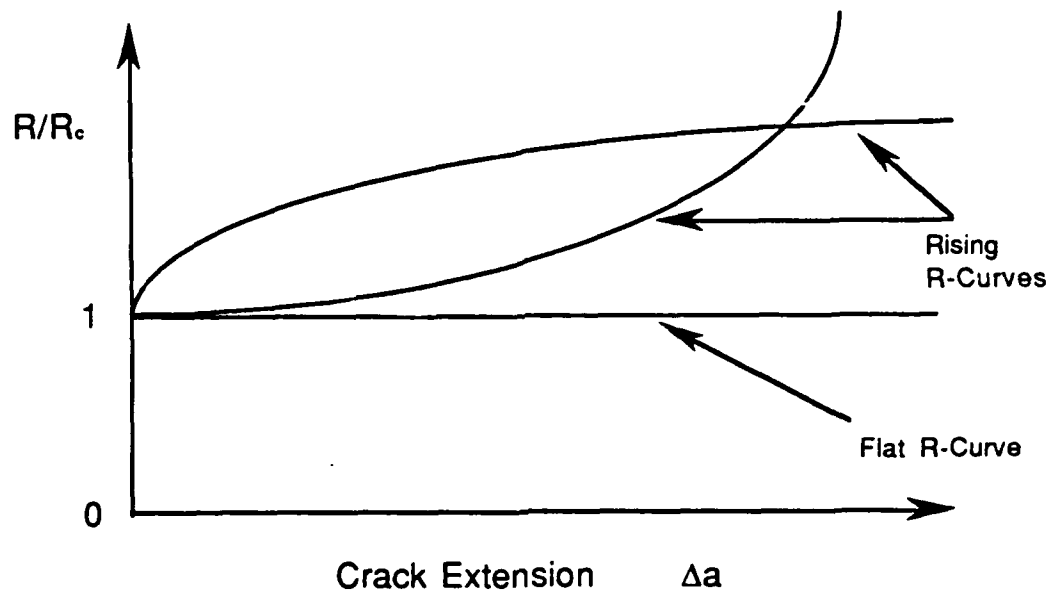


FIGURE 1: Three Types of Crack Growth Resistance Curves (R-curves) Reduced by Fracture Toughness,  $R_c$  (Reference 39).

Chevron-notched specimens are gaining widespread use for fracture toughness testing of brittle materials<sup>41</sup>. The unique features of Chevron-notched specimens, over conventional fracture toughness specimens, are the extremely high stress concentration achieved at the tip of the Chevron notch and a stress intensity factor that passes through a minimum as the crack grows. Because of the high stress concentration factor at the tip of the Chevron notch, a crack initiates at a low applied load, so costly precracking of the specimen is not needed, and then propagates stably until catastrophic fracture. The notch should be large enough to cover many fibers at the critical crack length. This test can be performed at room or high temperatures equally well. From the minimum stress intensity factor, the fracture toughness can be evaluated from the maximum test load. FIGURE 2 shows the conventional notation used in the literature to define the parameters involved with the Chevron-notched specimen.

#### II.D.4.d. Saw Tooth Behavior

When testing under stable crack growth conditions with a Chevron-notched, three point bend sample, the load-displacement curve may exhibit repeated crack initiation/crack arrest behavior<sup>2</sup>, also known saw tooth behavior (see FIGURE 3). This behavior has especially been noticed in the case of SiC whisker/ $\text{Al}_2\text{O}_3$  matrix composites. Both the crack arrest and crack initiation stress intensity factors exhibited rising R-curves with increasing crack length, suggesting wake toughening effects (see TABLE 5). The

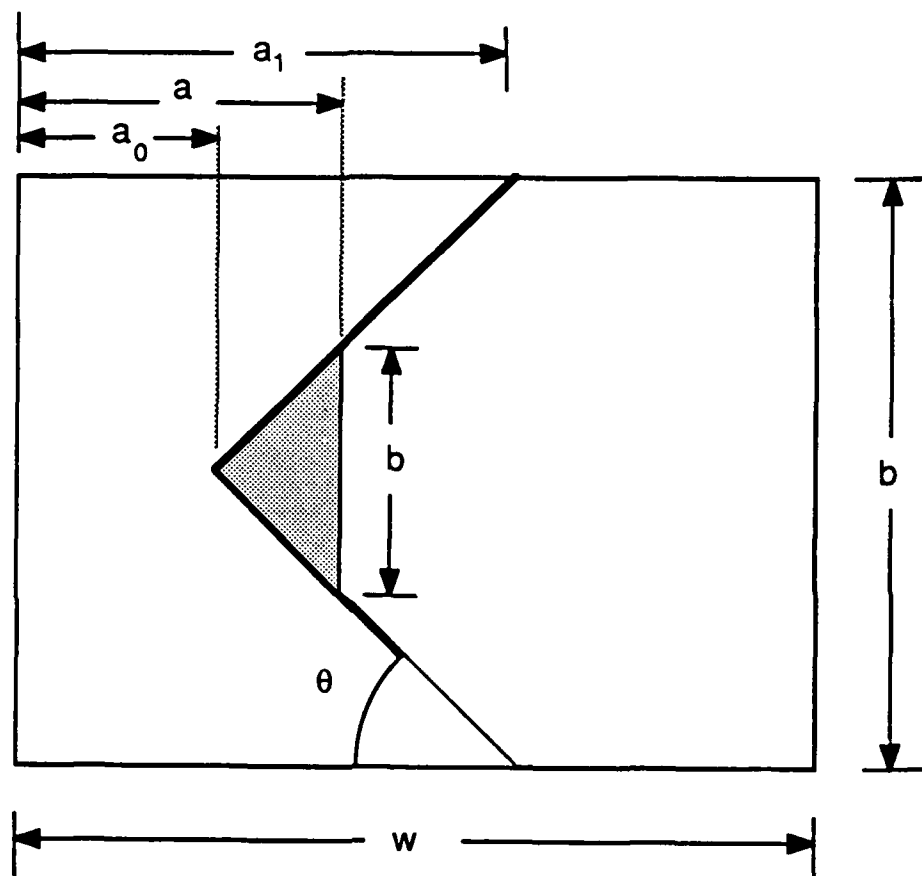


FIGURE 2: Schematic Diagram of Cross-Section of Chevron Notch (Reference 35).

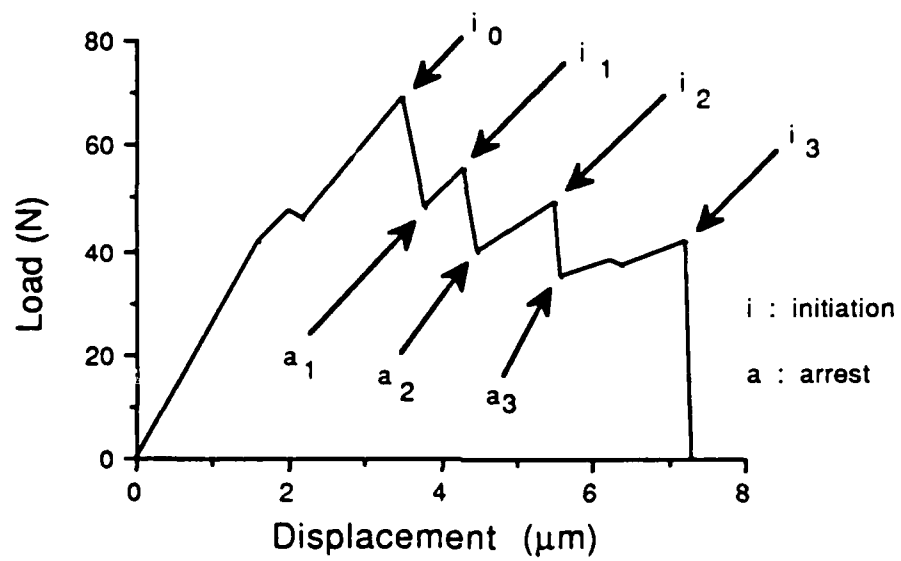


FIGURE 3: Schematic Diagram of the Saw Tooth Behavior Seen in the Load Displacement Curve during a Four Point Bend Flexure Test (Reference 2).

TABLE 5  
Initiation/Arrest Stress Intensity Factors (from Ref. 2)

(a/w)	$K_I$ arrest (MPa m <sup>1/2</sup> )	$K_I$ initiation (MPa m <sup>1/2</sup> )	$\Delta K$ (MPa m <sup>1/2</sup> )	(a/w)*
0.51		6.12		
0.57	5.57	6.08	0.51	0.59
0.65	5.70	6.36	0.66	0.67
0.72	6.16	6.92	0.76	0.76

\* From fractography measurements.

dimensionless stress intensity factor can be determined for the Chevron-notched specimen geometry based on the analysis of Sakai et al.<sup>45</sup> Therefore, for any specimen dimensions the actual stress intensity factor,  $K_i$ , and the corresponding load,  $P_i$ , for a given crack length, are related by:

$$K_i = \frac{P_i}{W^{1/2}B} \times Y_i \quad (43)$$

where  $B$  is the specimen thickness,  $W$  is the specimen width, and  $Y_i$  is the corresponding dimensionless stress intensity factor. Because of the saw tooth behavior of the load-displacement curve, it is not possible to generate a continuous R-curve. Discrete points of the R-curve can be calculated from the relative extremum of the saw tooth curve. The initiation stress intensity factor calculated at the first maximum load is generally accepted as the fracture toughness,  $K_{IC}$ .

#### II.D.4.e. Calculation of the R-Curve

For the determination of the fracture toughness of brittle materials, a short bar specimen with rectangular cross section and Chevron notch can be used.<sup>35</sup> For a straight through crack, the short bar specimen is similar to a double cantilever beam specimen, but with a smaller width to height ratio:

$$K = \frac{P}{B\sqrt{W}} Y \quad (44)$$

where  $K$  is the stress intensity factor,  $P$  is the applied load,  $W$  is the width of the specimen, and  $Y$  is the corresponding dimensionless stress intensity factor, also called the geometric correction factor for the straight notch specimen.

The fracture toughness for the Chevron-notched specimens can be calculated from the maximum load and the minimum geometry correction factor:<sup>42</sup>

$$K = \frac{P_{\max}}{B\sqrt{W}} Y^*_{\min} \quad (45)$$

where  $P_{\max}$  is the maximum applied load and  $Y^*_{\min}$  is the minimum geometry correction factor for the Chevron-notched specimen.

Calculations of Srawley and Gross<sup>43</sup> for a specimen with a straight through crack are applied to the specimen with a Chevron notch. The slice model of Bluhm (see FIGURE 4) is applied to explain the difference in compliance between the specimens with a straight through crack and those with a Chevron notch. The formulation of the geometry correction factor,  $Y^*$ , is dependent on the crack length. For a long crack length:

$$Y_1 = \frac{2.702 + 1.628 \alpha}{(1 - \alpha)^{3/2}} \quad (46)$$

where  $\alpha = \frac{a}{W}$ . For a short crack length:

$$Y_2 = \sqrt{12 \frac{W^3}{H^3}} \left( \alpha + \frac{0.679 H}{W} \right) \quad (47)$$



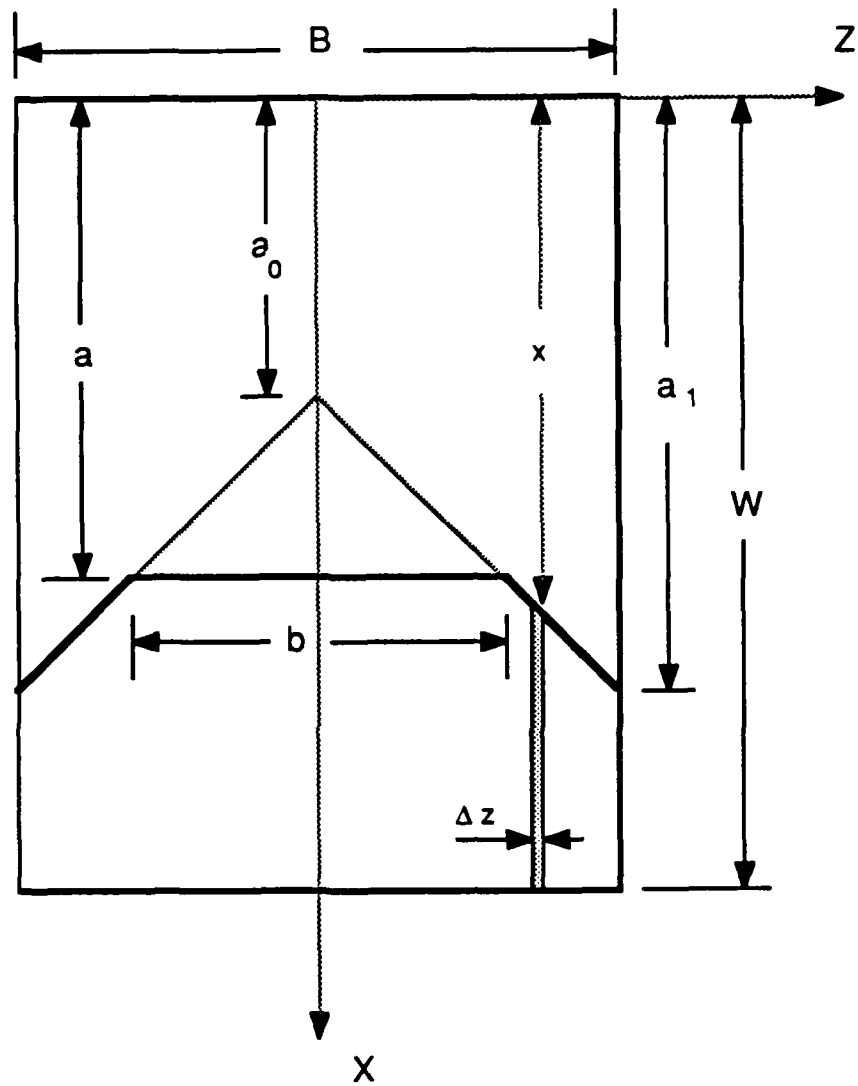


FIGURE 4: Schematic Diagram of the Slice Model of Bluhm (Reference 35).

For an intermediate crack length, an exponential superposition is suggested<sup>35</sup>:

$$Y = \frac{F \alpha}{(1-\alpha)^{3/2}} \quad (48)$$

where  $F$  is defined as follows:

$$F = \ln [\exp(F_1) + \exp(F_2)] \quad (49)$$

$$F_1 = \frac{Y_1 (1-\alpha)^{3/2}}{\alpha} \quad (50)$$

$$F_2 = \frac{Y_2 (1-\alpha)^{3/2}}{\alpha} \quad (51)$$

The geometry correction factor can be explained as a function of the dimensionless compliance:<sup>35</sup>

$$Y^* = \sqrt{\frac{1}{2} \frac{dC_{TR}}{d\alpha} \frac{\alpha_1 - \alpha_0}{\alpha - \alpha_0}} \quad (52)$$

where  $C_{TR} = E'BC$  is the dimensionless compliance.

For the Bluhm analysis, the sample is divided into a number of different slices of thickness  $\Delta z$  (see FIGURE 4). The compliance of a slice,  $C_s$ , with crack length  $x$  is:

$$C_s = C(\xi) \frac{B}{\Delta z} \quad (53)$$

where  $C(\xi)$  is the compliance of a straight through crack specimen of thickness  $B$  and crack length to width ratio  $\xi = \frac{x}{W}$ . The summation of the inverse  $C_s$  values yields  $\frac{1}{C_{TR}}$ :

$$\frac{1}{C_{TR}} = \sum_{i=1}^n \left( \frac{1}{C_s} \right)_i \quad (54)$$

$$\frac{1}{C_{TR}} = \frac{\alpha - \alpha_0}{\alpha_1 - \alpha_0} \frac{1}{C(\alpha)} + \frac{1}{\alpha_1 - \alpha_0} \int_{\alpha}^{\alpha_1} \frac{1}{C(\xi)} d\xi \quad (55)$$

The compliance of the slices in the section between the edge and the straight through part of the trapezoidal crack is influenced by interlaminar shear stresses. This interlaminar shear stress decreases the compliance of the slices. To take this effect into account, a shear transfer coefficient,  $k$ , is introduced in the thickness of the slice:

$$\Delta z' = k \Delta z \quad \text{with } k \geq 1 \quad (56)$$

then:

$$\frac{1}{C_{TR}} = \frac{\alpha - \alpha_0}{\alpha_1 - \alpha_0} \frac{1}{C(\alpha)} + \frac{k}{\alpha_1 - \alpha_0} \int_{\alpha}^{\alpha_1} \frac{1}{C(\xi)} d\xi \quad (57)$$

The shear transfer coefficient  $k$  is dependant on the angle  $\theta$  of the triangular notch and possibly on  $\alpha_1$  and should decrease with increasing  $\theta$  or decreasing  $\alpha_0$ .

The compliance of the straight through crack sample is related to the geometric correction factor by<sup>44</sup>:

$$C(\xi) = \frac{2}{E'B} \int_0^{\xi} Y^2(\xi) d\xi + C_0 \quad (58)$$

where  $C_0$  is the compliance of the specimen without a notch or crack in the environment of the experiment.  $C_0$  is defined as:

$$C_0 = C_{\text{Fixture Configuration}} + C_{\text{Initiation}}(\alpha) - C_{\text{Fixture}}(T) \quad (59)$$

where  $C_{\text{Fixture}}(T)$  is the compliance of the fixture as a function of temperature,  $C_{\text{Initiation}}(\alpha)$  is the compliance of the crack for each initiation, and  $C_{\text{Fixture Configuration}}$  is defined as followed:

$$C_{\text{Fixture Configuration}} = \left( \frac{S_1 - S_2}{W} \right)^2 \left( \frac{S_1 + 2S_2}{4W} + \frac{(1+\nu) W}{2(S_1 + S_2)} \right) \frac{1}{E'B} \quad (60)$$

where  $S_1$  is the major load roller span,  $S_2$  is the minor load roller span,  $W$  is the specimen width, and  $\nu$  is the Poisson's ratio.

The shear transfer coefficient,  $k$ , is obtained by analytical calculation. For  $0 < \alpha < 1$ :

$$k = 1 + \alpha_1^{3.12} (2.263 \theta - 4.744 \theta^2 + 4.699 \theta^3 - 1.774 \theta^4) \quad (61)$$

For  $\alpha > 1$ :

$$k = 1 + 0.444 \alpha_1^{3.12} \quad (62)$$

where:

$$\theta = \tan^{-1} \left( 2 \frac{(\alpha_1 - \alpha_0) W}{B} \right) \quad (63)$$

The expression of  $\frac{dC_{TR}}{d\alpha}$  is obtained from the derivative of the inverse of equation (57):

$$C_{TR} = \frac{1}{\frac{\alpha - \alpha_0}{\alpha_1 - \alpha_0} \frac{1}{C(\alpha)} + \frac{k}{\alpha_1 - \alpha_0} \int_{\alpha}^{\alpha_1} \frac{1}{C(\xi)} d\xi} \quad (64)$$

$$\frac{dC_{TR}}{d\alpha} = \frac{(-1) C_{TR}}{\alpha_1 - \alpha_0} \left( \frac{C(\alpha) - (\alpha - \alpha_0) \frac{dC(\alpha)}{d\alpha}}{C^2(\alpha)} + k \left( \frac{1}{C(\alpha_1)} - \frac{1}{C(\alpha)} \right) \right) \quad (65)$$

Using  $\frac{dC(\alpha)}{d\alpha} = \frac{2Y^2}{E'B}$ , equation (65) becomes:

$$\frac{dC_{TR}}{d\alpha} = \frac{(-1) C_{TR}}{\alpha_1 - \alpha_0} \left( \frac{C(\alpha) - (\alpha - \alpha_0) \frac{2Y^2}{E'B}}{C^2(\alpha)} + k \left( \frac{1}{C(\alpha_1)} - \frac{1}{C(\alpha)} \right) \right) \quad (66)$$

To obtain an expression of the Young's modulus for an unnotched beam,  $E'$ , an elastic beam of thickness,  $B$ , is bent to a radius,  $\rho$ , where  $\rho \gg B$  and the deformation is assumed to consist solely of the extension or contraction of longitudinal fibers of the beam in proportion to their distance from a central neutral surface,

which retains its original length. The moments from successive layers above and below this cooperate in tending to rotate the cross-section about this axis. If the width of the beam at this distance from the neutral surface is  $b(y)$ , then a total bending moment,  $M$ , is produced:<sup>45</sup>

$$M = \frac{E'}{\rho} \int y^2 b(y) dy = \frac{E' I}{\rho} \quad (67)$$

where  $\int y^2 b(y) dy$  is the second moment of area,  $I$ , of the cross-section. For a rectangular beam, where  $b(y) = b = \frac{W}{2}$ :

$$I = b \int_{-(B/2)}^{(B/2)} y^2 dy = \frac{b B^3}{12} = \frac{W B^3}{24} \quad (68)$$

and

$$M = \frac{P}{2} d = \frac{P(S_1 - S_2)}{4} \quad (69)$$

The deflection of a uniformly bent beam,  $y_0$ , is:

$$y_0 = \frac{S_1^2}{8\rho} = \frac{M S_1^2}{8E' I} = \frac{\frac{P(S_1 - S_2)}{4} S_1^2}{8E' \frac{W B^3}{24}} = \frac{3}{4} (S_1 - S_2) S_1^2 \frac{P}{E' W B^3} \quad (70)$$

The derivative of equation (70) yields:

$$E' = \left( \frac{3}{4} \frac{(S_1 - S_2) S_1^2}{W B^3} \right) \left( \frac{dP}{dy_0} \right) \quad (71)$$

At this point, it would be important to investigate the continuity of  $C_{TR}(\alpha)$  and the stress intensity factor  $K_1(\alpha)$  for  $\alpha \rightarrow \alpha_1$ . The model with  $\alpha = \alpha_1$  must be identical with a straight through notched model:<sup>46</sup>

$$\lim_{\alpha \rightarrow \alpha_1} C_{TR}(\alpha) = C(\alpha_1) \quad (72)$$

The condition described in equation (71) is always satisfied.

$$\lim_{\alpha \rightarrow \alpha_1} K_1(\alpha)_{\text{chevron}} = K_1(\alpha)_{\text{straight}} \quad (73)$$

Equation (73) implies two conditions expressed by equations (74) and (75):

$$\lim_{\alpha \rightarrow \alpha_1} \frac{dC_{TR}(\alpha)}{d\alpha} = \left( \frac{dC(\alpha)}{d\alpha} \right)_{\alpha=\alpha_1} \quad (74)$$

This condition described in equation (74) is obtained for  $\lim_{\alpha \rightarrow \alpha_1} k(\alpha) = 1$

$$\frac{1}{C_{TR}} = \frac{\alpha - \alpha_0}{\alpha_1 - \alpha_0} \frac{1}{C(\alpha)} + \frac{k}{\alpha_1 - \alpha_0} \int_{\alpha}^{\alpha_1} \frac{1}{C(\xi)} d\xi \quad (75)$$

Thus, the derivative of the compliance,  $\frac{dC_{TR}(\alpha)}{d\alpha}$ , will be discontinuous at  $\alpha = \alpha_1$  if the assumption of Bluhm is used. This assumption must be modified by assuming that  $k(\alpha)$  has a constant value  $k$  ( $>1$ ) over almost the whole range of  $\alpha$ , but tends to 1 in the

boundary layer in  $\alpha^* < \alpha < \alpha_1$ , in which  $\alpha^*$  is a characteristic crack length defining the boundary value of  $\alpha$ . The shear transfer coefficient must be redefined as:

$$\begin{aligned} k(\alpha) &= k > 1 && \text{for } \alpha^* \geq \alpha \geq \alpha_0 \\ k(\alpha) &= (k-1) \frac{\alpha - \alpha_1}{\alpha^* - \alpha_1} + 1 && \text{for } \alpha_1 \geq \alpha \geq \alpha^* \\ k(\alpha) &= 1 && \text{for } \alpha \geq \alpha_1 \end{aligned} \quad (76)$$

The value of  $\alpha^*$  is obtained by solving the equation (74).

## II.E. MECHANICAL PROPERTIES OF SiC WHISKER/Al<sub>2</sub>O<sub>3</sub> MATRIX COMPOSITES

### II.E.1. Introduction

When SiC whiskers are added to polycrystalline Al<sub>2</sub>O<sub>3</sub>, both the fracture toughness and fracture strength are significantly improved. The improved fracture strength and fracture toughness are retained to approximately 1200°C.<sup>47</sup> In addition, the SiC whisker/Al<sub>2</sub>O<sub>3</sub> matrix composites are very resistant to slow crack growth<sup>47</sup>, high temperature creep<sup>48</sup>, and thermal shock.<sup>49</sup> The increase in fracture toughness is primarily due to crack deflection, pullout, and bridging by the SiC whiskers.<sup>47</sup>



### II.E.2. Effect of Density

The fracture toughness and the flexural strength of SiC whisker/ $\text{Al}_2\text{O}_3$  matrix composites are dependent on the density of the composites. At whisker contents greater than 10 volume percent, Tiegs and Becher<sup>22</sup> showed that for composites fabricated by pressureless sintering the density was a critical parameter in determining the mechanical properties. At high whisker aspect ratios, the whiskers began to touch one another, accentuating the formation of agglomerates by rearrangement of particles during processing. As a consequence, low densification was noticed. FIGURE 5 summarizes the results obtained for composites fabricated by pressureless sintering. Homeny et al.<sup>3</sup> evaluated the effect of density on fracture toughness and fracture strength for hot pressed composites. FIGURES 6 and 7 show the results for fracture toughness and flexural strength, respectively, for composites fabricated by hot pressing.

### II.E.3. Effect of Whisker Content

By addition of SiC whiskers to polycrystalline  $\text{Al}_2\text{O}_3$ , the mechanical properties are substantially increased compared to monolithic  $\text{Al}_2\text{O}_3$ . TABLE 6 gives an overview of the values obtained for fracture strength and the fracture toughness at different whisker contents. The room temperature fracture toughness values reached a maximum of  $8.7 \text{ MPa}\cdot\text{m}^{1/2}$  for the composites fabricated

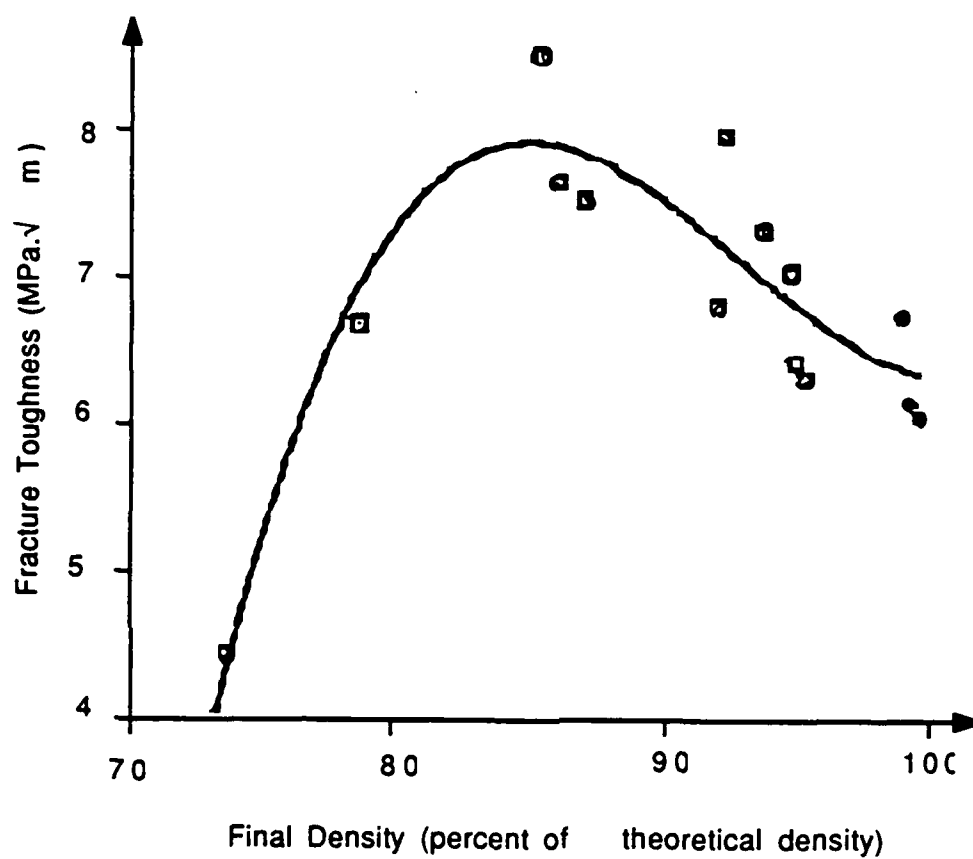


FIGURE 5: Fracture Toughness,  $K_{IC}$ , of Sintered 10 Volume Percent SiC Whisker/ $Al_2O_3$  Matrix Composites (Reference 22).

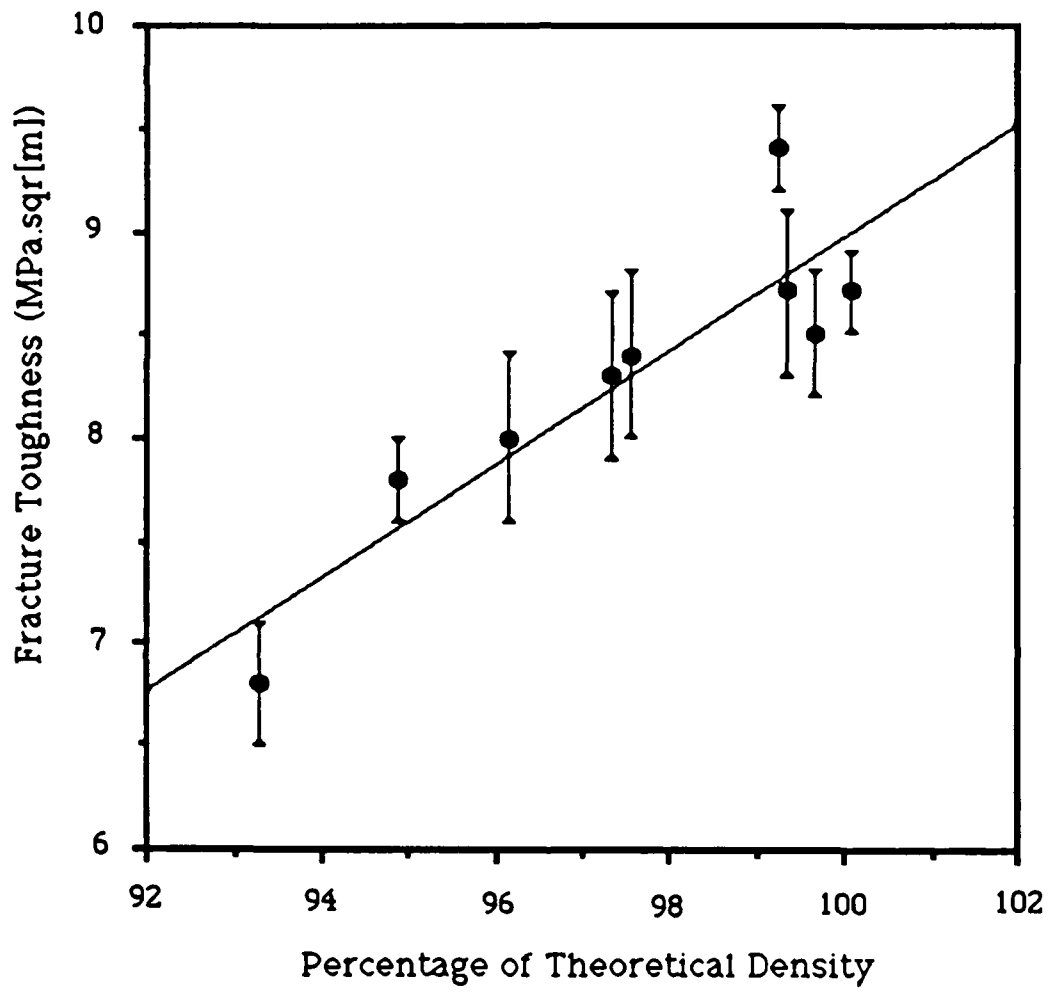


FIGURE 6: Fracture Toughness for 30 Volume Percent SiC/Al<sub>2</sub>O<sub>3</sub> Matrix Composite, as Measured by the Notched-Beam Technique, as a Function of Theoretical Density (Reference 3).

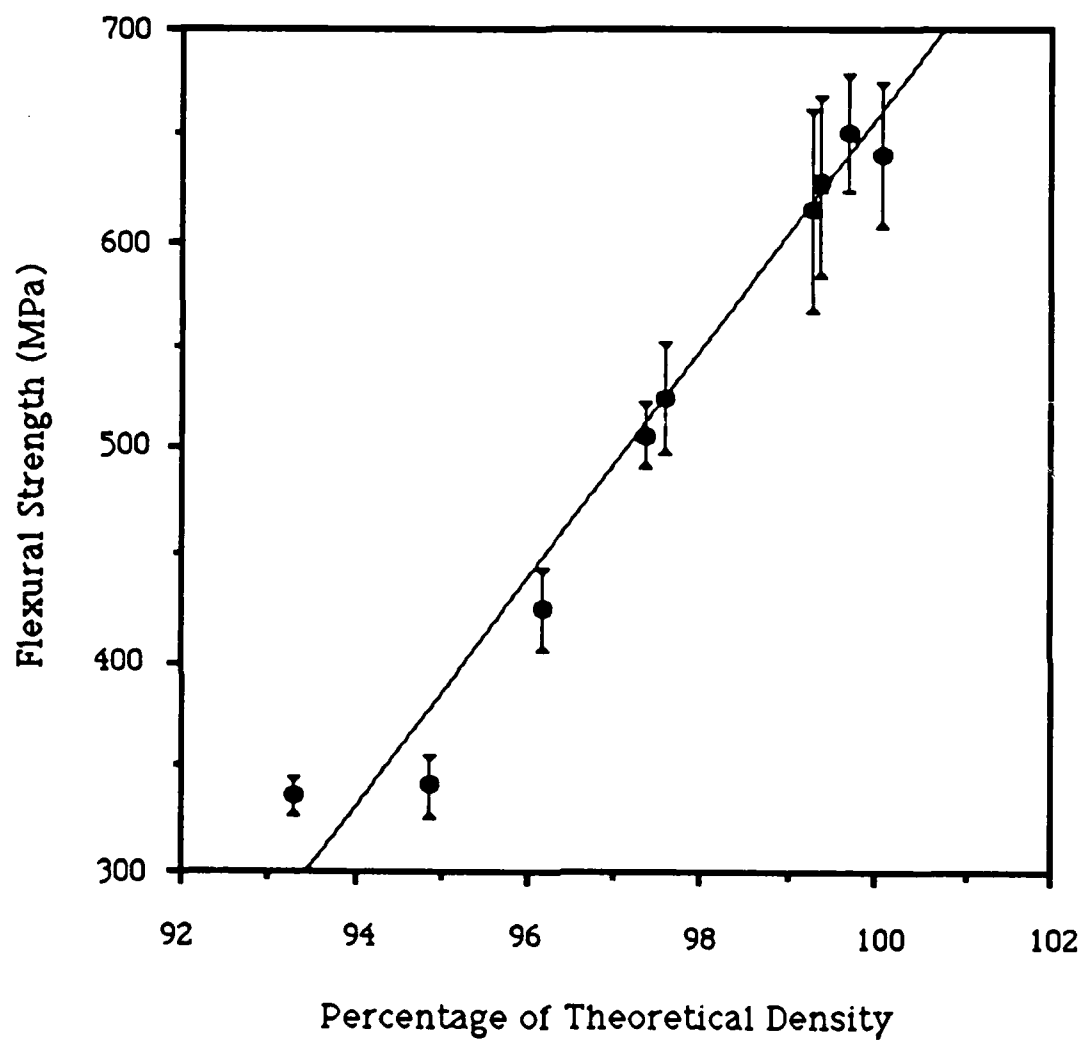


FIGURE 7: Flexural Strength for 30 Volume Percent SiC/Al<sub>2</sub>O<sub>3</sub> Matrix Composites as a Function of Theoretical Density (Reference 3)

TABLE 6  
Summary of Mechanical Properties of SiC Whisker/ $\text{Al}_2\text{O}_3$  Matrix  
Composites (from Ref. 1)

Whisker Content (vol.%)	Fracture Strength (MPa)	Fracture Toughness (MPa $\text{m}^{1/2}$ )	Test Temperature (°C)
0	150	4.3	25
15	652	4.6	25
30	680	8.7	25
40	850	6.2	25
<hr style="border-top: 1px dashed black;"/>			
40	680	6.4	1000
40	610	8.7	1200

with 30 volume percent SiC whiskers. For the room temperature fracture strength, the values increased as the whisker contents increased.

#### II.E.4. Effect of Temperature

Limited mechanical property measurements have been performed at elevated temperatures (see TABLE 6). The fracture toughness values for composites fabricated with 40 volume percent of SiC whiskers increased as the temperature increased. In contrast for the same composites the fracture strength decreased with increasing temperature.

Additionally, the effect of thermal cycling on the mechanical properties of the SiC whisker/ $\text{Al}_2\text{O}_3$  matrix composites has been investigated. Thermal shock testing of a 20 volume percent SiC whisker/ $\text{Al}_2\text{O}_3$  matrix composite showed no decrease in flexural strength with temperature differences up to  $900^\circ\text{C}$  (see TABLE 7).<sup>49</sup> Polycrystalline  $\text{Al}_2\text{O}_3$ , on the other hand, normally showed a significant decrease in flexural strength with a temperature change of greater than  $400^\circ\text{C}$ . Possible explanations for the increase in thermal shock resistance were that the thermal conductivity was higher and/or the thermal expansion was lower for the composite than for the monolithic  $\text{Al}_2\text{O}_3$ . However, the changes in these properties were relatively minor. Thus, the improvement in the thermal shock resistance of the 20 volume percent SiC whisker/ $\text{Al}_2\text{O}_3$  matrix composite was primarily attributed to the higher fracture toughness. Analysis indicated that crack bridging

TABLE 7

Flexural Strength after Thermal Shock Testing of Polycrystalline  $\text{Al}_2\text{O}_3$  and 20 volume percent SiC Whisker/ $\text{Al}_2\text{O}_3$  Matrix Composites (from Ref. 49)

Temperature Change (°C)	Flexural Strength (MPa)	Number of Quenches
20 vol. % SiC Whisker/ $\text{Al}_2\text{O}_3$ Matrix		
	620	0
300	630	1
300	610	10
500	690	1
500	570	10
700	610	1
700	540	10
900	710	1
900	545	10
Polycrystalline $\text{Al}_2\text{O}_3$		
	310	0
700	120	1

and deflection by the whiskers were the major toughening mechanisms, with some contribution from whisker pullout.

#### II.E.5. Effect of Whisker Orientation

Becher and Wei<sup>1</sup> determined fracture toughness and fracture strength as a function of whisker orientation (see TABLES 8 and 9). The fracture toughness was a function of the orientation of the crack plane. When the crack plane was oriented such that it was perpendicular to the plane of the whisker axis, large increases in the fracture toughness were observed. Observations of the crack plane revealed that whisker pullout as well as considerable crack deflection occurred. The fracture strengths of the composites also exhibited an orientation dependence. Low strength occurred when the crack or fracture plane was parallel to the whisker plane. An additional orientation dependence occurred when the crack or fracture plane was normal to the whisker plane. The fracture strengths of the composites were limited by the nonuniformity of the distribution of the whiskers.

#### II.E.6. Effect of Microstructure

The nature of the whisker/matrix interface is the primary microstructural feature responsible for improved mechanical reliability. A key factor in determining the interfacial characteristics is the whisker surface chemistry. Homeny et al.<sup>3</sup> examined this effect by fabricating composites with SiC whiskers



TABLE 8  
Four Point Flexural Strength of 20 volume percent SiC  
Whisker/ $\text{Al}_2\text{O}_3$  Matrix Composites (from Ref. 1)

$\text{Al}_2\text{O}_3$ Powder	Orientation of tensile axis/ tensile surface with respect to plane of whisker axis	$\sigma_F$ (MPa)	Orientation of fracture plane to whisker plane
Linde A	perp./perp.	361	paral.
	paral./paral.	527	perp.
	paral./perp.	600	perp.
CR 10	paral./paral.	669	perp.
	paral./perp.	805	perp.

TABLE 9  
Fracture Toughness of SiC Whisker/ $\text{Al}_2\text{O}_3$  Matrix Composites  
(from Ref. 1)

Specimen Orientation/ $\text{Al}_2\text{O}_3$ Powder	$K_{IC}$ (MPa.m <sup>1/2</sup> )
20 Vol. % SiC Whiskers	
crack plane parallel to plane of whiskers/ CR 10 $\text{Al}_2\text{O}_3$	5.6
crack plane normal to plane of whiskers/ CR 10 $\text{Al}_2\text{O}_3$	8.7
0 Vol. % SiC Whiskers	4.6

that were identical in all respects, except for their surface chemistry. The observed increase in fracture toughness for the SiC whisker/ $\text{Al}_2\text{O}_3$  matrix composite produced with Silar-SC-9 whiskers appeared to be due to contributions from both crack deflection and crack bridging/pullout mechanisms (see TABLE 10)<sup>50</sup>. Apparently the thin layer of  $\text{SiO}_x\text{C}_y$  or  $(\text{CH}_2)_n$  observed on the Silar-SC-9 whiskers acted to prevent a chemical bond at the interface. For composites fabricated with Tateho-SCW-1-S whiskers, there appeared to be an enhancement of interfacial shear stress, possibly due to chemical bond formation. The surfaces of these whisker consisted primarily of pure SiC. No whisker bridging or pullout was observed in these composites. Crack/microstructure interaction studies on the SiC whisker/ $\text{Al}_2\text{O}_3$  matrix composites revealed that crack deflection and pullout by the whiskers were the predominant toughening mechanisms when the thin layer of  $\text{SiO}_x\text{C}_y$  or  $(\text{CH}_2)_n$  was present. Crack branching was frequently observed. Examination of fracture surfaces also revealed that extensive whisker pullout toughening mechanisms were activated when the thin layer of  $\text{SiO}_x\text{C}_y$  or  $(\text{CH}_2)_n$  was present. No whisker pullout was evident for composites produced with clean SiC surfaces. It was concluded that the nature of the interface between the whiskers and matrix was the most critical factor in determining the mechanical properties of ceramic matrix composites. If the interface was strongly bonded, matrix cracks propagated through whiskers and the composite failed in a brittle manner. However, if the interface was weakly bonded, then debonding and fiber pullout lead to nonbrittle response of the

TABLE 10  
Physical and Mechanical Properties of Polycrystalline  $\text{Al}_2\text{O}_3$  and SiC  
Whisker/ $\text{Al}_2\text{O}_3$  Matrix Composites (from Ref. 3)

S**	Polycrystalline	Composite	Composite
	$\text{Al}_2\text{O}_3$	Silar-SC-9*	Tateho-SCW-1-
Density ( $\text{g/cm}^3$ )	3.92	3.74	3.71
% Theoretical Density	99.2	100.0	99.2
Grain Size ( $\mu\text{m}$ )	<2.5	<2.5	<2.5
Fracture Strength (MPa)	456	641	606
Fracture Toughness ( $\text{MPa m}^{1/2}$ )	3.3	8.7	4.6

\* Arco Metals Company, Greer, S. C., U. S. A.

\*\* Tateho Chemical Industries Co. Ltd., Hyogo-Ken, Japan

composite, with a nonlinear stress-strain curve, large strain to failure, and load carrying capacity beyond the peak load.

Tiegs et al.<sup>51</sup> further analyzed the effect of the whisker/matrix interface on the mechanical reliability. Silar SC-9 and Tateho SCW-1 SiC whiskers were used to reinforce polycrystalline  $\text{Al}_2\text{O}_3$ . The contributions to bonding between the SiC whiskers and the  $\text{Al}_2\text{O}_3$  matrix was determined to come from two sources; mechanical and/or chemical bonding. The mechanical bond was due to the thermal expansion mismatch between the  $\text{Al}_2\text{O}_3$  and the SiC. Using the analysis of Selsing<sup>52</sup> for calculating stresses at the whisker/matrix interface, the contraction of the  $\text{Al}_2\text{O}_3$  matrix applied a radial compressive stress of approximately 1900 MPa on the SiC whisker. Bonding can also occur from the chemical interaction between the SiC whiskers and  $\text{Al}_2\text{O}_3$  matrix during processing at the fabrication temperature. The whisker surface chemistry was again found to be a key factor in determining the mechanical reliability. In particular the oxygen content was much higher for the whiskers used in the composite that exhibited low fracture toughness. Examination of whisker surface chemistry revealed a  $\text{SiO}_2$ , rather than SiC surface layer. However, even the whiskers used in the high toughness composite had some surface  $\text{SiO}_2$ , but at a much lower level. Evidently a high surface  $\text{SiO}_2$  content on the whisker surface lead to a chemical reaction with the  $\text{Al}_2\text{O}_3$  matrix and increased chemical bonding at the interface.

### III. EXPERIMENTAL PROCEDURE

#### III.A. INTRODUCTION

The fabrication of high quality SiC whisker/ $\text{Al}_2\text{O}_3$  matrix composites is necessary for obtaining meaningful R-curve measurements. In this section, the composite fabrication details and the procedures for generating R-curves under the various conditions are described. The experimental variables are emphasized, including composite fabrication parameters (e.g. whisker type and content) and mechanical testing conditions (e.g. test configuration and temperature).

#### III.B. RAW MATERIALS

The composites involved in this study were ceramic matrix composites; an  $\text{Al}_2\text{O}_3$  matrix was reinforced with SiC whiskers. The  $\text{Al}_2\text{O}_3$ <sup>\$</sup> was a high purity reactive powder obtained from ALCOA. The data provided by the manufacturer for the  $\text{Al}_2\text{O}_3$  powder are shown in TABLE 11. SiC whiskers from two sources, were evaluated for reinforcing the  $\text{Al}_2\text{O}_3$  matrix. Whiskers were obtained in limited amounts from ARCO Metals Corporation \$\$ and from Tateho Chemical Industries Corporation \$\$\$ . The data provided by the manufacturer for the two types of whiskers are shown in TABLE 12.

---

<sup>\$</sup> A-16SG  $\text{Al}_2\text{O}_3$ , ALCOA, Chemicals Division, Pittsburgh, PA, U.S.A.

<sup>\$\$</sup> Silar SC-9 SiC Whiskers, ARCO Metals Co., Greer, SC, U.S.A.

<sup>\$\$\$</sup> SiC Whisker SCW # 1-S, Tateho Chemical Industries Co. Ltd., Hyogo-Ken, JAPAN.

---

TABLE 11  
Manufacturer's Data for the  $\text{Al}_2\text{O}_3$  Powder

---

---

$\text{Al}_2\text{O}_3$ Type	A16-SG (Alcoa)	
Medium Particle Size ( $\mu\text{m}$ )	0.73	
Surface Area ( $\text{m}^2/\text{gm}$ )	6.5	
Crystal Type	Alpha	
Bulk Chemical Composition	$\text{Al}_2\text{O}_3$	99.5+ (Wt.%)
	$\text{SiO}_2$	0.025
	$\text{Fe}_2\text{O}_3$	0.01
	$\text{Na}_2\text{O}$	0.08

---

TABLE 12  
Manufacturer's Data for the SiC Whiskers

	Silar SC-9 (Arco)	Tateho SCW-1-S (Tateho)
Physical Properties		
Diameter ( $\mu\text{m}$ )	0.5-0.6	0.3-0.6
Aspect Ratio	60	80
Density (gm/cm)	3.2	3.2
Crystal Type	Alpha	Alpha
Modulus (GPa)	700	700
Strength (GPa)	7	7
Bulk Chemical Composition		
Silicon	70.3 (Wt. %)	71.3 (Wt. %)
Carbon	25.3	27.6
Oxygen	1.19	0.47
Iron	0.023	0.040
Cobalt	<0.001	<0.001
Chromium	0.001	0.007
Calcium	0.19	0.047
Manganese	0.073	0.005
Aluminium	0.10	0.13
Magnesium	0.076	0.006
Sodium	<0.01	<0.01



### III.C. PROCESSING OF COMPOSITES

#### III.C.1. Mixing of the Raw Materials

The raw materials were mixed by a liquid slurry technique. Six composite specimens were processed; 15, 30 and 45 volume percent SiC whiskers for each of the two whisker types. This set of composites was processed under the same routine.

Raw material mixing consisted of the following sequential steps:

(1) The  $\text{Al}_2\text{O}_3$  powder was weighed out<sup>\$</sup> (see TABLE 13) and poured into stirring<sup>\$\$</sup> deionized water.

(2) After weighing out the SiC whiskers (see TABLE 13), they were added to the  $\text{Al}_2\text{O}_3$  containing slurry.

(3) The slurry was adjusted at 15 percent solids by weight (i.e., 150 gm of solids in 800 to 900 ml of water).

(4) After soaking the pH-meter electrodes in deionized water until they stabilized, the pH-meter was calibrated in pH 9 buffer solution.

(5) The  $\text{pH}_1$  of the slurry was measured and adjusted to  $\text{pH}_2 > 10$  with  $\text{NH}_4\text{OH}$ .

(6) The slurry was blended<sup>\$\$\$</sup> at high shear for 2 minutes.

---

<sup>\$</sup> DIAL-O-GRAM Balance, Ohaus, Florham Park, NJ., U.S.A.

<sup>\$\$</sup> Model 1279, King Size Pyro-magnestir, Lab-Line Instruments, Melrose Park, IL., U.S.A.

<sup>\$\$\$</sup> Model 1266, two speed blender, Waring Products Division, Dynamics Corp. of America, New Hartford, CT, U.S.A.

TABLE 13  
Ratio of Raw Materials

	Vol. <sub>SiC</sub> (cm <sup>3</sup> )	Vol. <sub>Alumina</sub> (cm <sup>3</sup> )	Mass <sub>SiC</sub> (gm)	Mass <sub>Alumina</sub> (gm)	Mass <sub>T</sub> (gm)
15 Vol. %	10.425	59.075	33.36	233.93	267.297
30 Vol. %	20.85	48.65	66.72	192.65	259.374
45 Vol. %	31.275	38.225	100.08	151.371	251.451

(7) The blended slurry was poured into a clean beaker and ultrasonically dispersed\* for 6 minutes.

(8) While stirring, the  $\text{pH}_3$  was measured and reduced to  $\text{pH}_4=7$  with  $\text{HNO}_3$ . The different values of the pH during the mixing process are shown in TABLE 14.

(9) While stirring, the slurry was heated to remove the water content to achieve a solids content of about 30 to 40 percent (i.e., 150 gm of solids in 400 to 500 ml of water).

(10) The resulting slurry was partially dried in a furnace at  $125^\circ\text{C}$  for 24 hours.

(11) The dried mixture was ground with a mortar and a pestle until it passed through a # 8 mesh screen.

(12) The powder was reintroduced in the oven at  $125^\circ\text{C}$  for 12 hours.

### III.C.2. Hot Pressing of Composites

Under 1/2 argon atmosphere, the samples were uniaxially hot pressed in a vacuum hot press.\*\* The carbon die\*\*\* had a cylindrical shape with a 152.4 mm outside diameter and a 76.2 mm inside diameter. The rams were 76.2 mm in diameter. The SiC whisker/ $\text{Al}_2\text{O}_3$  powder mixtures were placed in the die and

---

\* Sonicator Model W375, Heat Systems - Ultrasonics Inc., Farmingdale, NY, U.S.A.

\*\* 30 ton vacuum hot press, GVA Corporation/Vacuum Industries Division, Somerville, MA, U.S.A.

\*\*\* ATJ grade carbon, Union Carbide, Carbon Products Division, Cleveland, OH, U.S.A.

---

TABLE 14  
pH Measurements during the Mixing Process

---

	pH <sub>1</sub>	pH <sub>2</sub>	pH <sub>3</sub>	pH <sub>4</sub>
15 Vol. %	8.80	10.49	10.14	6.97
30 Vol. %	8.72	10.51	10.27	7.00
45 Vol. %	8.37	10.57	10.25	7.08

---

separated from the die walls and rams by carbon foil\* and carbon spacers to enhance the life time of the die. The furnace was heated using graphite resistance heating elements with a maximum power input of 40 kilowatts. The temperature was controlled using a two color infrared pyrometer focused on the outside of the die wall. FIGURE 8 shows a schematic of the hot press furnace. The pressures, temperatures and times used in hot pressing the samples are shown in TABLE 15. The resulting samples were in the shape of a disk with a diameter of 76.2 mm (see FIGURE 9).

### III.C.3. Machining of the Composites

The samples were machined in two steps. First, they were surface ground with a 600 grit diamond wheel. At this stage, the samples were in the shape of a disk with parallel faces and an appropriate geometric volume used for calculating the density. Afterwards, the composite as a bulk was sent to a machine shop\$ to be cut into bars. Figure 6 shows the orientation of the bars in the disk. The R-curve test fixture required bars within the dimensions 3 mm x 4 mm x 60 mm. Two bar layers with 9 bars per layer were generated. All cut surfaces were ground with a 320 grit diamond wheel and all dimensions are plus or minus 0.01 mm. The edges of the bars were beveled to avoid the concentration of stresses at these regions during mechanical testing.

---

\* GTA-5 mil, Union Carbide, Carbon Products Division, Cleveland, OH, U.S.A.

\$ Bomas Machine Specialities Inc., Somerville, MA, U.S.A.

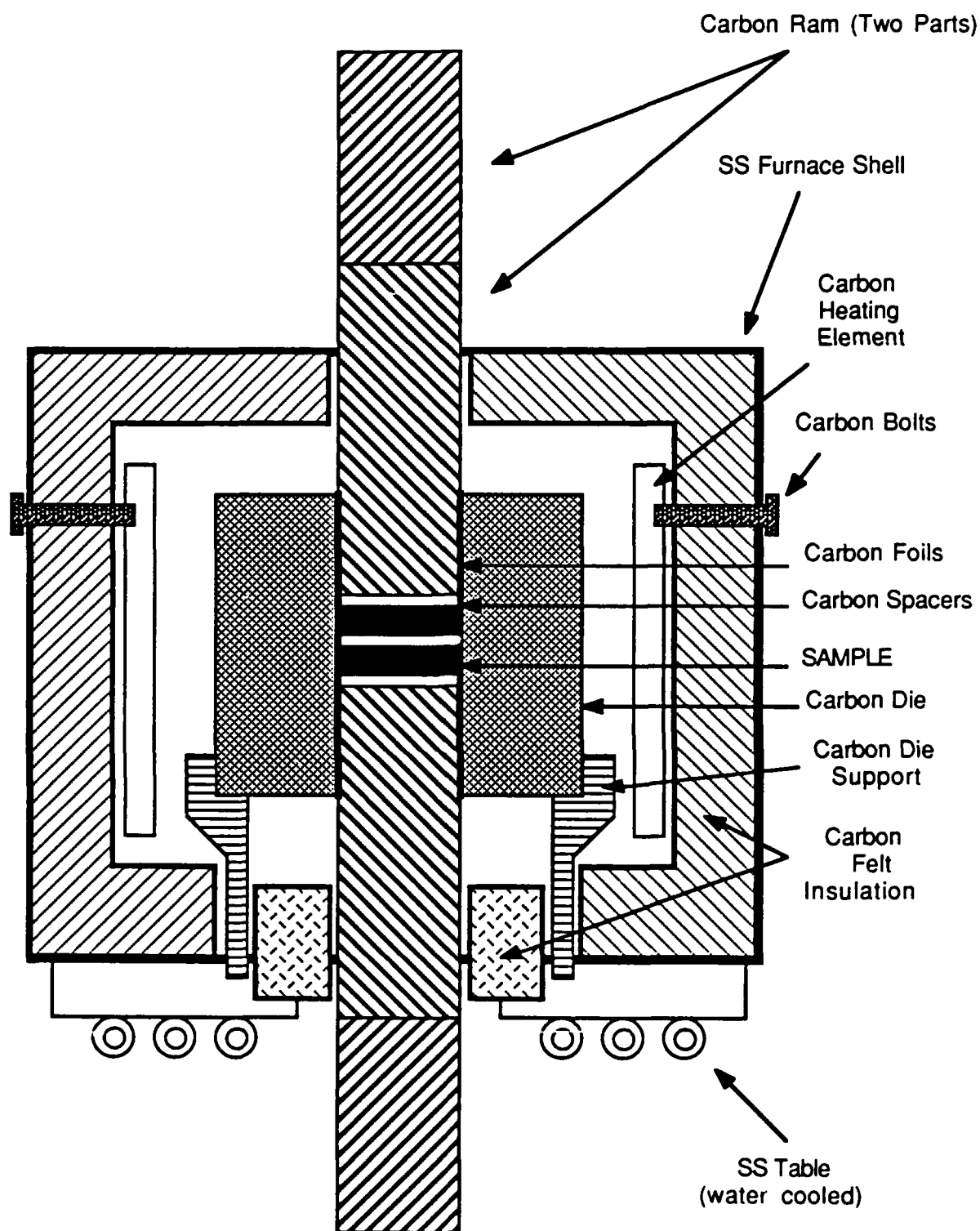


FIGURE 8: Schematic Diagram of the Hot Press Furnace.

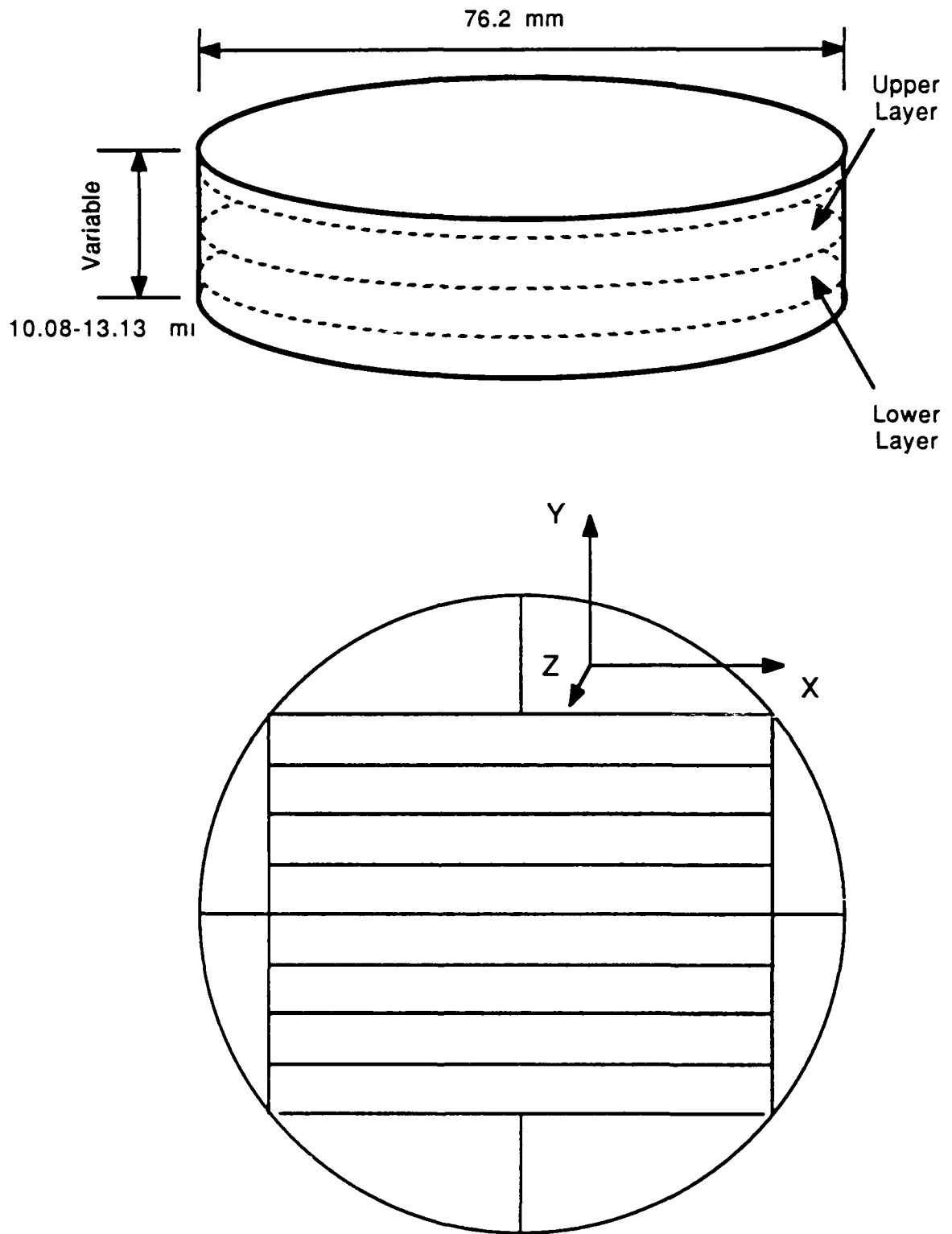


FIGURE 9: Shape of the Hot Pressed Samples and Schematic Diagram of the Bar Positions in the Samples (The z-axis is the hot pressed direction).

TABLE 15  
Processing Parameters for Uniaxial Hot Pressed Composites

Whisker Types	SiC (Vol. % )	Al <sub>2</sub> O <sub>3</sub> (Vol. % )	Pressure (MPa)	Temperature (°C)	Time (Min.)
Tateho SCW-1-S	15	85	32	1900	60
Tateho SCW-1-S	30	70	32	1900	60
Tateho SCW-1-S	45	55	32	1900	190
Silar SC-9	15	85	32	1900	60
Silar SC-9	30	70	32	1900	60
Silar SC-9	45	55	32	1925	180
No Whisker	0	100	32	1510	10



### III.D. CHARACTERIZATION OF THE COMPOSITES

#### III.D.1. Density Measurements

The theoretical densities of the materials were calculated by knowing the content of the different components in the composites and the theoretical densities of the components. The densities of  $\text{Al}_2\text{O}_3$  and  $\text{SiC}$  were  $d(\text{Al}_2\text{O}_3) = 3.96 \text{ gm/cm}^3$  and  $d(\text{SiC}) = 3.2 \text{ gm/cm}^3$ , respectively. The theoretical density,  $d_{\text{theoretical}}$ , was calculated using the following expression:

$$d_{\text{theoretical}} = \frac{M(\text{Al}_2\text{O}_3) \times d(\text{Al}_2\text{O}_3) + M(\text{SiC}) \times d(\text{SiC})}{M(\text{Al}_2\text{O}_3) + M(\text{SiC})} \quad (77)$$

where  $M(\text{Al}_2\text{O}_3)$  and  $M(\text{SiC})$  are the respective masses of  $\text{Al}_2\text{O}_3$  and  $\text{SiC}$ .

For the measurement of the effective densities, the disks with parallel faces were weighed on an electronic balance<sup>\$</sup>. The ratio of the weight,  $M_{\text{measured}}$ , over the measured volume,  $V_{\text{measured}}$ , yielded the following:

$$d_{\text{measured}} = \frac{M_{\text{measured}}}{V_{\text{measured}}} \quad (78)$$

The percentage of theoretical density,  $\%d_{\text{theoretical}}$ , was calculated from the previous densities as follows:

---

<sup>\$</sup> Model AE 166, Mettler Instrument Corp., Hightstown, NJ, U.S.A.

$$\%d_{\text{theoretical}} = \frac{d_{\text{theoretical}}}{d_{\text{measured}}} \times 100 \quad (79)$$

### III.D.2. R-curve Behavior

#### III.D.2.a. Introduction

To measure R-curve behavior by the Chevron notch technique, several experimental conditions must be achieved. The calculation of the R-curve requires the existence of a load-displacement curve exhibiting stable fracture (i.e., slow crack growth throughout the fracture process). Two parameters are of great importance in order to attain the optimum experimental environment; the design and precision of the mechanical testing equipment and the geometry of the specimen.

#### III.D.2.b. Mechanical Testing Equipment

The load-displacement curve was achieved with a compression test in a four point bend fixture. The test was performed in stroke control with a crosshead speed of 0.0152 mm/min. With this displacement rate, a stiff test machine was needed<sup>\$</sup> (see FIGURE 10). A tension-compression load cell of capacity 1kN was installed<sup>\$\$</sup>. The high temperature four point bend fixture<sup>\$\$\$</sup> was made of SiC (see FIGURE 11). To eliminate the extra load that the

---

<sup>\$</sup> Model 1332-152, Instron Corporation, Canton, MA, U.S.A.

<sup>\$\$</sup> Model 2518-806, Instron Corporation, Canton, MA, U.S.A.

<sup>\$\$\$</sup> Model 3118-024, Instron Corporation, Canton, MA, U.S.A.

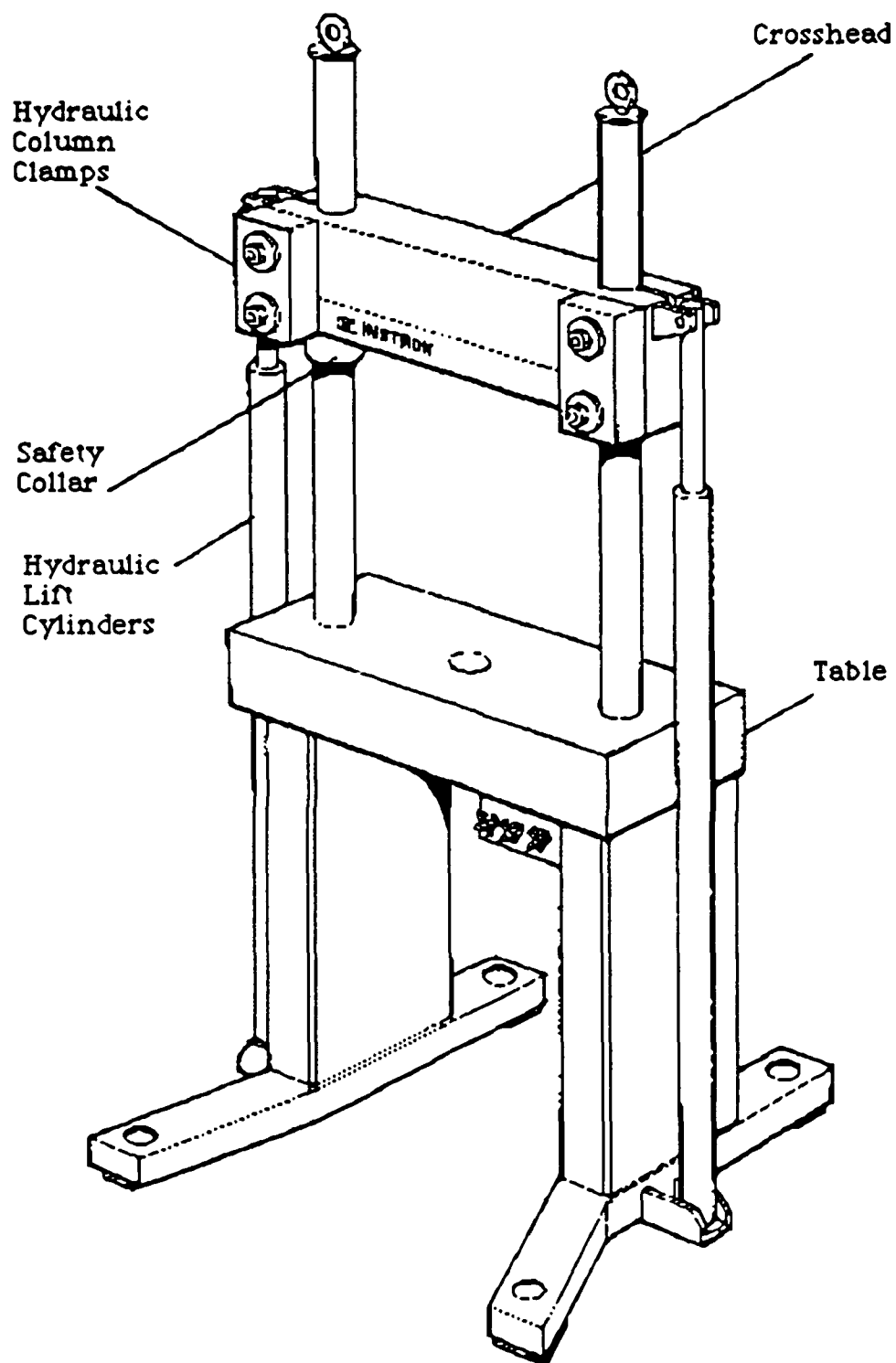


FIGURE 10: Schematic Diagram of the Mechanical Testing Machine.

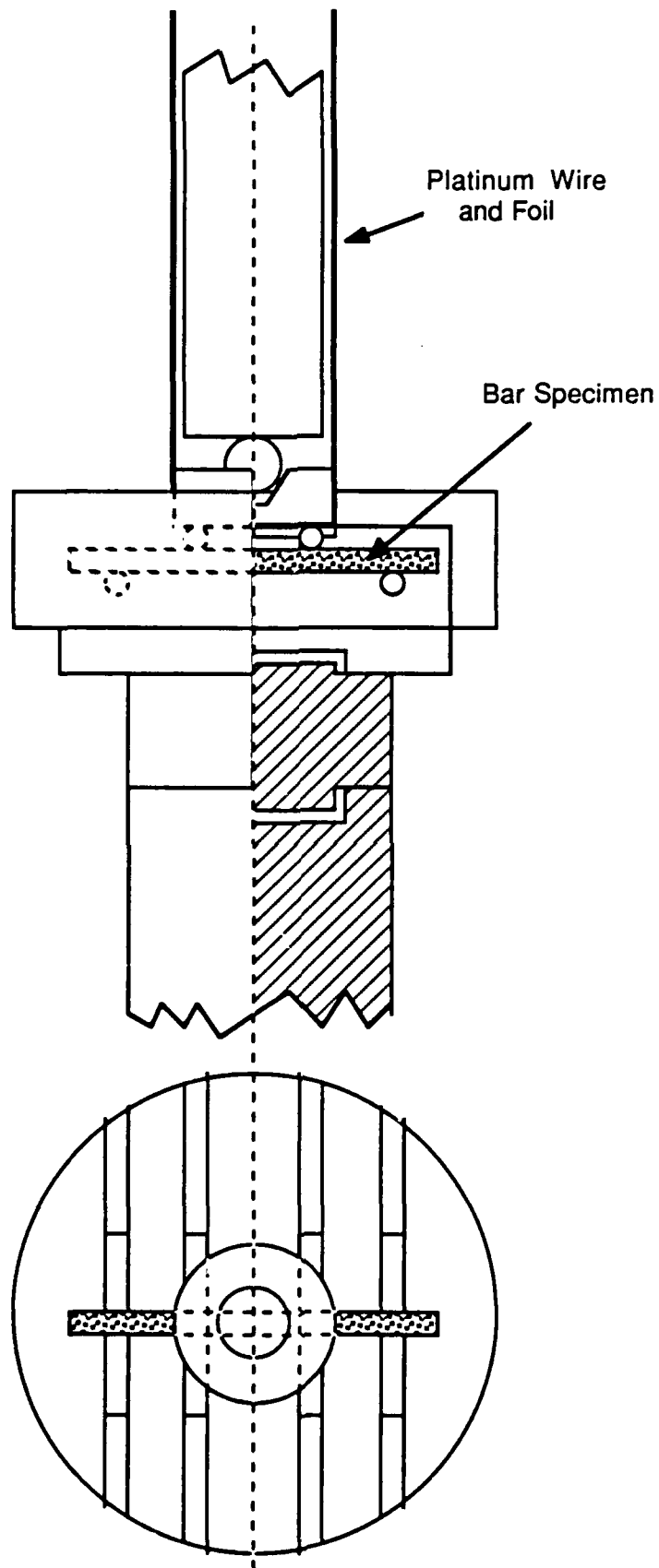


FIGURE 11: Schematic Diagram of the Four Point Bend Test Fixture.

upper part of the fixture applied on the sample, platinum foil and wires were used to suspend it from a fixed part of the machine frame. For the high temperature measurements, a furnace\* was heated with kanthal super 33 elements for service to 1650°C. A thermocouple, type R platinum/platinum-13% rhodium, was installed as close as possible to the sample to control the temperature in the furnace at the vicinity of the sample. The outputs of the stroke cell and the load cell were respectively plotted on the x-axis and y-axis of a X-Y recorder\*\*.

#### III.D.2.c. Specimen Geometry

To initiate the crack at a particular position on the bar and to obtain an increasing resistance as the crack propagates, a Chevron notched bar configuration was chosen (see FIGURE 12). The Chevron notch was generated with a high speed saw\*. The blade\*\* had the following characteristics; OD = 9.52 cm, ID = 1.59 cm, thickness = 0.023 cm, grit size 325, and diamond depth = 0.32 cm. The angle of the Chevron notch was either: 69.44° and 45° at the base of the triangle. To be sure to initiate the crack, a slight cut with a razor blade was performed at the tip of the Chevron notch.

---

\* Model 3320 High Temperature Split Furnace, Applied Testing Systems, Inc., Butler, PA, U.S.A.

\*\* Model 3023 A3 X-Y recorder, Yokogawa Electric Works, Ltd, Tokyo, Japan.

\* Aremco Accu-Cut 5255, AREMCO PRODUCTS, Inc., Ossining, N.Y., U.S.A.

\*\* 120 Series Accu-Cut Diamond Saw Blade, AREMCO PRODUCTS, Inc., Ossining, N.Y., U.S.A.

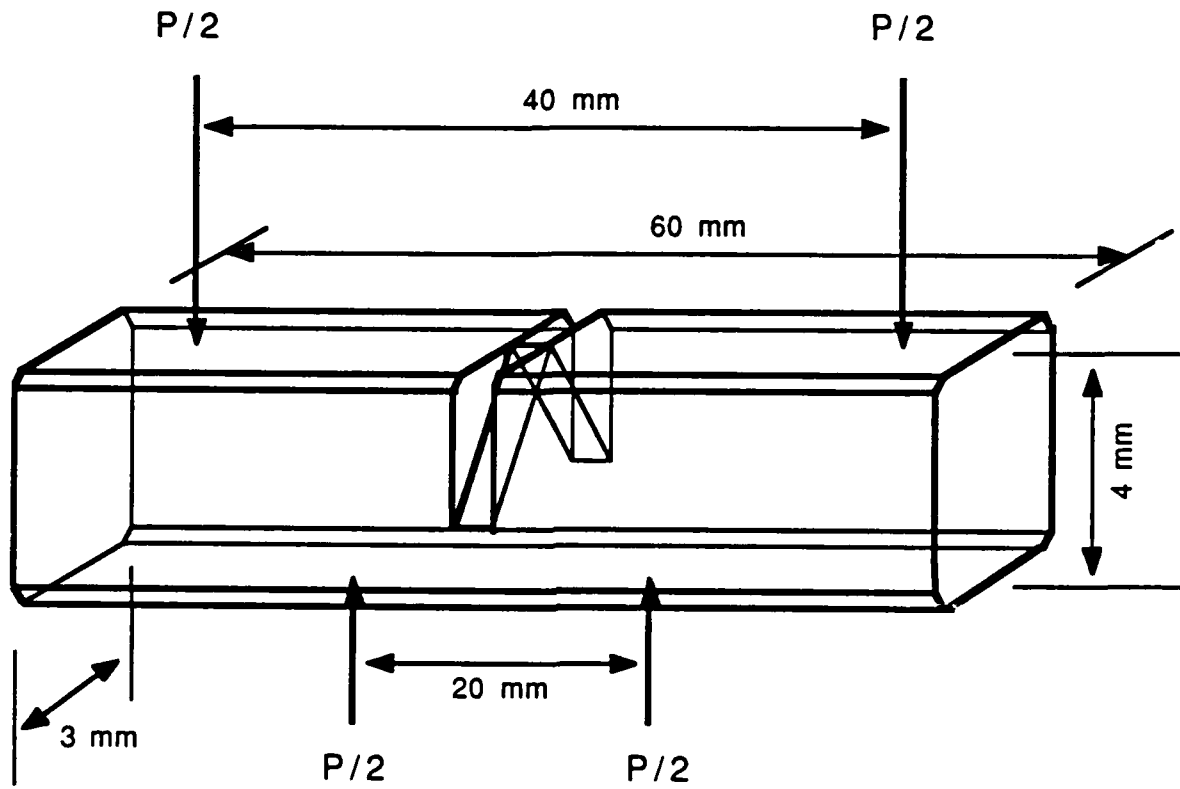


FIGURE 12: Schematic Diagram of the Chevron Notched Specimen.

### III.D.2.d. Calculation of R-curves

The mathematical development of section II.D.4.e. can be simplified in agreement with the numerical values of the different variables. In the particular case of this experiment, the characteristic values of the setup were:

$$W = 4 \text{ mm}$$

$$B = 3 \text{ mm}$$

$$H = 30 \text{ mm} \quad (\text{since } 2H \text{ is the total length of the bar})$$

$$S_1 = 40 \text{ mm}$$

$$S_2 = 20 \text{ mm}$$

$$\theta_1 = 69^\circ 44' \quad \text{or} \quad \theta_2 = 45^\circ$$

The main difficulty was to evaluate the geometric factor,  $Y^*$ , of a Chevron-notched bar specimen as a function of the crack length ratio,  $\alpha$ . The first step was to express every parameter as a function of the crack length ratio ( $\alpha$ ), the Poisson's Ratio ( $\nu$ ), and the Young's Modulus ( $E'$ ). The Young's Modulus ( $E'$ ) was measured on the load-displacement curve in the linear portion where the material had an elastic mechanical behavior. For the Poisson's Ratio ( $\nu$ ), a pulse echo technique<sup>53</sup> with a commercial ultrasonic testing system\* was used. The values of  $\nu$  were found to be relatively constant among the different composite materials and a value of

---

\* NDT-150, Nortec Inc., Kennewick, WA, U.S.A.

0.22 was chosen for the calculations. After computation\*\* of the variable numbers,  $Y^* = f(\alpha)$  was determined.

### III.D.3. Fractography

#### III.D.3.a. Introduction

One goal of this investigation was to evaluate the type of toughening mechanisms that generate the rising R-curves. At room temperature, SiC whisker reinforced  $Al_2O_3$  matrix composites react to the propagation of the crack by the activation of several toughening mechanisms. The debonding and bridging of the whisker across the crack path have been clearly identified at room temperature. To evaluate toughening mechanisms that may occur at

---


$$^{**} F_1 = \frac{2.702}{\alpha} + 1.628 \text{ and } F_2 = 0.169 \left( 1 + \frac{5.092}{\alpha} \right) (1-\alpha)^{3/2} ;$$

$$C_{\text{Fixture Configuration}} = \frac{41944.445 + \nu 277.778}{E'} ;$$

$$C(\xi) = \frac{666.667}{E'} \int_0^{\xi} Y^2(\xi) d\xi + \left( \frac{41944.445 + \nu 277.778}{E'} \right) + C_{\text{Initiation}}(\alpha) - C_{\text{Fixture}}(T)$$

$$\frac{1}{C_{TR\theta 1}} = \frac{\alpha}{C(\alpha)} + k \int_{\alpha}^1 \frac{d\xi}{C(\xi)} \text{ with } k_{\theta 1}(\theta_1=1.212 \text{ rad}) = 1.312 ; \frac{1}{C_{TR\theta 2}} = \frac{\alpha}{0.375 C(\alpha)} +$$

$$\frac{k}{0.375} \int_{\alpha}^{0.375} \frac{d\xi}{C(\xi)} \text{ with } k_{\theta 2}(\theta_2=0.785 \text{ rad}) = 1.021$$

$E' = 2.222 \cdot 10^5 \times \left( \frac{dP}{dy_0} \right)$  where  $\left( \frac{dP}{dy_0} \right)$  is the slope of the load-displacement curve in the elastic region.



both room and high temperature fractography was performed by scanning electron microscopy (SEM).

### III.D.3.b. Scanning Electron Microscopy

Scanning electron microscopy specimens were prepared from Chevron notch fracture surfaces. After testing, the two pieces left from the bars were cut with a low speed saw\*. The specimens were mounted on an aluminum stub with colloidal graphite suspension.\$ In order to prevent charging of the fracture surface, a carbon coating was deposited with a vacuum coating unit\*\*.

The observation has been achieved under a scanning electron microscope\$\$\$. The pictures and negatives were developed with Polaroid 55 instant sheet film.

---

\* Buehler Isomet<sup>®</sup>, Low Speed Saw, AB. Buehler Ltd., Evanston, IL, U.S.A.

\$ Aquadag<sup>®</sup>, Acheson Colloids Company, Port Huron, Michigan, U.S.A.

\*\* Vacuum Coating Unit, Type LC1-14B, Consolidated Vacuum Corporation, Rochester, NY, U.S.A.

\$\$\$ Hitachi S-800, Hitachi Inc., Japan.

## IV. RESULTS AND DISCUSSION

### IV.A. INTRODUCTION

This research involved the measurement and, to a certain extent, the interpretation of the R-curve behavior for SiC whisker/ $\text{Al}_2\text{O}_3$  matrix composites. Several parameters were investigated to achieve a better understanding of the R-curve behavior. The temperature during the mechanical testing was the parameter of most interest. The ultimate goal was to compare the room temperature and high temperature R-curve behavior of the composites. This comparison was extended to the type and the content of whiskers in the composites. To generate a R-curve from a load-displacement curve, a crack must be propagated in a quasi-stable manner. The sample geometry was also investigated for this purpose. A summary of the results concerning the load-displacement curves, the geometric correction factor curves, and the R-curves for different conditions is presented in Appendices A, B, and C, respectively.

### IV.B. PROCESSING

The choice of the parameters during hot pressing was very important in the control of the densification and in the ultimate microstructure for both the monolithic  $\text{Al}_2\text{O}_3$  and the SiC whisker/ $\text{Al}_2\text{O}_3$  matrix composites. TABLE 16 shows a summary of the uniaxial hot press parameters and the values of the theoretical

TABLE 16  
Uniaxial Hot Press Parameters and Measured Densities

Whisker Types	SiC (Vol. % )	Al <sub>2</sub> O <sub>3</sub> (Vol. % )	Measured Density (g/cm <sup>3</sup> )	Theoretical Density (g/cm <sup>3</sup> )	Pressure (MPa)	Temperature (°C)	Time (Min.)
Tateho SCW-1-S	15	85	3.813 (99.16%)*	3.846	32	1900	60
Tateho SCW-1-S	30	70	3.698 (99.09%)	3.732	32	1900	60
Tateho SCW-1-S	45	55	3.426 (94.90%)	3.610	32	1900	190
Silar SC-9	15	85	3.804 (98.91%)	3.846	32	1900	60
Silar SC-9	30	70	3.694 (98.98%)	3.731	32	1900	60
Silar SC-9	45	55	3.563 (98.70%)	3.610	32	1925	180
No Whisker	0	100	3.890 (98.40%)	3.960	32	1510	10

\* Percent of Theoretical Density.

densities for the different materials. The literature<sup>3</sup> suggests for the hot pressing conditions; a pressure of 32 MPa, a temperature of 1900°C, and a pressing time of 60 minutes. For the SiC whisker contents of 15 and 30 volume percent, the percentage of theoretical density was higher than 98 percent. For the SiC whisker content of 45 volume percent, the large volume of whiskers was more difficult to align in the plane perpendicular to the hot press axis. As a result, full densification was not achieved. In anticipation of this behavior, the pressing time was increased from 60 minutes to approximately 180 minutes. In the case of the composite fabricated with 45 volume percent Tateho SCW-1-S SiC whiskers, the density reached only 94.90 percent of theoretical density. In order to enhance the densification in the case of the composite fabricated with 45 volume percent Silar SC-9 SiC whiskers, the temperature was increased by 25°C. A theoretical density of 98.70 percent was obtained.

In the case of monolithic  $\text{Al}_2\text{O}_3$ , the hot press parameters (temperature = 1510°C and time = 10 minutes) were chosen to achieve the same grain size as that in the matrix of the composites. The monolithic  $\text{Al}_2\text{O}_3$  was used as a standard material for the investigation of the mechanical testing procedure.

#### IV.C. THE MECHANICAL TESTING: R-CURVES

##### IV.C.1. Room Temperature Testing

#### IV.C.1.a. The Effect of Chevron Notch Geometry

Two different Chevron notch angles were investigated; 69.44 degrees and 45 degrees. Those angles are described as  $\theta$  in FIGURE 2. The attempt at  $\theta = 69.44^\circ$  was to have a maximum amount of material left in the Chevron notch. There were some difficulties achieving controlled crack growth with this geometry. In contrast, the attempt at  $\theta = 45^\circ$  showed better crack growth stability (see FIGURE 13). As a result of the experiment, all remaining samples were tested with  $\theta = 45^\circ$ . Additionally, two Chevron-notched samples were tested to generate each R-curve.

#### IV.C.1.b. Load-Displacement Curves

For composites fabricated with the two types of whiskers, the typical difference in the shape of the load-displacement curves is shown in FIGURE 14. For composites fabricated with Tateho SCW-1-S SiC whiskers, the load-displacement curves showed a quasi-continuous shape. The only singularity was at the end of the linear portion of the curve at the limit of the elastic behavior of the composite. This point represented the load transfer from the matrix to the whiskers. For composites fabricated with Silar SC-9 SiC whiskers, irregularities appeared in the decreasing load portion of the curves, in addition to the point of load transfer. The crack was arrested and initiated at the relative extremes. This phenomenon is referred to as saw tooth behavior. FIGURE 15 specifies the positions

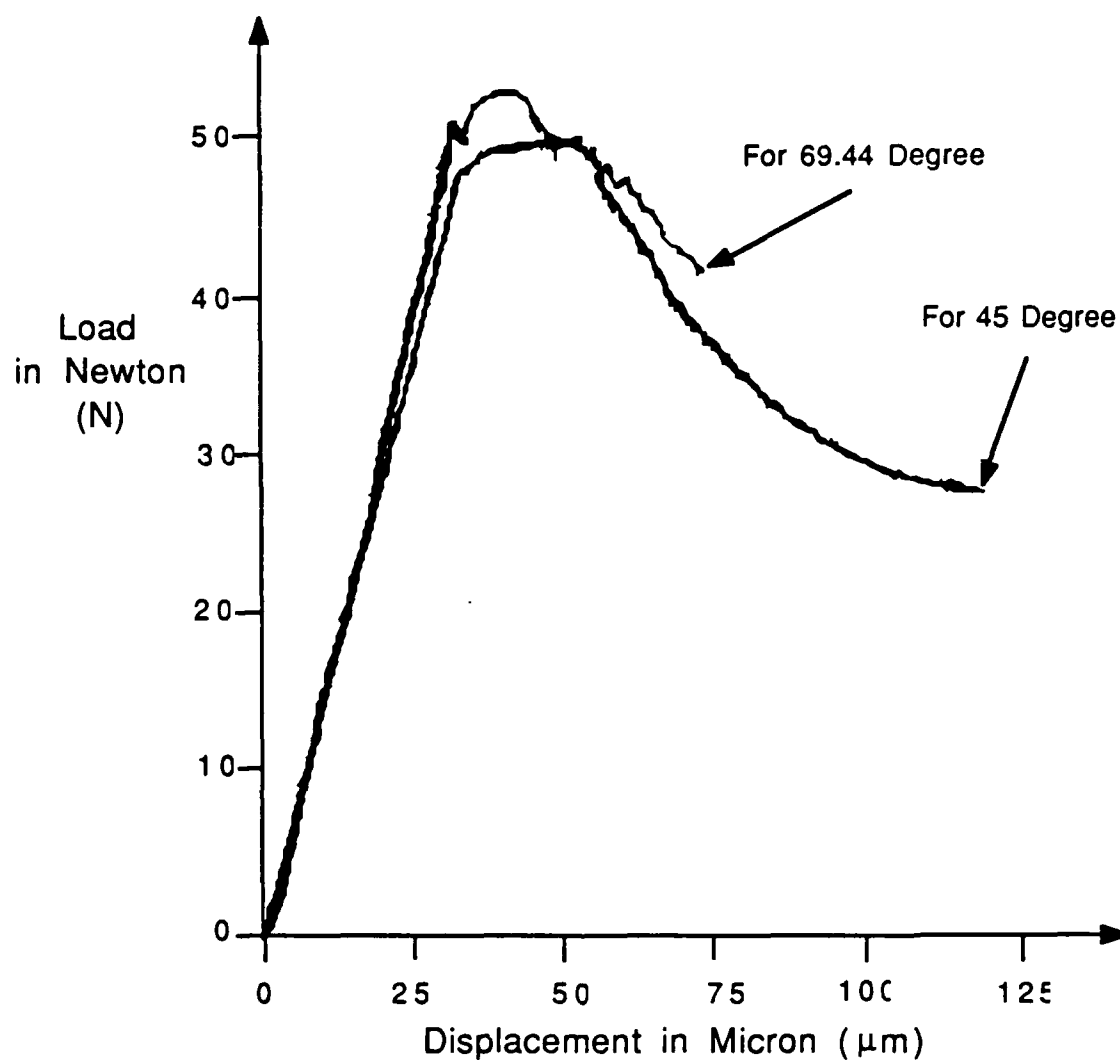


FIGURE 13: Influence of the Chevron Notch Angle on Load-Displacement Curves of 15 Vol.% Tateho SiC Whisker/Aluminum Oxide Matrix Composite at Room Temperature.

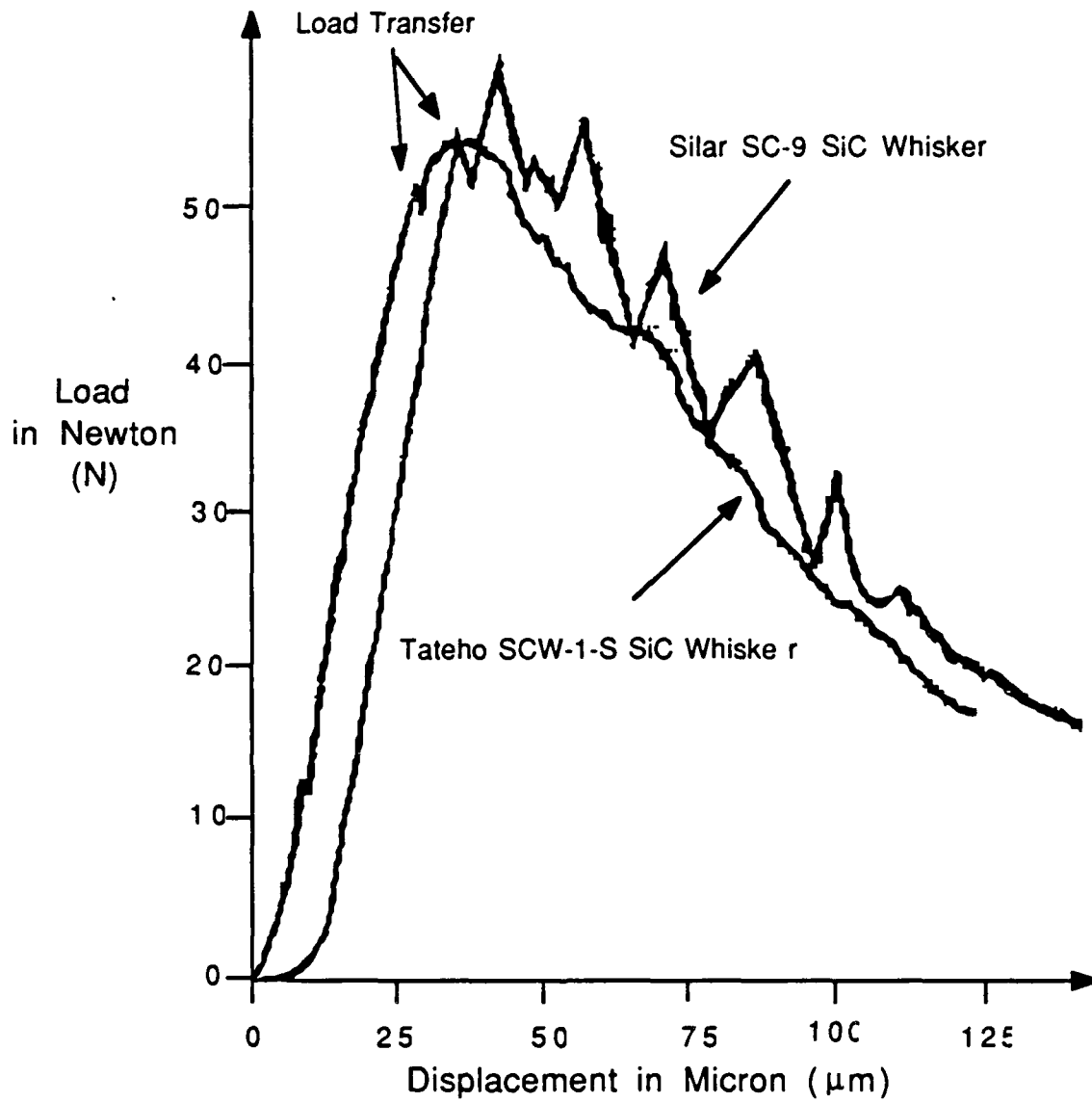


FIGURE 14: Influence of SiC Whisker Type on Load-Displacement Curve for 30 Vol.% SiC Whisker/ Aluminum Oxide Matrix Composite at Room Temperature.

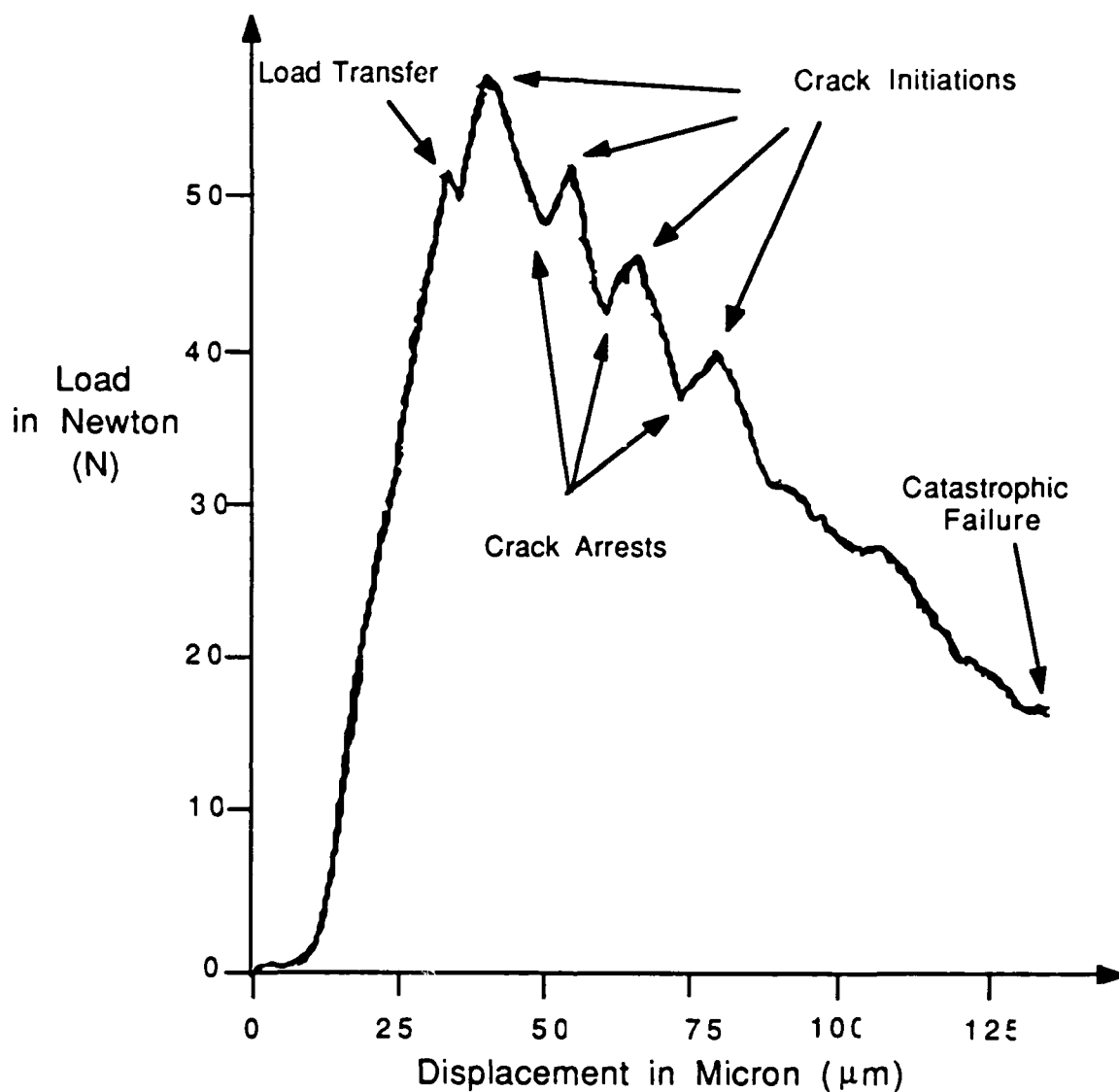


FIGURE 15: Typical Saw Tooth Behavior of a Load-Displacement Curve for 30 Vol.% Silar SiC Whisker/ Aluminum Oxide Matrix Composite at Room Temperature.



of crack arrest and crack initiation. At this point, it is interesting to notice the similarities between FIGURE 15 and the diagram in FIGURE 3.

#### IV.C.1.c. R-Curve Calculation

##### IV.C.1.c.1. Introduction

It was possible to calculate a R-curve for all of the materials tested using the method described in section II.D.4.e. An increase of fracture toughness of a material as a function of crack length reveals that the resistance of the material to crack propagation increases with increasing crack length. From the engineering point of view, this behavior is very important in order to avoid catastrophic failure and to provide the necessary mechanical reliability.

##### IV.C.1.c.2. Tateho SCW-1-S SiC Whisker/ $\text{Al}_2\text{O}_3$ Matrix Composites

In the case of Tateho SCW-1-S SiC whisker/ $\text{Al}_2\text{O}_3$  matrix composites, the R-curves generated were flat, regardless of the whisker content. However, the values of the fracture toughness varied depending on the whisker contents. FIGURE 16 presents the fracture toughness as a function of relative crack length. The higher value of  $4.5 \text{ MPa}\cdot\text{m}^{1/2}$  was obtained for the composite containing 15 volume percent SiC whiskers. Fracture toughness values of 4.2 and  $2.2 \text{ MPa}\cdot\text{m}^{1/2}$  were measured for the composites containing 30 and

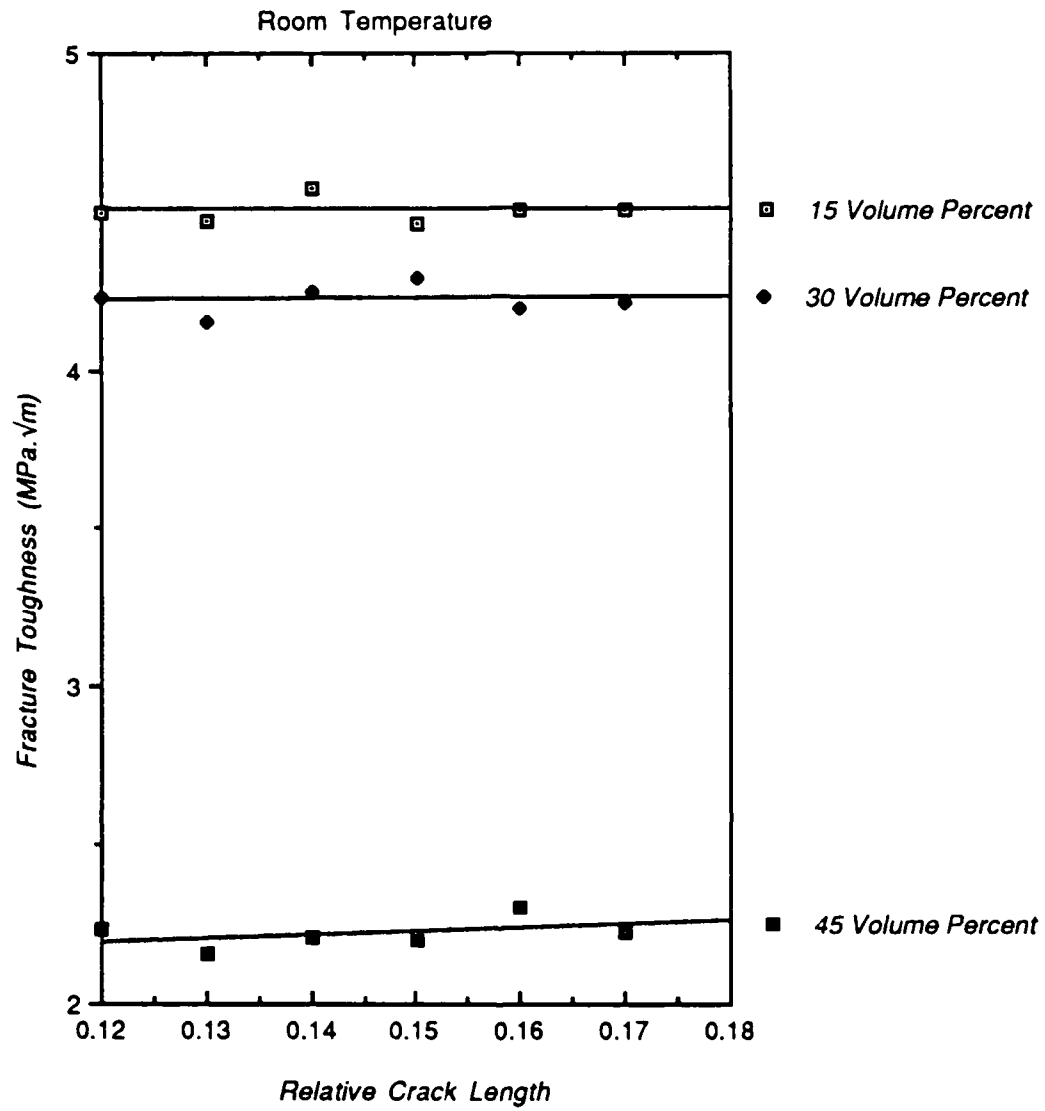


FIGURE 16: R-Curve Behavior as a Function of Whisker Content in Tateho SiC Whisker/ $\text{Al}_2\text{O}_3$  Matrix Composites.

45 volume percent SiC whiskers, respectively. The flat R-curves can be explained by the fact that little or even no toughening mechanisms were activated during the opening of the crack. For the composite fabricated with 45 volume percent SiC whiskers, the fracture toughness of the composite became inferior to that of the monolithic  $\text{Al}_2\text{O}_3$  ( $K_{IC} = 4.0 \text{ MPa}\cdot\text{m}^{1/2}$ ). The low fracture toughness value can be explained by the fact that the composite was not fabricated to full density.

#### IV.C.1.c.3. Silar SC-9 SiC Whisker/ $\text{Al}_2\text{O}_3$ Matrix Composites

Opposite to the previous case, the Silar SC-9 SiC whisker/ $\text{Al}_2\text{O}_3$  matrix composites generated rising R-curves. The saw tooth curves allowed for the calculation of two R-curves for each composite; a R-curve of arrest and a R-curve of initiation. To each point of initiation corresponded a point of arrest, until the last initiation, where the crack propagated catastrophically (see FIGURE 17). In agreement with the derivation of the R-curve calculation, the arrest curves were associated with lower values of fracture toughness than the initiation curves. For the same composite, the increase in fracture toughness as a function of relative crack length had more influence in the case of the initiation of the crack than in its arrest.

FIGURE 18 shows the R-curves of crack initiation for composites fabricated with 15, 30, and 45 volume percent SiC whiskers. The toughening mechanisms responsible for the rising R-curves were active in the wake region of the crack. They were

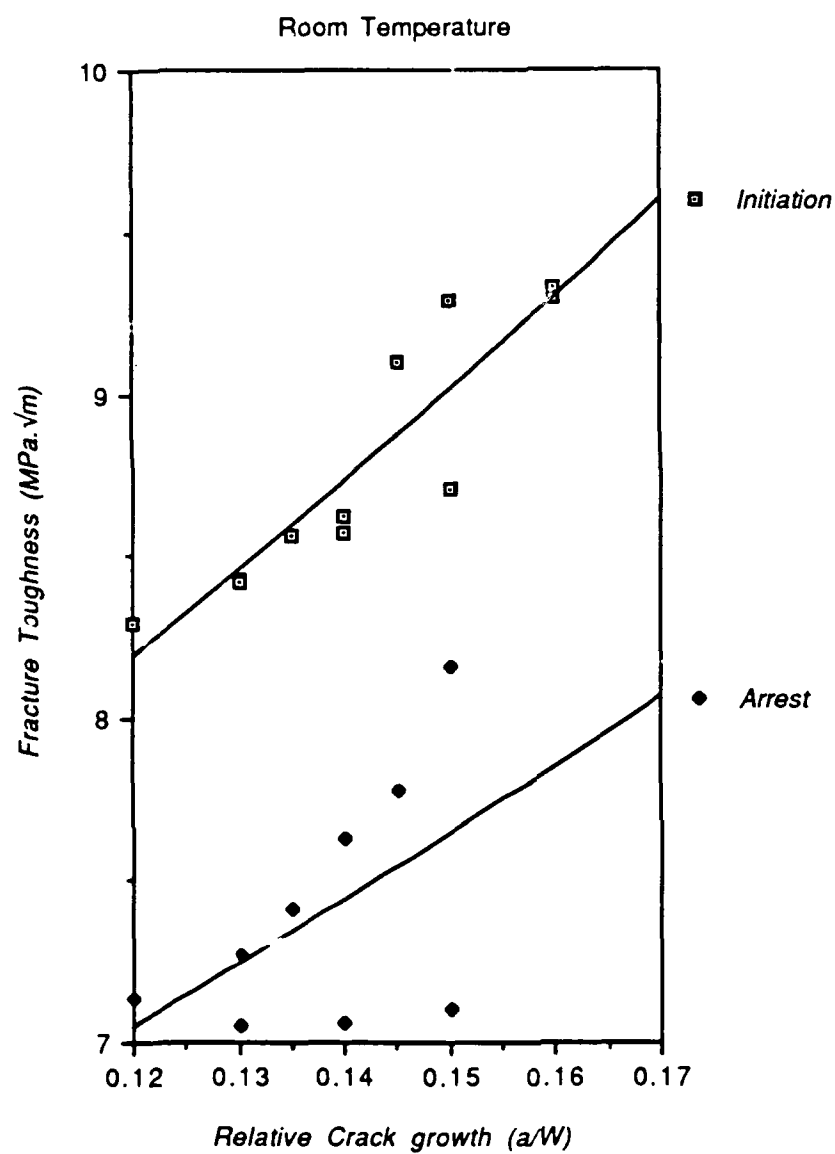


FIGURE 17: R-Curve Behavior in 30 Vol.% Silar SiC Whisker/ $\text{Al}_2\text{O}_3$  Matrix Composites

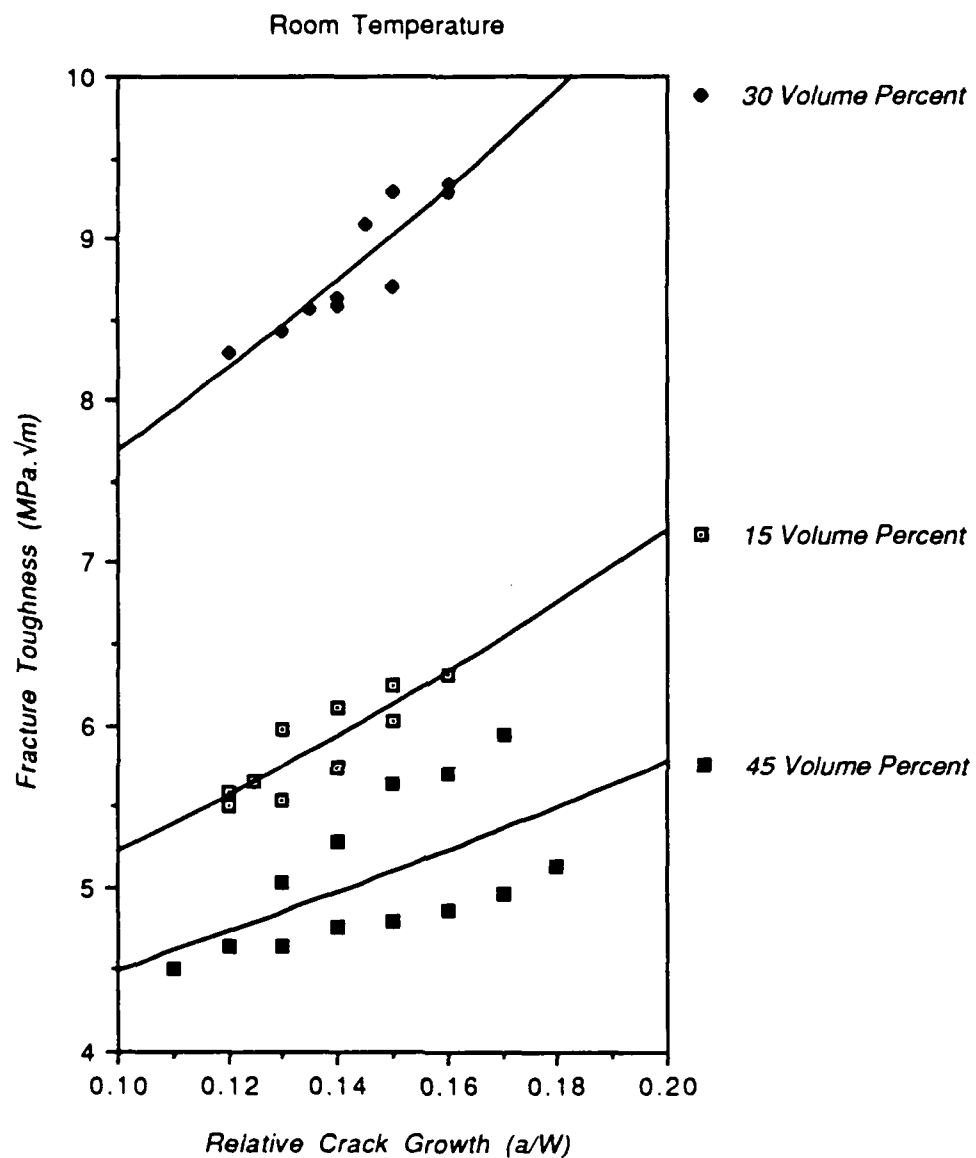


FIGURE 18: R-Curve Behavior by Initiation as a Function of Whisker Content in Silar SiC Whisker/ $\text{Al}_2\text{O}_3$  Matrix Composites.

primarily associated with whisker bridging and whisker pullout. This phenomenon was proportional to the amount of fibers present in the composites. The composite fabricated with 30 volume percent SiC whiskers showed a R-curve with higher fracture toughness values than the composite fabricated with 15 volume percent SiC whiskers. The composite fabricated with 45 volume percent SiC whiskers was an exception to this effect. The large whisker content had a negative effect on the fracture toughness. It is believed that during the processing of the composites the whiskers had a tendency to agglomerate together. These whisker agglomerates apparently weakened the composite and consequently decreased the fracture toughness.

#### IV.C.2. High Temperature Testing

##### IV.C.2.a. Load-Displacement Curves

The load-displacement curves at high temperature (1000°C) showed different behavior for the composites fabricated with the two types of whiskers. In the case of the Tateho SCW-1-S SiC whisker/ $\text{Al}_2\text{O}_3$  matrix composites, the load-displacement curves represented stable crack growth with a quasi-continuous behavior. For the Silar SC-9 SiC whisker/ $\text{Al}_2\text{O}_3$  matrix composites, a saw tooth shape to the curves was observed. In this particular case, the arrest points were difficult to identify (See FIGURE 19). This resulted in a certain lack of accuracy in the calculation of the arrest R-curve. FIGURE 20 illustrates the load-displacement curves for

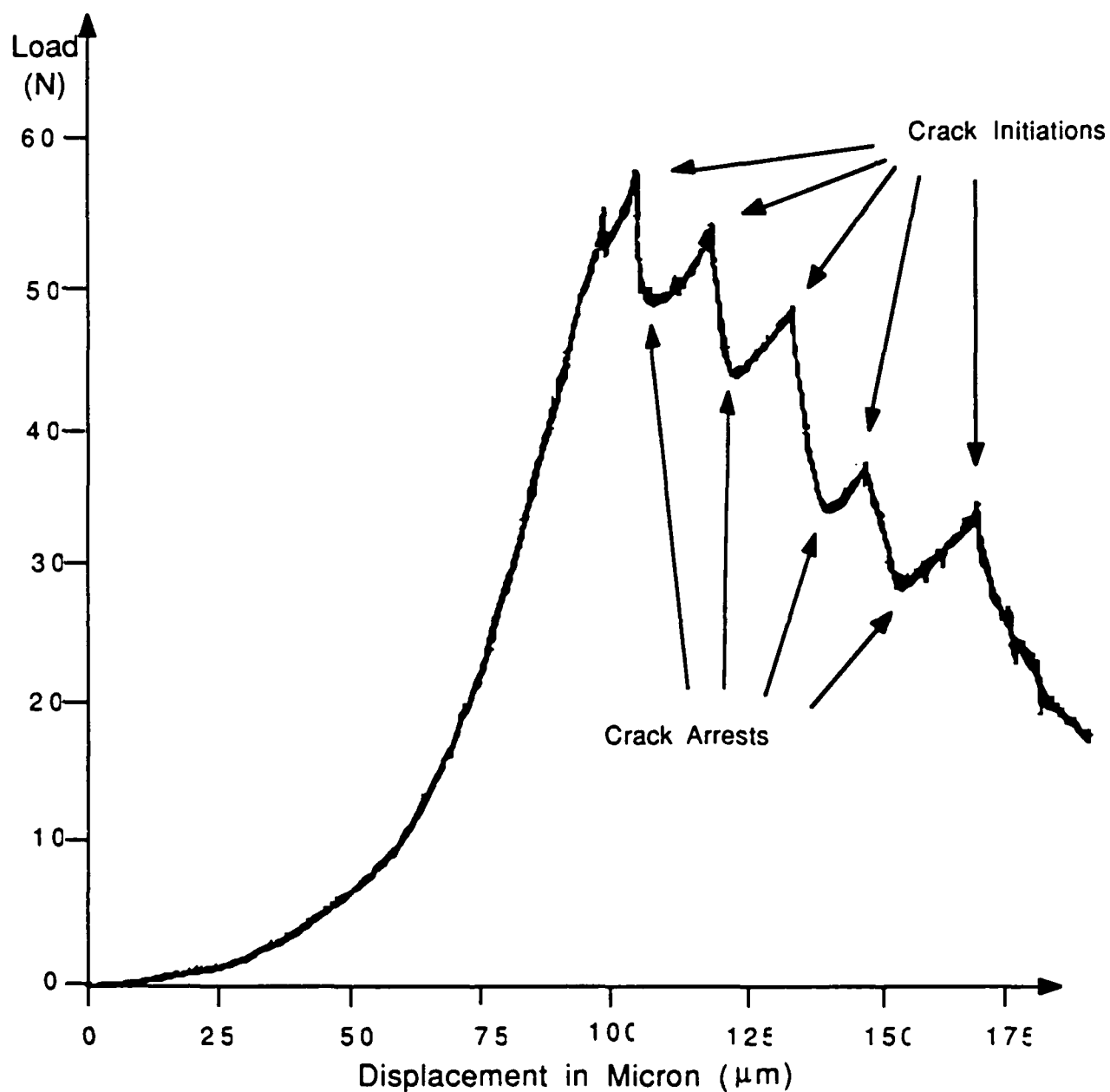


FIGURE 19: Typical Saw Tooth Behavior Of Load-Displacement Curves For 30 Vol.% Silar SiC/Alumina Matrix Composite at 1000 degree Celsius.

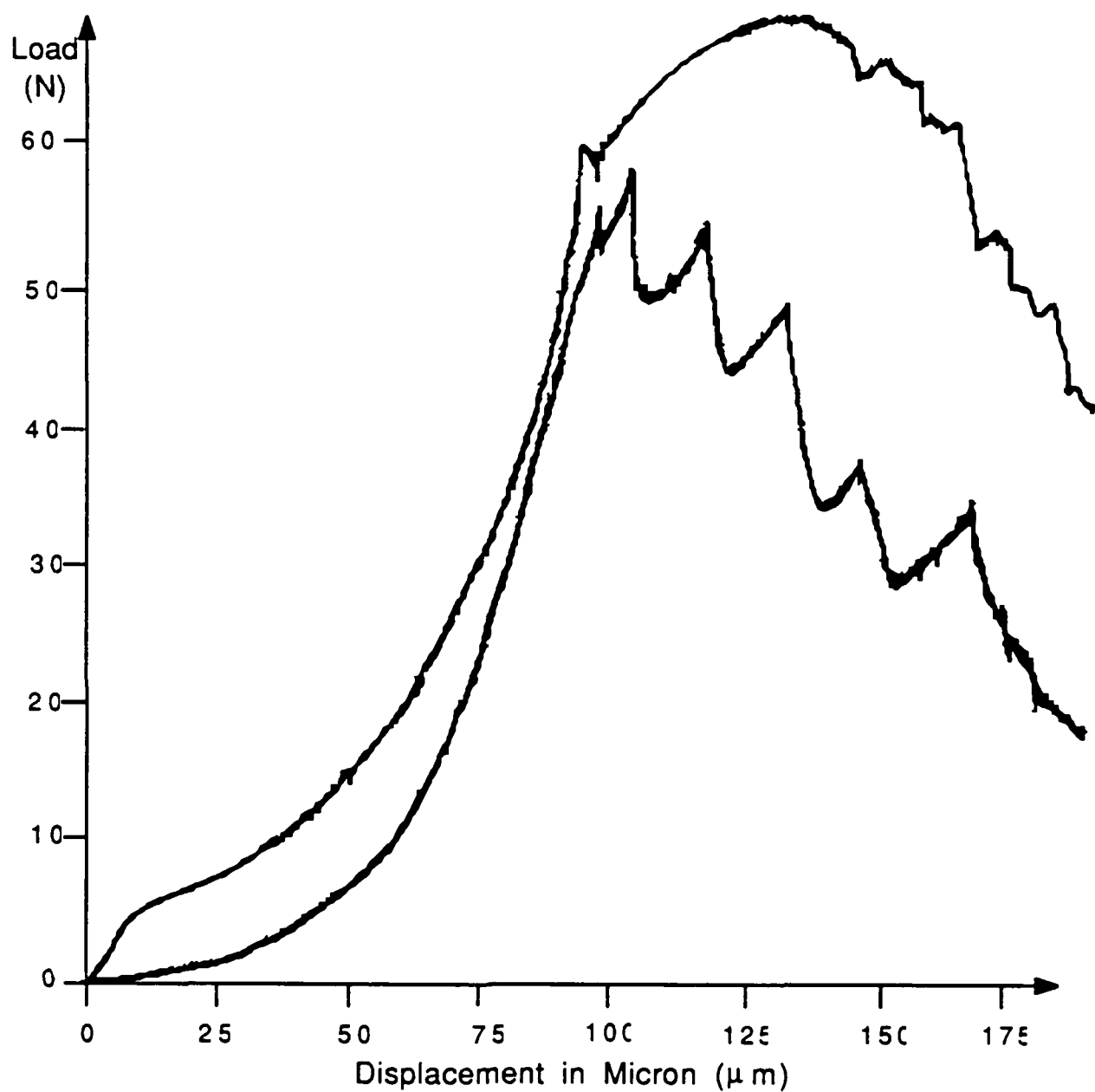


FIGURE 20: Influence of SiC Whisker Type on Load-Displacement Curves for 30 Volume Percent SiC Whisker/Aluminum Oxide Matrix Composite at 1000 Degree Celsius.



composites fabricated with the two types of whiskers involved in this study.

#### IV.C.2.b. R-Curve Calculation

##### IV.C.2.b.1. Introduction

In parallel to the room temperature R-curve measurements, the calculation of the R-curves at high temperature (1000°C) was different depending on the whisker type. For the composites fabricated with Tateho SCW-1-S SiC whiskers, the load-displacement curves did not allow for the separation of the initiation and arrest points. In consequence, only one R-curve was generated per composite. With the composites fabricated with the Silar SC-9 SiC whiskers, two R-curves were calculated per composite. All mechanical testing was performed only with specimens having  $\theta = 45^\circ$ . This choice was in agreement with the stability of the crack observed in the experiments at room temperature.

At this point, it is important to state that the an artifact phenomenon had to be taken into account. The compliance of the fixture was no longer negligible in comparison with the sample compliance. A numerical correction was required in the R-curve calculation to reach the true values of the fracture toughness. At high temperature, the compliance of the fixture was estimated to be of the same order of magnitude as the sample compliance.

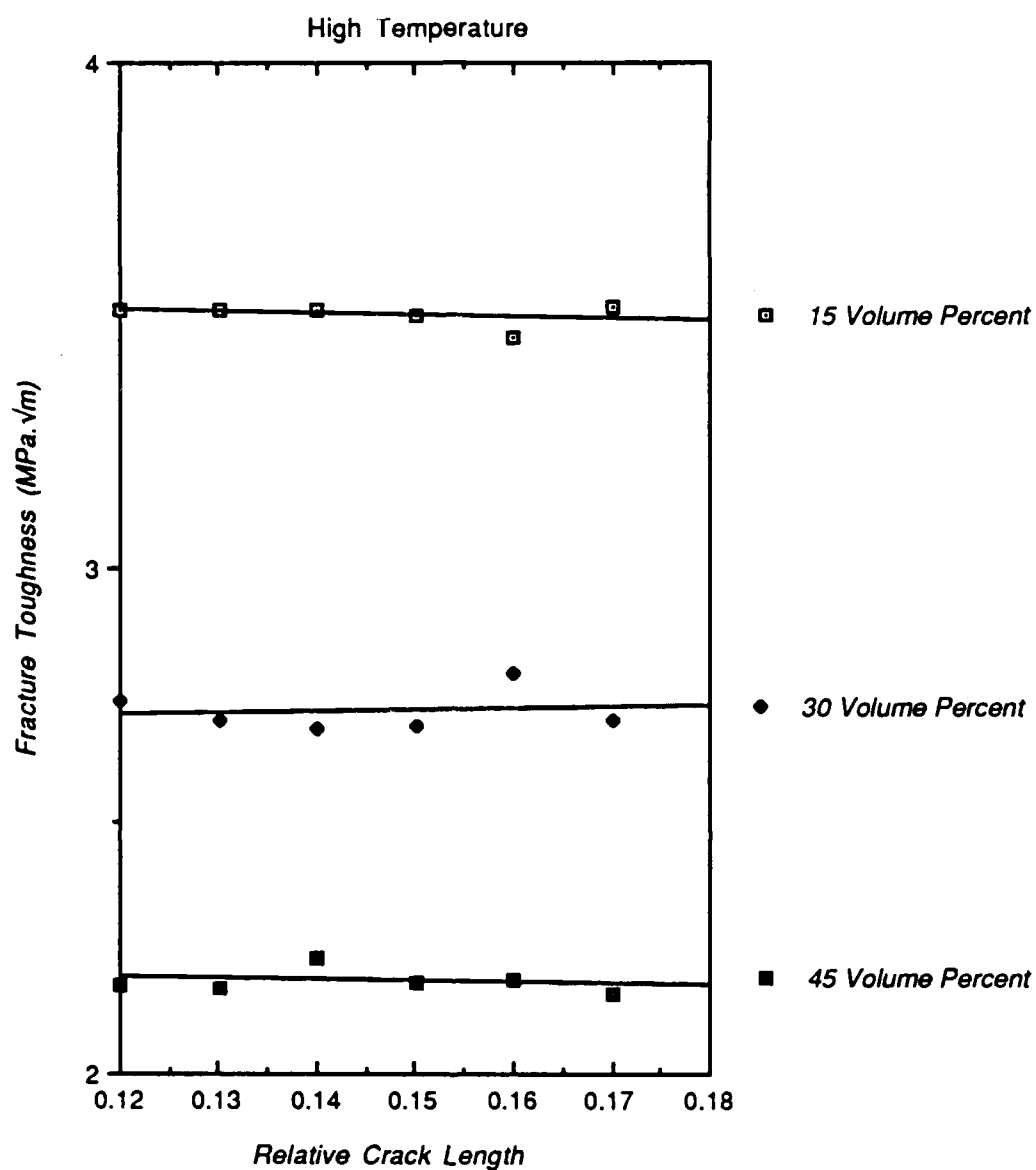


FIGURE 21: R-Curve Behavior as a Function of Whisker Content in Tateho SiC Whisker/Al<sub>2</sub>O<sub>3</sub> Matrix Composites.

#### IV.C.2.b.2. Tateho SCW-1-S SiC Whisker/ $\text{Al}_2\text{O}_3$ Matrix Composites

The results of the fracture toughness calculations as a function of the relative crack length indicated flat R-curves for the composites fabricated with the Tateho SCW-1-S SiC whiskers. The values of the fracture toughness decreased as the whisker content increased. FIGURE 21 illustrates this trend. The three values are all below the fracture toughness of monolithic  $\text{Al}_2\text{O}_3$  ( $K_{IC} = 4.0 \text{ MPa}\cdot\text{m}^{1/2}$ ) at room temperature. For increasing whisker contents, the values of the fracture toughness are respectively 3.5, 2.7, and  $2.2 \text{ MPa}\cdot\text{m}^{1/2}$ .

#### IV.C.2.b.3. Silar SC-9 SiC Whisker/ $\text{Al}_2\text{O}_3$ Matrix Composites

At high temperature, the Silar SC-9 SiC whisker/ $\text{Al}_2\text{O}_3$  matrix composites exhibited rising R-curve behavior. This was visible in both the arrest and initiation R-curves. Similar to the room temperature results, the initiation curves were associated with higher values of fracture toughness than the arrest curves (see FIGURE 22).

FIGURE 23 shows the R-curves of crack initiation for composites fabricated with 15, 30, and 45 volume percent SiC whiskers. The fracture toughness values were typically in the range of  $6.5$  to  $7.5 \text{ MPa}\cdot\text{m}^{1/2}$  for the composite with 30 volume percent SiC whiskers. For the composites fabricated with 30 and 45 volume percent SiC whiskers, the fracture toughness fluctuated around  $4.5 \text{ MPa}\cdot\text{m}^{1/2}$ . For the composite fabricated with 45 volume percent SiC

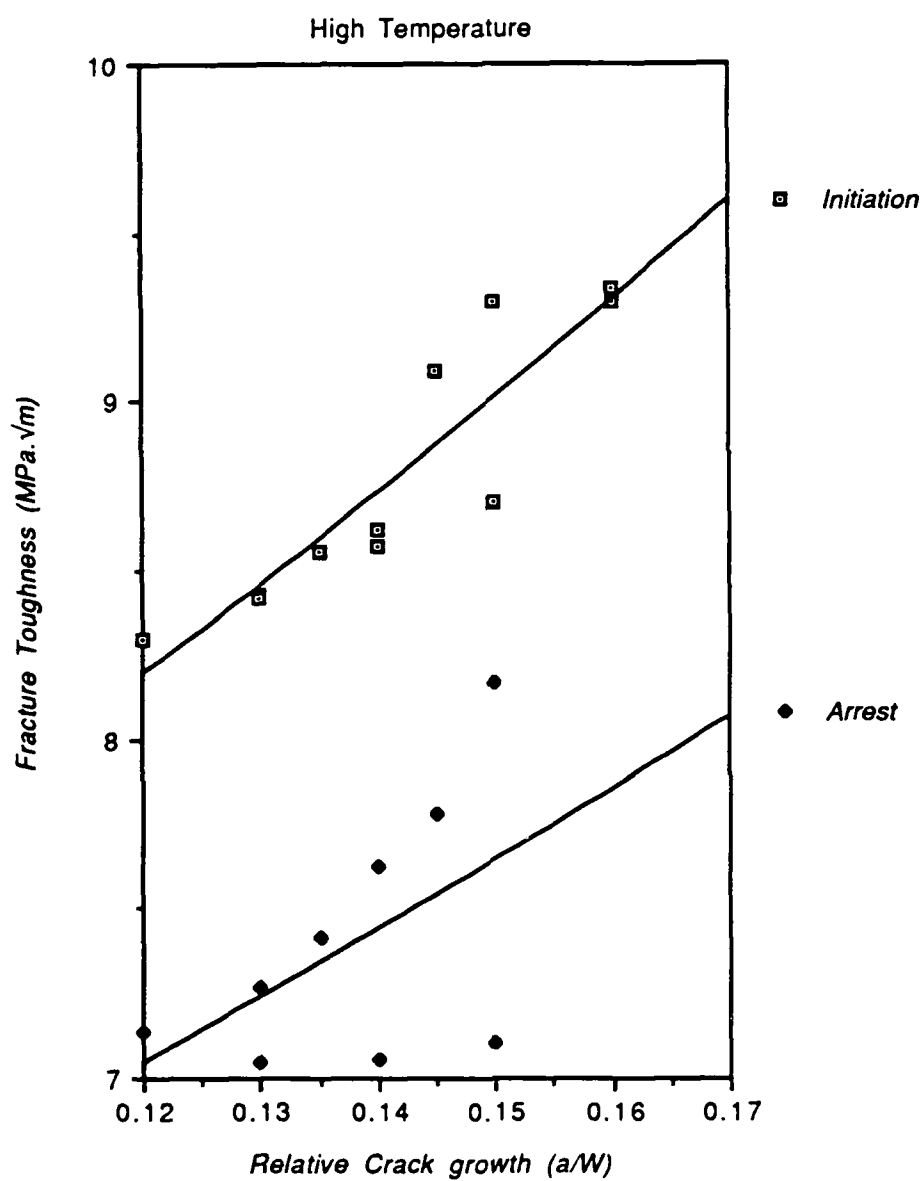


FIGURE 22: R-Curve Behavior of 30 Vol.% Silar SiC Whisker/ $\text{Al}_2\text{O}_3$  Matrix Composite.

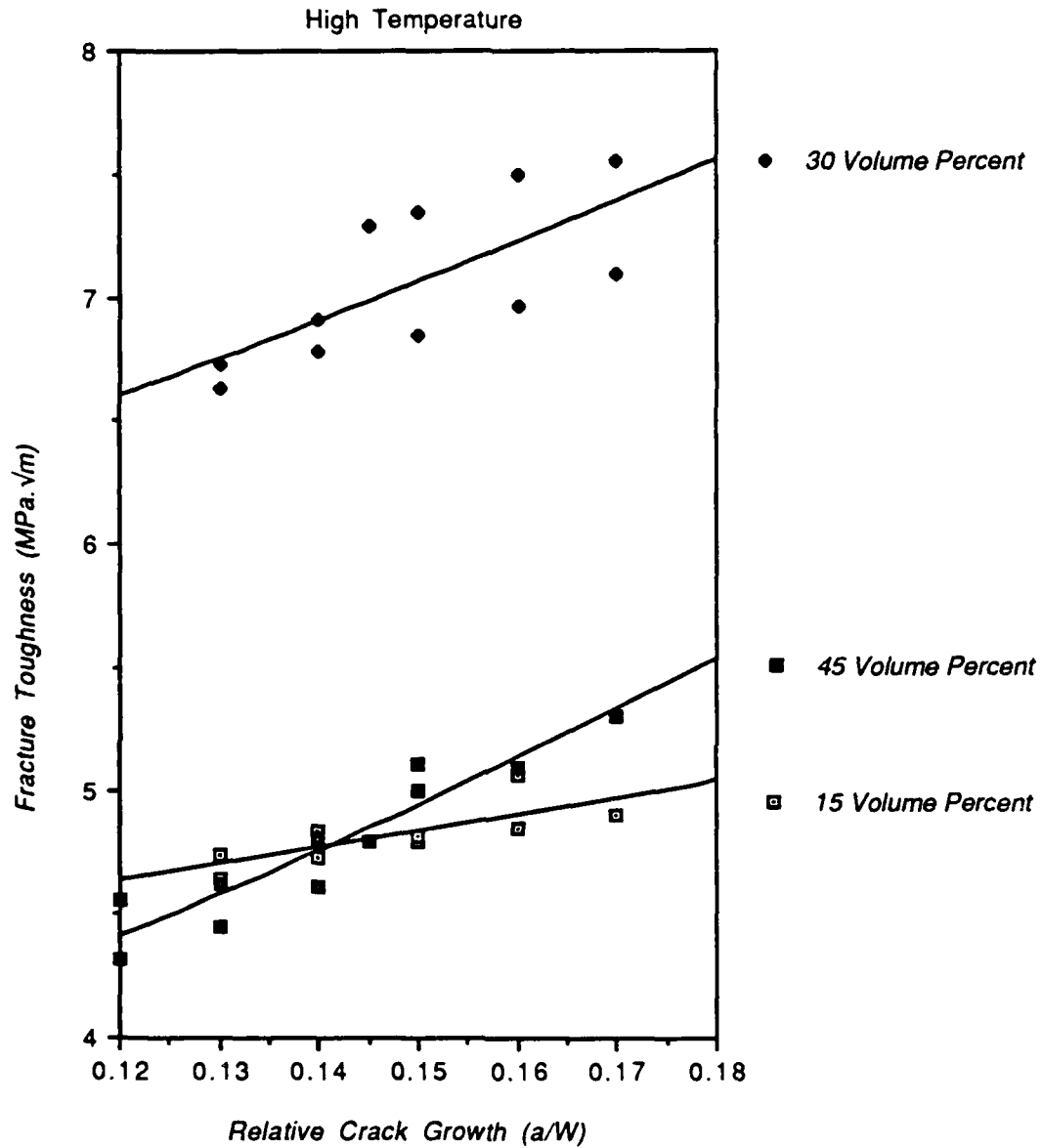


FIGURE 23: R-Curve Behavior by Initiation as a Function of Whisker Content in Silar SiC Whisker/ $\text{Al}_2\text{O}_3$  Matrix Composites.

whiskers, the initiation R-curve began with the lowest value of fracture toughness among the different composites, but because the rising effect was greater than that of the composite fabricated with 15 volume percent SiC whiskers after 0.14 relative crack length. This phenomenon was seen only at high temperature.

#### IV.C.3. Comparison of The Results as a Function of Temperature

##### IV.C.3.a. Load-Displacement Curves

FIGURE 24 illustrates the different load-displacement curves obtained at 25°C and 1000°C with 45 volume percent Silar SC-9 SiC/Al<sub>2</sub>O<sub>3</sub> matrix composites. As described in sections IV.C.1.b. and IV.C.2.a., the saw tooth shape of the curves was seen at both room temperature and high temperature. The same shape of the curves implies that the predominant phenomenon in resisting the propagation of the crack was of the same nature independent of the temperature. To be more precise, it can be said that the same toughening mechanisms operating at room temperature were still present at 1000°C. But it is incorrect to say that those toughening mechanisms responsible for the rising R-curves had the same influence on the composite at the different temperatures. FIGURE 24 shows a maximum load at about 53 N for the room temperature curve and 25 N at high temperature. Also at high temperature, the saw tooth shape was less sharp compared to the one at room temperature. This affected the crack arrest points to a greater

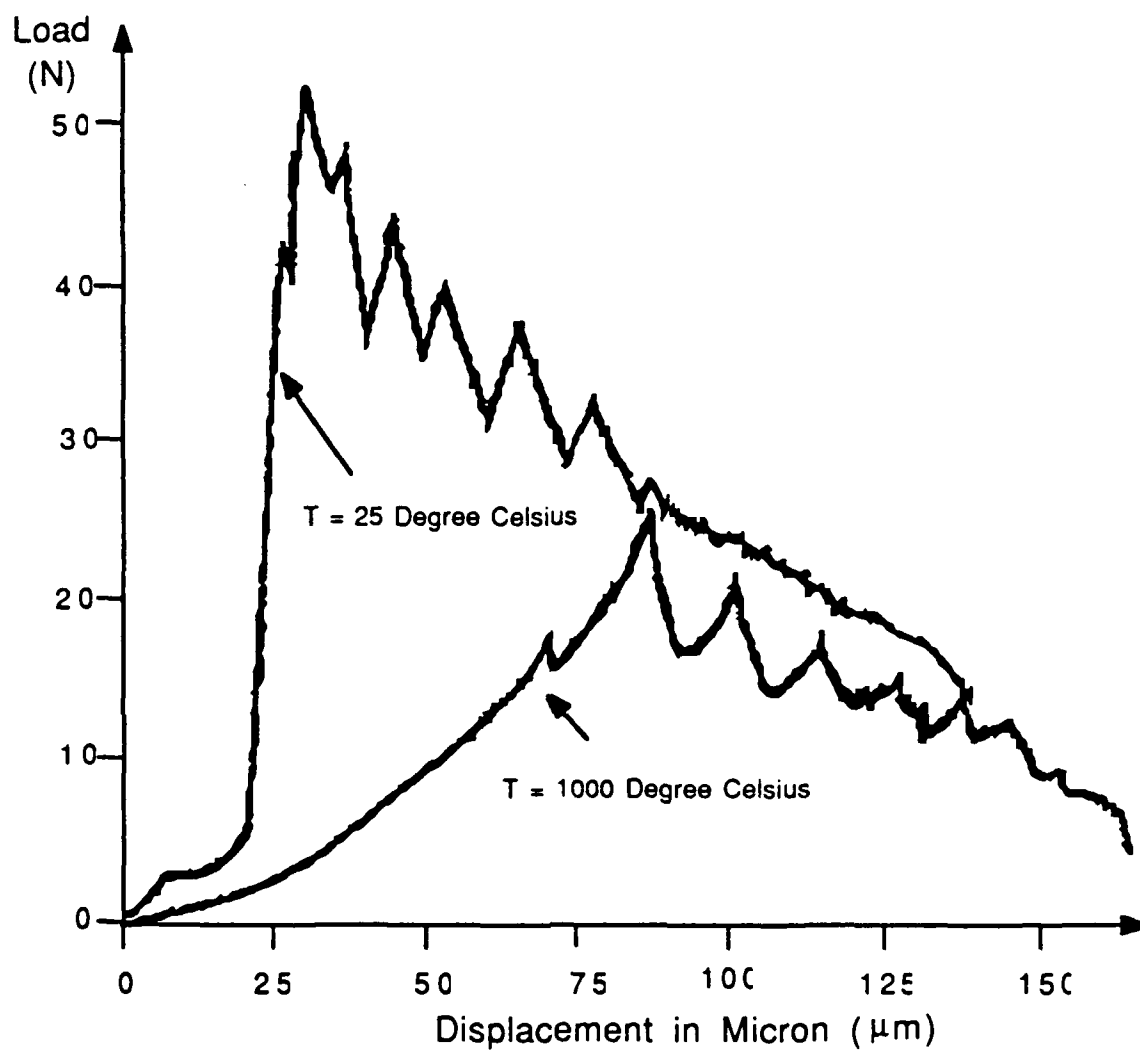


FIGURE 24: Effect of Temperature on the Load-Displacement Curves for 45 Vol.% Silar SiC/Aluminum Oxide Matrix Composite.

extent than the crack initiation points. The behavior suggests that the material was less brittle at the higher temperature.

#### IV.C.3.b. Effect of Whisker Content

##### IV.C.3.b.1. Tateho SCW-1-S SiC Whiskers

As seen in FIGURE 25 and TABLE 17, the optimum value of the fracture toughness was reached with 15 volume percent SiC whiskers at both room and high temperatures, 4.5 MPa.m<sup>1/2</sup> and 3.5 MPa.m<sup>1/2</sup>, respectively. The room temperature R-curves were at a higher level of fracture toughness than the corresponding ones at high temperature, except for the composite fabricated with 45 volume percent SiC whiskers. In this case, both room and high temperature fracture toughness levels were similar, approximately 2.2 MPa.m<sup>1/2</sup>. The defects due to low density and also due to the difficulty of dispersing whisker agglomerates during processing were responsible for these low values. The defects primarily limit the toughening behavior of these composites.

For both temperatures, the flat R-curves appeared at lower levels as the whisker content increased. The behavior of the composite fabricated with 30 volume percent SiC whiskers distinctly illustrates the different toughening behavior seen at the two temperatures. At room temperature, the fracture toughness was above that of monolithic Al<sub>2</sub>O<sub>3</sub>, 4.2 MPa.m<sup>1/2</sup> compared to 3.9 MPa.m<sup>1/2</sup>. At high temperature, the fracture toughness was below that of monolithic Al<sub>2</sub>O<sub>3</sub>, 2.7 MPa.m<sup>1/2</sup> compared to 3.22 MPa.m<sup>1/2</sup>.



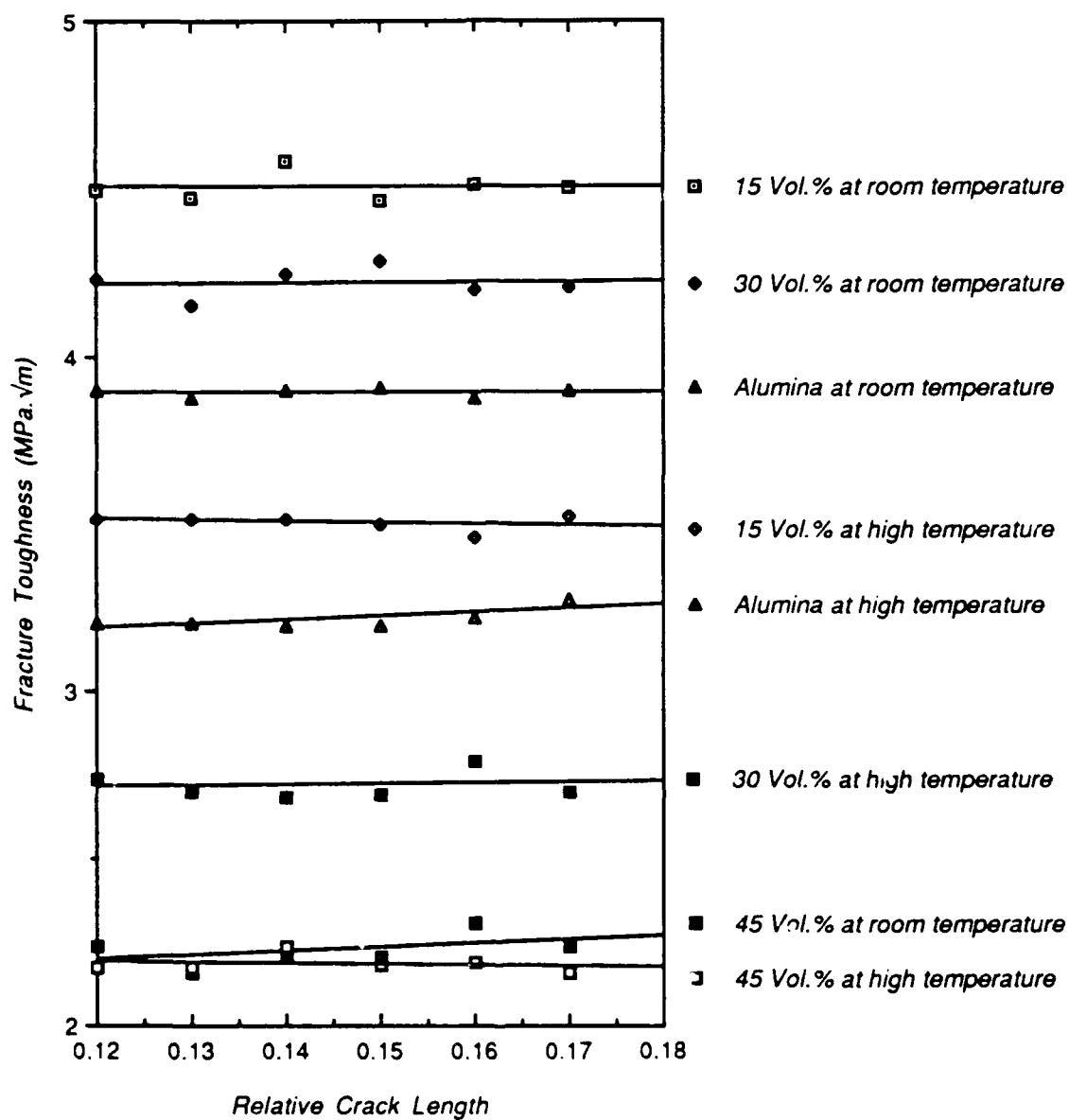


FIGURE 25: R-Curve Behavior as a Function of Whisker Content and Temperature in Tateho SiC Whisker/ $\text{Al}_2\text{O}_3$  Matrix Composites.

TABLE 17  
Summary of Fracture Toughness Values (MPa.m<sup>1/2</sup>)  
For SiC Whisker/Al<sub>2</sub>O<sub>3</sub> Matrix Composites.

Vol.% SiC	0	15	30	45
Silar SC-9				
Initiation				
25°C	3.90	5.50-6.32	8.30-9.33	4.50-5.95
1000°C	3.22	4.64-5.01	6.63-7.55	4.32-5.30
Arrest				
25°C	3.90	4.48-5.57	7.05-8.16	3.93-4.41
1000°C	3.22	3.46-4.26	5.25-5.90	2.98-4.01
Tateho SCW-1-S				
25°C	3.90	4.50	4.20	2.20
1000°C	3.22	3.50	2.70	2.170

For this particular whisker content, this observation means that the effect of whisker additions does not have an intrinsic relationship with the fracture toughness which is characteristic of the composite. The phenomenon was primarily related to the mismatch of thermal expansion between the  $\text{Al}_2\text{O}_3$  matrix and the SiC whiskers. During hot pressing, the matrix was prestressed by the whiskers. For room temperature testing, this prestressing resulted in the activation of toughening mechanisms related to crack deflection. For high temperature testing, the prestressing of the matrix was essentially released. The composite could then be viewed as a monolithic  $\text{Al}_2\text{O}_3$ , with defects represented by whisker inclusions. It can be easily seen that the effect of prestressing of the matrix was balanced by the effect of the whisker defects. With 15 volume SiC whiskers, the influence of the whiskers as defect sources was limiting, but not predominant compared to the prestressing effect.

#### IV.C.3.b.2. Silar SC-9 SiC Whiskers

In the case of Silar SC-9 SiC whisker/ $\text{Al}_2\text{O}_3$  matrix composites, all the R-curves were rising. There was an increase in fracture toughness as the crack propagated in the composites. For the crack to propagate, the opening of the two surfaces which characterized the crack required more energy as more free surfaces were generated. The composite, at all three whisker contents, had a fracture toughness superior to monolithic  $\text{Al}_2\text{O}_3$ , independent of the testing temperature. For the composites fabricated with 15 and 30

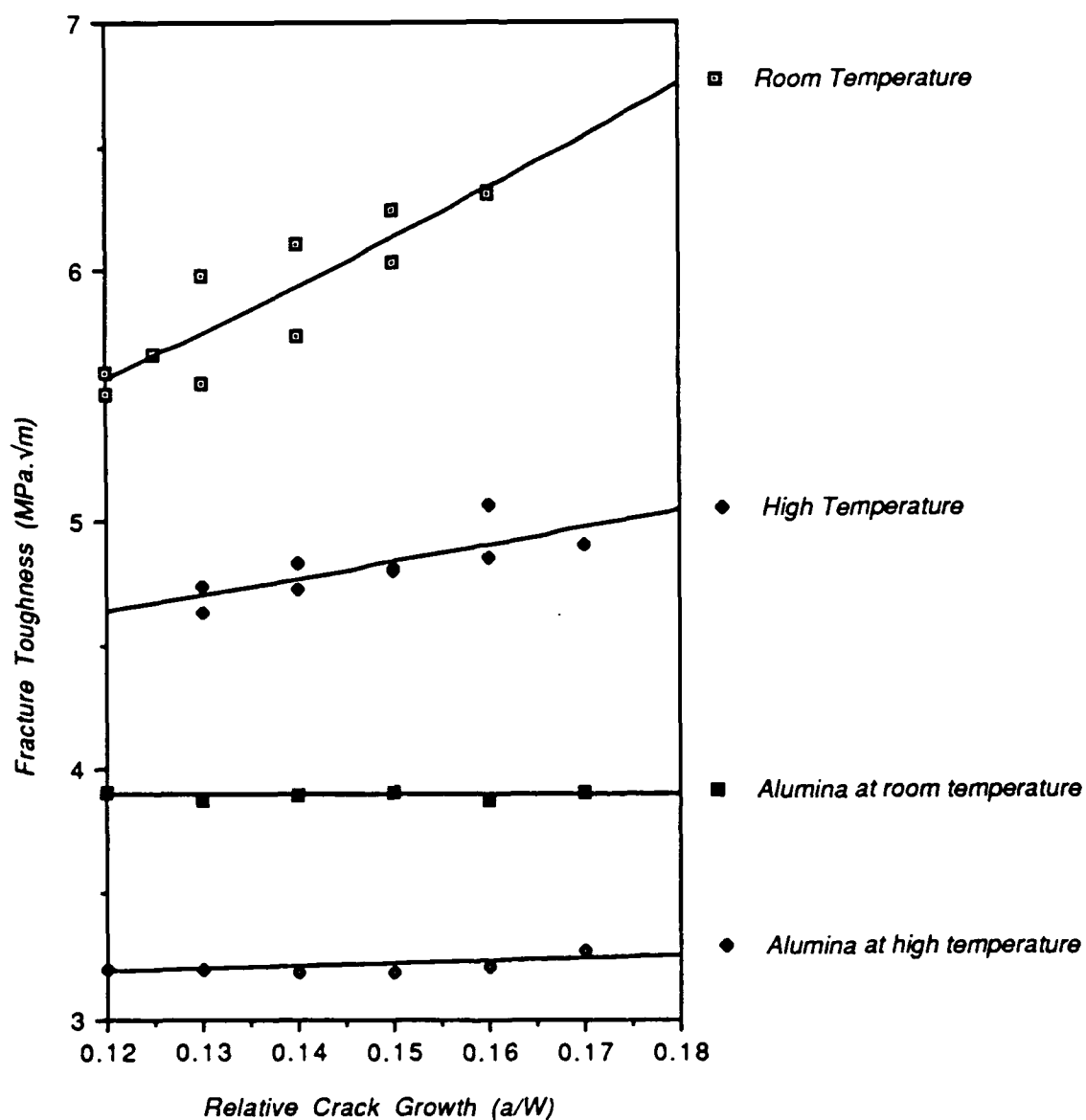


FIGURE 26: Effect of Temperature on the R-Curve Behavior by Initiation in 15 Vol.% Silar SC-9 SiC Whisker/ $\text{Al}_2\text{O}_3$  Matrix Composite.

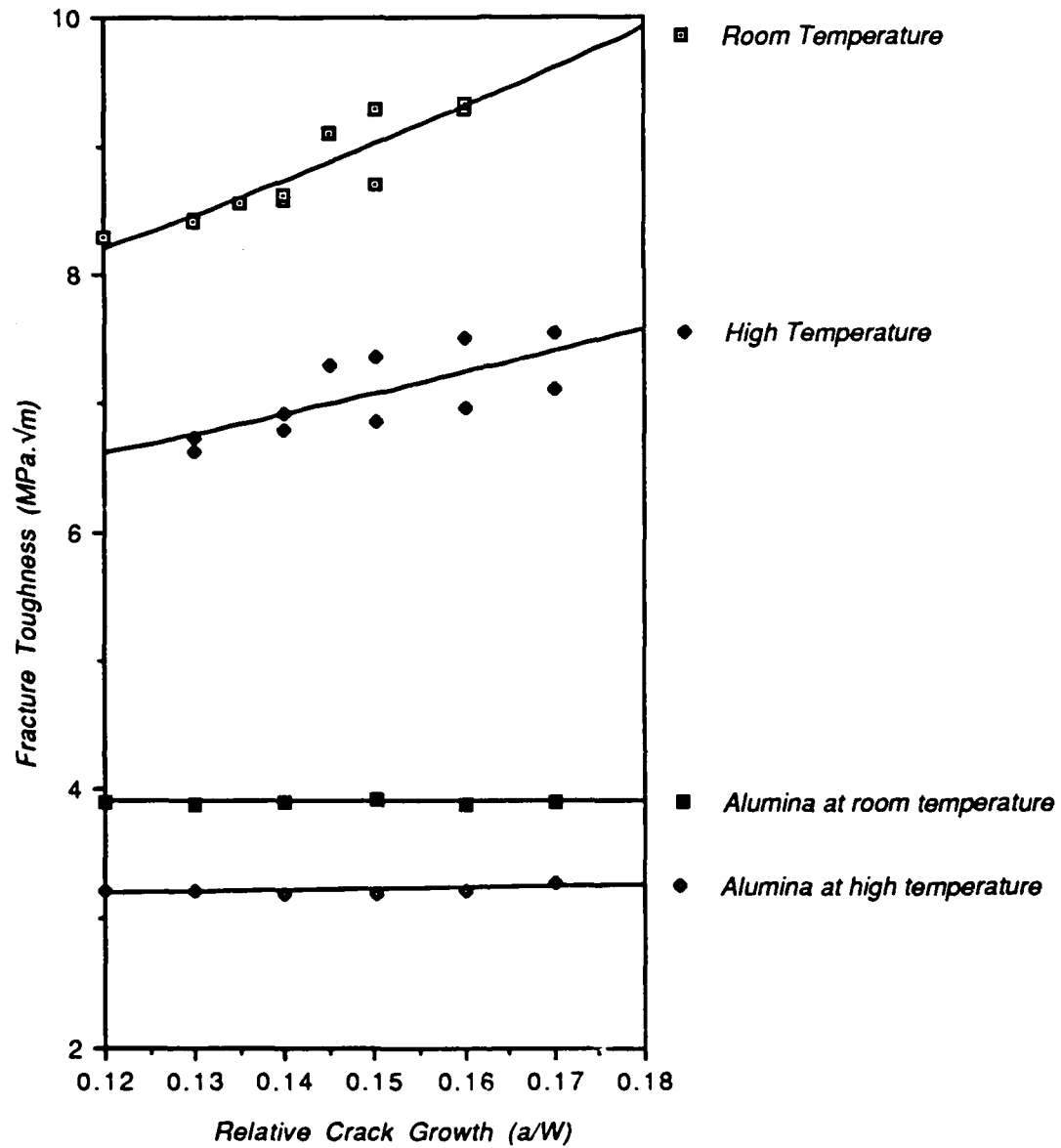


FIGURE 27: Effect of Temperature on R-Curve Behavior by Initiation in 30 Vol.% Silar SC-9 SiC Whisker/ $\text{Al}_2\text{O}_3$  Matrix Composite.

volume percent SiC whiskers, the values of fracture toughness at room temperature were superior to those at high temperature (see FIGURES 26 and 27, respectively in addition to TABLE 17). For those particular whisker contents, the increase in temperature decreased the effect of the toughening mechanisms, which were responsible for the rising R-curves. With 45 volume percent SiC whiskers, the composite had the same behavior at both temperatures. The high whisker content apparently weakened the composite as a result of whisker agglomerate formation during processing.

As a function of whisker content, the fracture toughness reached a maximum for composites fabricated with 30 volume percent SiC whiskers, regardless of the test temperature. Nevertheless, at high temperature, the R-curve for the composite fabricated with 45 volume percent SiC whiskers showed the most rapid rise in comparison to the other R-curves. FIGURE 28 reveals that at high temperature the toughening mechanisms were more effective in toughening the composite at the high whisker content as the crack propagated. It is easily seen that the ratio of the fracture toughness values of this composite, relative to monolithic  $\text{Al}_2\text{O}_3$ , gave a multiplicative coefficient of 2 at the beginning of the crack propagation and a coefficient of 3 at 20 percent of the relative crack length.

The optimum toughening behavior is clearly shown in FIGURE 29 for the composite fabricated with 30 volume percent Silar SC-9 SiC whiskers. From FIGURE 29 it can be concluded that the increase in fracture toughness was not always proportional to the whisker

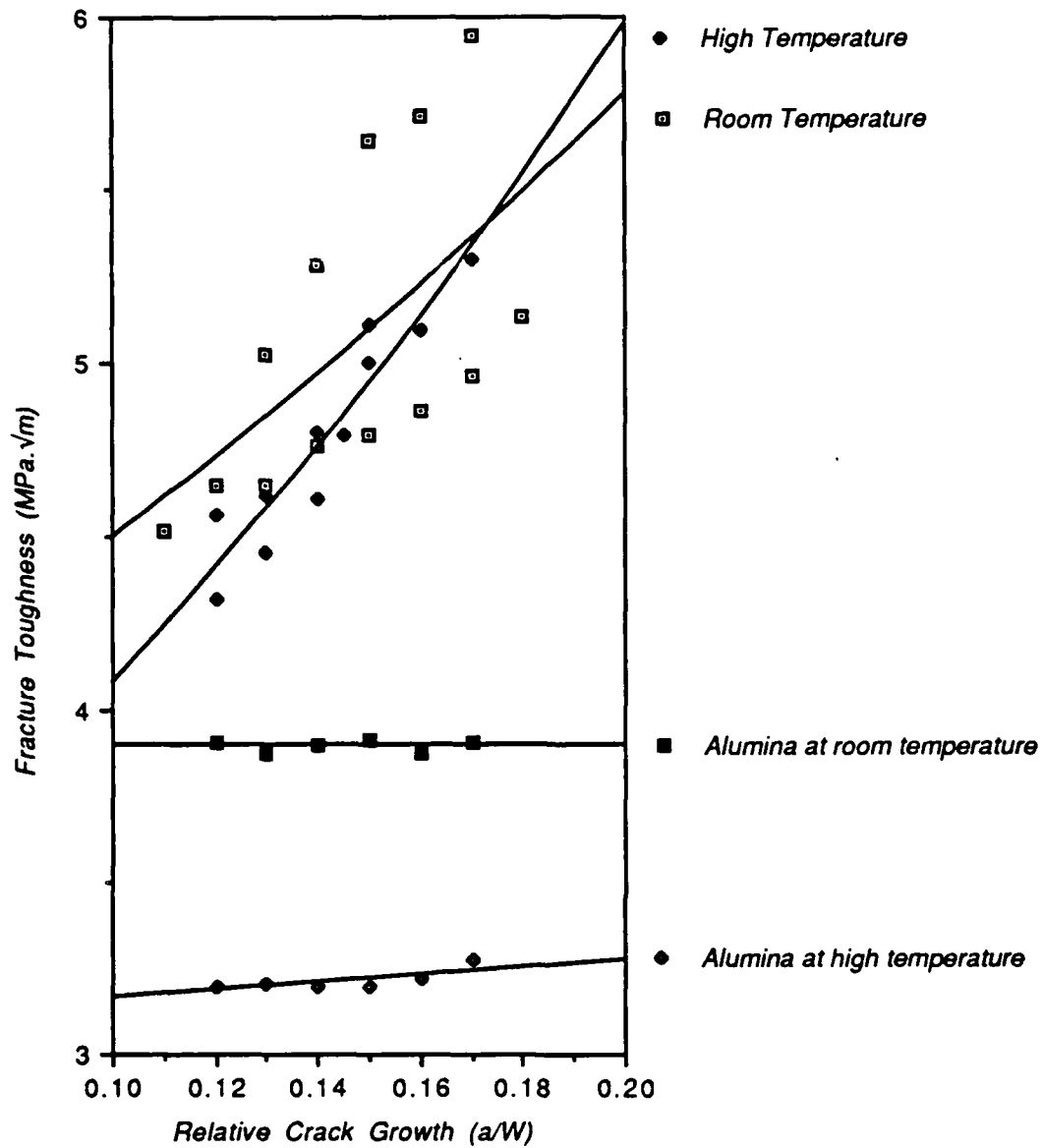


FIGURE 28: Effect of Temperature on R-Curve Behavior by Initiation in 45 Vol.% Silar SC-9 SiC Whisker/ $\text{Al}_2\text{O}_3$  Matrix Composite.

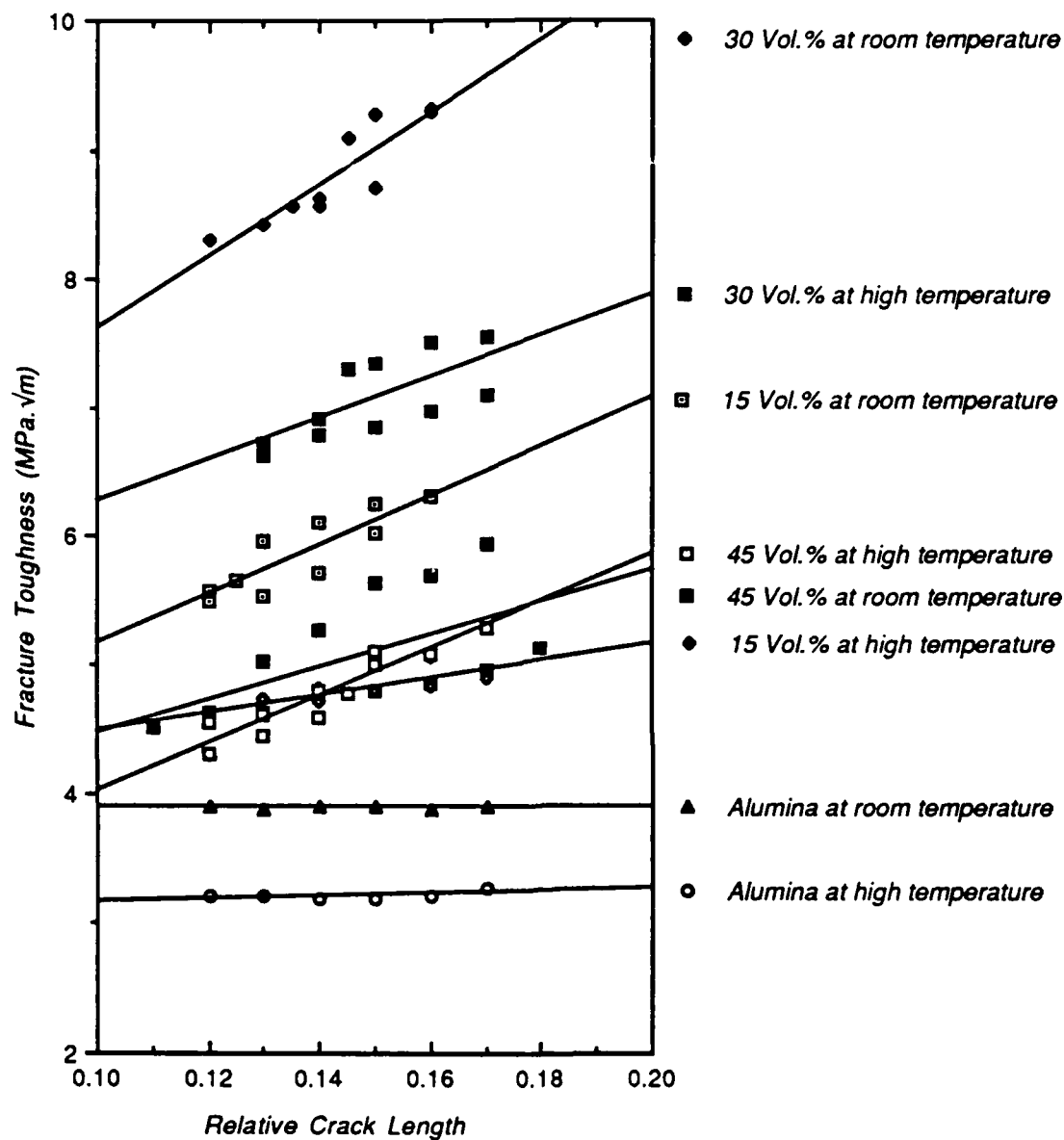


FIGURE 29: Effect of Temperature and Whisker Content on R-Curve Behavior by Initiation in Silar SC-9 SiC Whisker/ $\text{Al}_2\text{O}_3$  Matrix Composite.



content, as higher whisker contents did not necessarily mean a further increase in fracture toughness for the composite.

#### IV.C.3.c. Effect of Whisker Type

The main differences between composites fabricated with Silar SC-9 SiC whiskers and Tateho SCW-1-S SiC whiskers were related to the shape of the R-curves and the ultimate values of the fracture toughness. The Silar SC-9 SiC whisker/ $\text{Al}_2\text{O}_3$  matrix composites showed rising R-curves and the Tateho SCW-1-S SiC whisker/ $\text{Al}_2\text{O}_3$  matrix composites showed flat R-curves. This observation was not related to the mechanical properties of the whiskers themselves since they were basically equivalent<sup>3</sup>. The difference appeared in the interaction of the whiskers with the  $\text{Al}_2\text{O}_3$  matrix. Previous characterization of SiC whisker/ $\text{Al}_2\text{O}_3$  matrix interfaces was of extreme importance for understanding what toughening mechanisms were involved during the propagation of the crack(s) through the composites<sup>3</sup>. In practice, the results presented in FIGURE 25 imply that reinforcing  $\text{Al}_2\text{O}_3$  with Tateho SCW-1-S SiC whiskers had little effect on the fracture toughness. The toughness values were approximatively in the same range as monolithic  $\text{Al}_2\text{O}_3$ . On the other hand, the reinforcement of  $\text{Al}_2\text{O}_3$  with Silar SiC SC-9 whiskers contributed significantly to the improvement of the toughening behavior (see FIGURE 29).

## IV.D. FRACTOGRAPHY

### IV.D.1. Introduction

Since toughening was only observed in the composite reinforced with Silar SC-9 SiC whiskers, fractography was only performed on the composite to gain an understanding of possible toughening mechanisms.

### IV.D.2. Observation of Fracture Surfaces

#### IV.D.2.a. Room Temperature Fracture Surface

At room temperature, the fracture surface for the Silar SC-9 SiC whisker/ $\text{Al}_2\text{O}_3$  matrix composite showed a large amount of crack/microstructure interaction, with evidence of whisker pullout. FIGURE 30 allows the identification of empty hexagonal positions and protruding whiskers. The whiskers tended to fracture inside the matrix on a different plane than the primary crack plane. When the whisker failed and debonded from the matrix, it finally pulled out by a sliding process. FIGURE 31 shows with more detail a whisker which pulled out from the opposite fracture surface, clearly indicating a debonding and sliding mechanism. This toughening mechanism was responsible of the increase in the fracture toughness as the crack propagated. The fractographic results are in agreement with the results concerning the rising R-curves

calculated in the case of the Silar SC-9 SiC whisker/ $\text{Al}_2\text{O}_3$  matrix composites.

#### IV.D.2.b. High Temperature Fracture Surface

At high temperature, the observations are identical to those seen for the room temperature fracture surface relative to the interaction of the crack with the whiskers. FIGURE 32 shows hexagonal holes and protruding whiskers, which are characteristic of debonding, sliding, and pullout of the whiskers. It should be noted that it was impossible to obtain sharp pictures of the high



FIGURE 30: Micrograph Showing the Fracture Surface of Silar SC-9 SiC whisker/ $\text{Al}_2\text{O}_3$  Matrix Composite at Room Temperature.



FIGURE 31: Micrograph Showing the Toughening Mechanism Process in Silar SC-9 SiC Whisker/ $\text{Al}_2\text{O}_3$  Matrix Composite at Room Temperature.



FIGURE 32: Micrograph Showing the Fracture Surface of Silar SC-9 SiC Whisker/Al<sub>2</sub>O<sub>3</sub> Matrix Composite at High Temperature.

temperature fracture surfaces, due to a layer of glassy phase which covered the entire surface. This phase formed as the result of an oxidation process during the cooling stage of the mechanical testing cycle. After the mechanical testing was performed, the furnace was cooled down overnight. During this long period of time, the formation of a glassy phase occurred. FIGURE 33 shows evidence that the formation did not occur simultaneously with the crack propagation. It was possible to determine that the whisker first pulled out of the matrix and then the glassy phase formation started, at the end of the whisker where the activation energy of the reaction was higher. Similar to the room temperature results, the fractography is in agreement with the calculation of the rising R-curves for Silar SC-9 SiC whisker/ $\text{Al}_2\text{O}_3$  matrix composites at high temperature. The toughening mechanisms were identical at room and high temperature.



FIGURE 33: Micrograph Showing the Formation of a Glassy Phase at the End of a Silar SC-9 SiC Whisker at High Temperature.



## V. CONCLUSIONS

The numerical values of the fracture toughness described in the literature are in agreement with those measured in this investigation. The major result of this investigation was that the fracture toughness of  $\text{Al}_2\text{O}_3$  was significantly improved by reinforcing it with SiC whiskers. The crystallinity and the surface characteristics (cleanliness, defect free) of the SiC whiskers were found to be predominant in improving the mechanical properties of the composites. Additionally, testing at high temperature had a detrimental effect on fracture toughness.

For the Silar SC-9 SiC whisker/ $\text{Al}_2\text{O}_3$  matrix composite, it was possible to show rising R-curve behavior at room and high temperatures for the three whisker contents (15, 30, and 45 volume percent). All composites showed reinforcement with SiC whiskers and improved fracture toughness over that of monolithic  $\text{Al}_2\text{O}_3$ . The optimum composite, in regards to the fracture toughness and the rise of the R-curve, was the composite containing 30 volume percent SiC whiskers.

To support the R-curve calculation, scanning electron microscopy was used to visualize the type of toughening mechanisms that were present during the propagation of the crack through the Silar SC-9 SiC whisker/ $\text{Al}_2\text{O}_3$  matrix composites. The micrographs showed evidence of whisker debonding, whisker sliding, and whisker pullout as the major toughening mechanisms involved. The saw tooth behavior of the load-displacement curves also verified the operation of crack wake toughening mechanisms.

For the Tateho SCW-1-S SiC whisker/ $\text{Al}_2\text{O}_3$  matrix composite and monolithic  $\text{Al}_2\text{O}_3$ , flat R-curve behavior was observed at both temperatures. For these composites, the best values of the fracture toughness were obtained for whisker contents of 15 volume percent. There was evidence of a competing process between the reinforcement of the  $\text{Al}_2\text{O}_3$  matrix by whiskers and the presence of whiskers considered as defects in the matrix.

## ACKNOWLEDGMENTS

We would like to acknowledge the support of Garrett Auxiliary Power Division of Allied Signal Aerospace Company. With the competence and guidance of Ms. Irena Dumler, the electron microscopy work was carried out in the Center for Microanalysis of Materials, University of Illinois, which is supported by the U.S. Department of Energy under contract DE-AC 02-27ER 01198.

## REFERENCES

- 1 P. F. Becher and G. C. Wei, "Toughening Behavior in SiC-Whisker-Reinforced Alumina," J. Am. Ceram. Soc., **67** [12] C267-C269 (1984)
- 2 M. G. Jenkins, A. S. Kobayashi, K. W. White, and R. C. Bradt, "Crack Initiation and Arrest in a SiC Whisker/ $\text{Al}_2\text{O}_3$  Matrix Composite," J. Am. Ceram. Soc., **70** [6] 393-95 (1987)
- 3 J. Homeny and W. L. Vaughn, "Whisker-Reinforced Ceramic Matrix Composites," MRS Bulletin, Oct. 1/Nov. 15, 66-71 (1987)
- 4 W. D. Kingery, H. K. Browen and D. R. Uhlmann. *Introduction to Ceramics*. John Wiley & Sons, New York, New York (1976)
- 5 R. W. Rice, "A Material Opportunity : Ceramic Composites," Chem. Tech. **4** 230-39 (1983)
- 6 L. J. Schioler and J. J. Stiglich, Jr., "Ceramic Matrix Composites : A Literature Review," Am. Ceram. Soc. Bull., **65** [2] 289-92 (1986)
- 7 E. R. Billman, P. K. Mehrotra, A. F. Shuster, and C. W. Beeghly, "Machining with  $\text{Al}_2\text{O}_3$ -SiC-Whisker Cutting Tools," Am. Ceram. Soc. Bull., **67** [6] 1016-19 (1988)
- 8 W. H. Gitzen, " *Alumina as a Ceramic Material* ," Special Publication, The American Ceramic Society, Inc., Columbus, Ohio (1970)
- 9 H. J. Sanders, "High-tech Ceramics," Chemical & Engineering News, Vol. 62, July 9, 26-40 (1984)

- <sup>10</sup> S. R. Nutt, "Defects in Silicon Carbide Whiskers," J. Am. Ceram. Soc., **67** [6] 428-31 (1984)
- <sup>11</sup> J. Lee and I. B. Cutler, "Formation of Silicon Carbide from Rice Hulls," Am. Ceram. Soc. Bull., **54** [2] 195-98 (1975)
- <sup>12</sup> V. K. Sarin and M. Ruhle, "Microstructural Studies of Ceramic-Matrix Composites," Composites, Volume 18, **2** [4] 129-133 (1987)
- <sup>13</sup> K. S. Mazdiasni, R. West, and L. D. David, "Characterization of Organosilicon-Infiltrated Porous Reaction-Sintered  $\text{Si}_3\text{N}_4$ ," J. Am. Ceram. Soc., **61** [11-12] 504-08 (1978)
- <sup>14</sup> K. S. Mazdiasni and A. Zangvil, "Effect of Impurities on SiC Whisker Morphology," J. Am. Ceram. Soc., **68** [6] C142-C144 (1985)
- <sup>15</sup> J. J. Shyne and J. V. Milewski, "Method of Growing Silicon Carbide Whiskers," US Patent 3 622 272, November (1971)
- <sup>16</sup> J. J. Petrovic, J. V. Milewski, D. L. Rohr, and F. D. Gac, "Tensile Mechanical Properties of SiC Whiskers," J. Mater. Sci. **20** 1167-77 (1985)
- <sup>17</sup> P. D. Shelek, G. F. Hurley, D. E. Christiansen, W. J. Parkinson, and J. D. Katz, "Effect of Process Parameters on the Growth of VLS SiC Whiskers," NASA Conference Publication 2482 (1986)
- <sup>18</sup> R. Dagani, "Ceramic Composites Emerging as Advanced Structural Materials," Chem. & Eng. News [2] 7-12 (1985)
- <sup>19</sup> E. Carlström and F. F. Lange, "Mixing of Flocced Suspensions," J. Amer. Ceram. Soc., **67** [8] C169-C170 (1986)

- <sup>20</sup> R. Lundberg, B. Nyberg, K. Willander, M. Persson, and R. Carlsson, "Processing of Whisker-Reinforced Ceramics," *Composites*, Volume 18, 2 [4] 125-127 (1987)
- <sup>21</sup> G. C. Wei and P. F. Becher, "Development of SiC-Whisker-Reinforced Ceramics," *Am. Ceram. Soc. Bull.*, 64 [2] 298-304 (1985)
- <sup>22</sup> T. N. Tiegs and P. F. Becher, "Sintered Al<sub>2</sub>O<sub>3</sub>-SiC-Whisker Composites," *Am. Ceram. Soc. Bull.*, 66 [2] 339-42 (1987)
- <sup>23</sup> J. R. Porter, F. F. Lange, and A. H. Chokshi, "Processing and Creep Performance of SiC-Whisker-Reinforced Al<sub>2</sub>O<sub>3</sub>," *Am. Ceram. Soc. Bull.*, 66 [2] 343-47 (1987)
- <sup>24</sup> D. B. Marshall and J. E. Ritter, "Reliability of Advanced Structural Ceramics and Ceramic Matrix Composites - A Review," *Am. Ceram. Soc. Bull.*, 66 [2] 309-17 (1987)
- <sup>25</sup> D. C. Larsen, K. L. Reifsnider, "Mechanical Evaluation of Refractory Fiber Composites," Unpublished Manuscript.
- <sup>26</sup> G. C. Sih, "Stress-Intensity Factor Solutions and Formulas for Reference," *Handbook of Stress-Intensity Factors*. Institute of Fracture and Solid Mechanics, Lehigh University, Bethlehem, Pennsylvania (1973)
- <sup>27</sup> A. G. Evans, "The New Generation of High Toughness Ceramics," *Ceramic Microstructure '86 : The Role of Interfaces*. Materials Science Research, Volume 21, Edited by J. A. Pask and A. G. Evans, Plenum Press, New York, New York 775-94 (1987)
- <sup>28</sup> K. T. Faber and A. G. Evans, "Crack Deflection Processes-I. Theory," *Acta. Metall.*, 31 [4] 573-76 (1983)

- 29 K. T. Faber and A. G. Evans, "Crack Deflection Processes-II. Experiments," *Acta. Metall.*, **31** [4] 577-84 (1983)
- 30 R. Warren and V. K. Sarin, "Fracture of Whisker Reinforced Ceramics," Unpublished Manuscript.
- 31 D. B. Marshall, "An Indentation Method for Measuring Matrix-Fiber Frictional Stresses in Ceramic Composites," *J. Am. Ceram. Soc.*, **67** [12] C259-C260 (1984)
- 32 J. J. Mecholski, "Evaluation of Mechanical Property Testing Methods for Ceramic Matrix Composites," *Am. Ceram. Soc. Bull.*, **65** [2] 315-22 (1986)
- 33 P. F. Becher, C.-H. Hsueh, P. Angelini, and T. N. Tiegs, "Toughening Behavior in Whisker-Reinforced Ceramic Matrix Composites," *J. Am. Ceram. Soc.*, **71** [12] 1050-61 (1988)
- 34 M. F. Kanninen and C. H. Popelar, *Advanced Fracture Mechanics*. Oxford University Press, New York, New York, 64-5 (1985)
- 35 D. Munz, R. T. Bubsey, and J. E. Srawley, "Compliance and Stress Intensity Coefficients for Short Bar Specimens with Chevron Notches," *Int. Journ. of Fracture*, **16** 359-374 (1980)
- 36 D. Lewis III, "Whisker-Reinforcement Ceramics," Unpublished Manuscript
- 37 R. F. Pabst, Ph. D. Thesis, Stuttgart (1972)
- 38 F. E. Buresch, "A Model for the Fracture Strength of Ceramics and its Influence on Critical Fracture Stresses," *Science of Ceramics, Vol. 7*. Published by Société Française de Céramique, Brevatome, Paris 383-91 (1973)

- 39 M. Sakai and R. C. Bradt, "The Crack Growth Resistance Curve of Non-Phase-Transforming Ceramics," *Nippon-Seramikkusu-Kyokai-Gakujutsu-Ronbunshi*, **96** [8] 801-09 (1988)
- 40 P. L. Swanson, C. J. Fairbanks, B. R. Lawn, Y. Mai and B. J. Hockey, "Crack Interface Grain Bridging as a Fracture Resistance Mechanism in Ceramics: I, Experimental Study on Alumina," *J. Am. Ceram. Soc.*, **70** [4] pp. 279-89 (1987)
- 41 J. C. Newman, Jr., "A Review of Chevron-Notched Fracture Specimens," *Chevron-Notched Specimens: Testing and Stress Analysis, ASTM STP 855*. Edited by J. H. Underwood, S. W. Freiman, and F. I. Baratta, Eds., American Society for Testing and Materials, Philadelphia, Pennsylvania 5-31 (1984)
- 42 M. G. Jenkins, A. S. Kobayashi, K. W. White, and R. C. Bradt, "Elevated Temperature Fracture Resistance of a SiC Whisker Reinforced/Polycrystalline  $\text{Al}_2\text{O}_3$  Matrix Composite," *Engineering Fracture Mechanics*, **30** [4] 505-515 (1988)
- 43 B. Gross and J. E. Srawley, "Stress Intensity Factors by Boundary Collocation for Single-Edge-Notch Specimens Subject to Splitting Forces," *NASA JN D-3295* (1966)
- 44 D. Munz, R. T. Bubsey, and J. L. Shannon, Jr., "Fracture Toughness Determination of  $\text{Al}_2\text{O}_3$  Using Four-Point-Bend Specimens with Straight-Through and Chevron Notches," *J. Amer. Ceram. Soc.* **63** [5-6] 300-305 (1980)
- 45 A. H. Cottrell, *The Mechanical Properties of Matter*, R. E. Krieger Publishing Company, Huntington, New York, 124-130 (1981)



- 46 M. Sakai and K. Yamasaki, "Numerical Fracture Analysis of Chevron-Notched Specimens: I, Shear Correction Factor,  $k$ ," J. Amer. Cer. Soc., **66** [5] 371-75 (1983)
- 47 P. F. Becher, T. N. Tiegs, J. C. Ogle, and W. H. Warnick, "Toughening of Ceramics by Whisker Reinforcement," *Fracture Mechanics of Ceramics, Vol.7*. Edited by R. C. Bradt, A. G. Evans, D. P. H. Hasselman, and F. F. Lange. Plenum Press, New York, 61-73 (1986)
- 48 A. H. Cholski and J. R. Porter, "Creep Deformation of an Alumina Matrix Composite Reinforced with Silicon Carbide Whiskers," J. Am. Ceram. Soc., **67** [6] C144-C145 (1985)
- 49 T. N. Tiegs and P. F. Becher, "Thermal Shock Behavior of an Alumina-SiC Whisker Composites," J. Am. Ceram. Soc., **70** [5] C109-C111 (1987)
- 50 D. B. Marshall, "Interfaces in Ceramic Fiber Composites," *Ceramic Microstructure '86 : The Role of Interfaces*. Materials Science Research, Volume 21, Edited by J. A. Pask and A. G. Evans, Plenum Press, New York, New York 859-68 (1987)
- 51 T. N. Tiegs, P. F. Becher, and L. A. Harris, "Interfaces in Alumina-SiC Whisker Composites," *Ceramic Microstructure '86 : The Role of Interfaces*. Materials Science Research, Volume 21, Edited by J. A. Pask and A. G. Evans, Plenum Press, New York, New York 911-17 (1987)
- 52 J. Selsing, "Internal Stresses in Ceramics," J. Am. Ceram. Soc., **44** [8] 419 (1961)
- 53 E. Schreiber, O.L. Anderson, and N. Soga, *Elastic Constants and*

*Their Measurements.* McGraw Hill, New York, New York  
(1974)

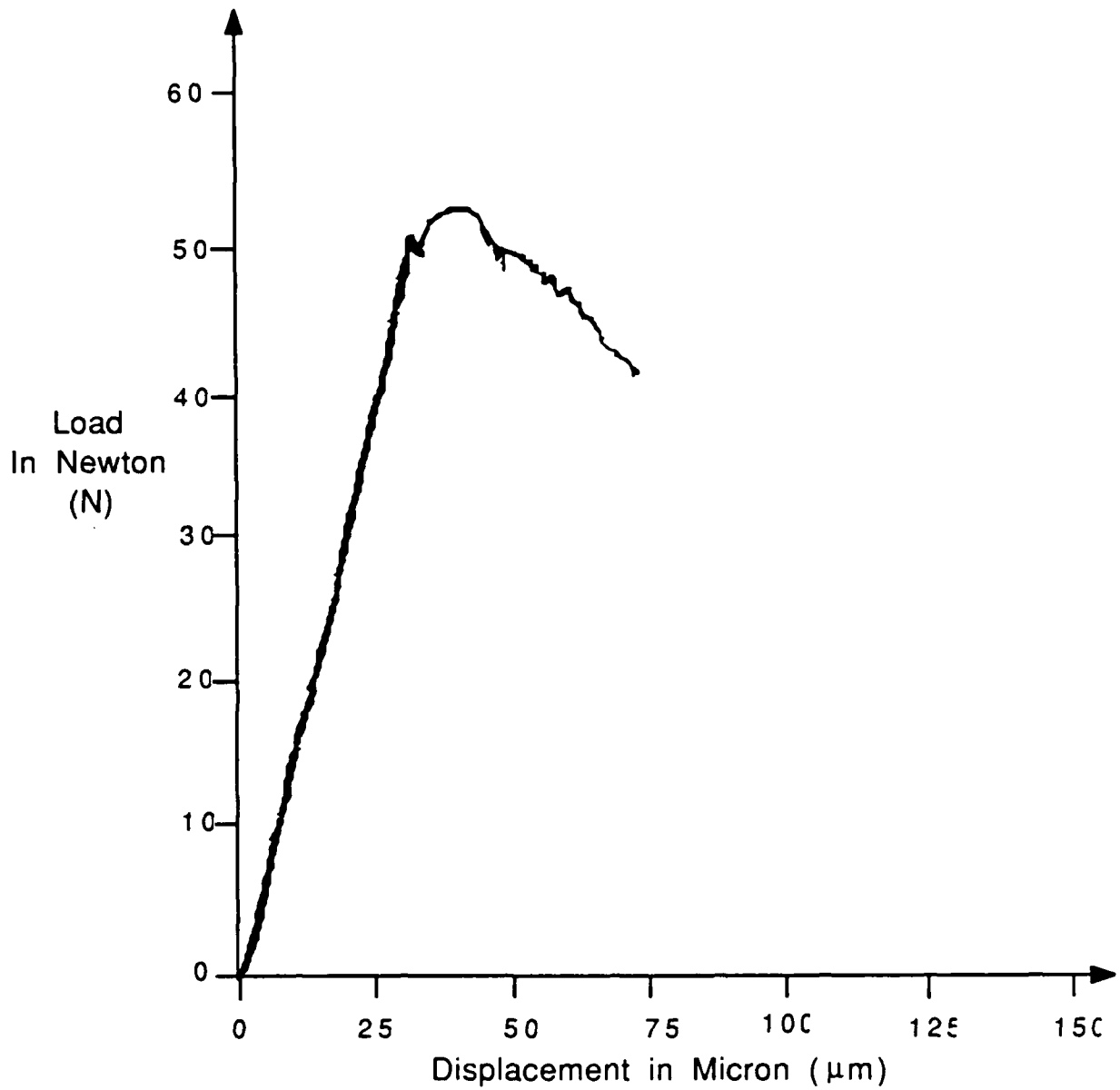


FIGURE A1: Load-Displacement Curve for 15 Vol.% Tateho SiC Whisker/Aluminum Oxide Matrix Composite at Room Temperature with an Angle of 69.44 Degree at the Base of the Chevron Notch.

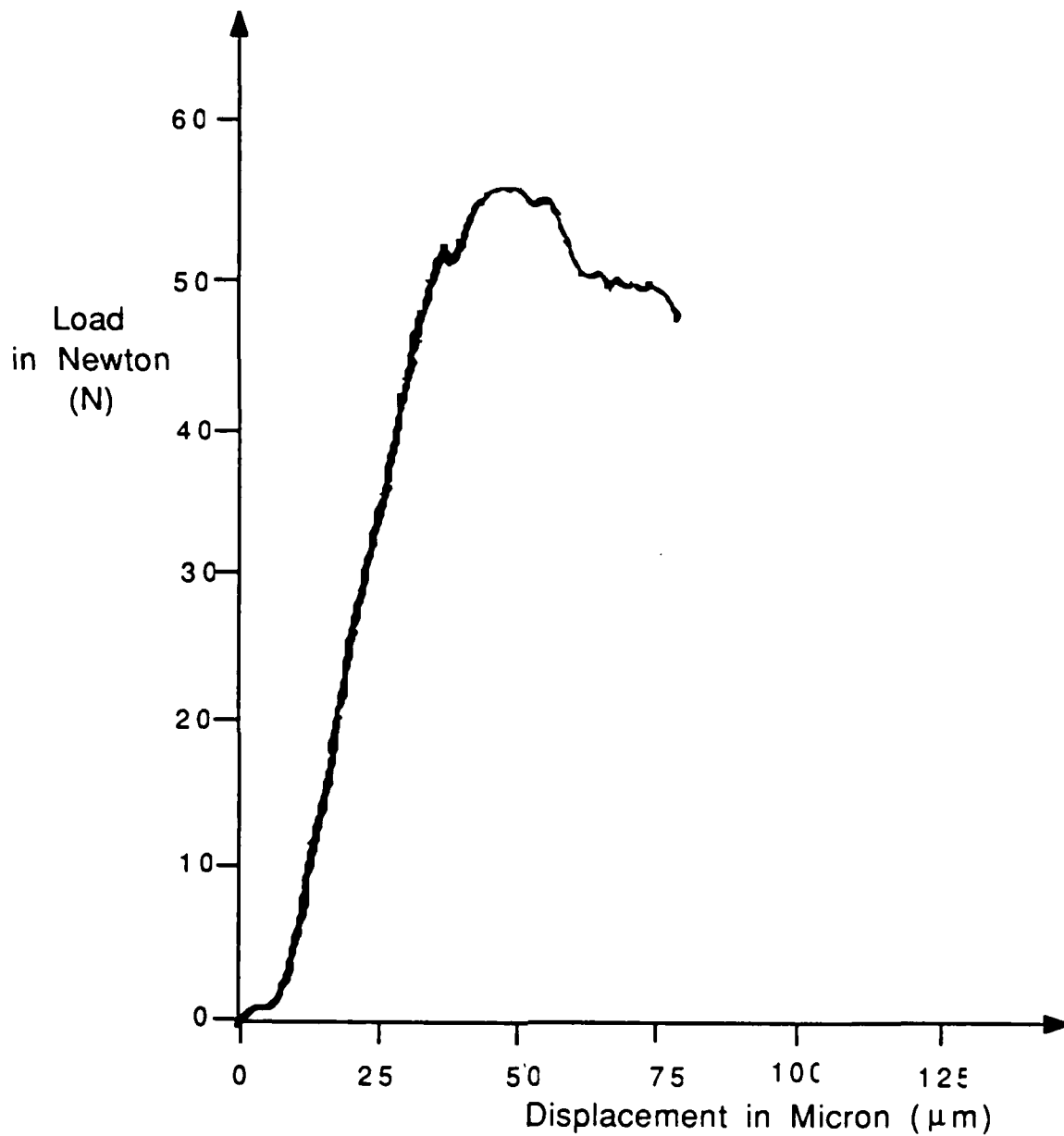


FIGURE A2: Load-Displacement Curve for 30 Vol.% Tateho SiC Whisker/Aluminum Oxide Matrix Composite at Room Temperature with an Angle of 69.44 Degree at the Base of The Chevron Notch.

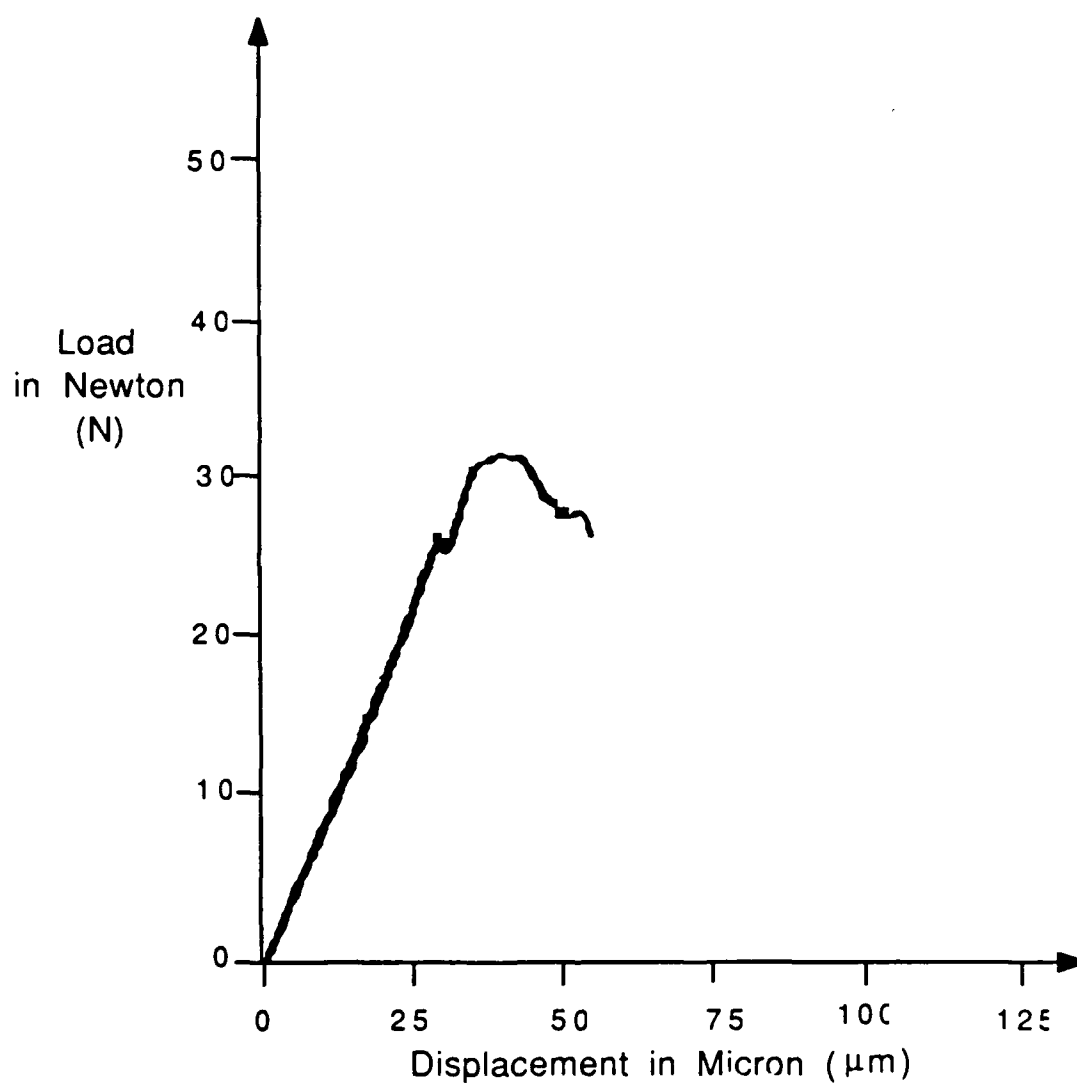


FIGURE A3: Load-Displacement Curve for 45 Vol.% Tateho SiC Whisker/Aluminum Oxide Matrix Composite at Room Temperature with an Angle of 69.44 Degree at the Base of the Chevron Notch.

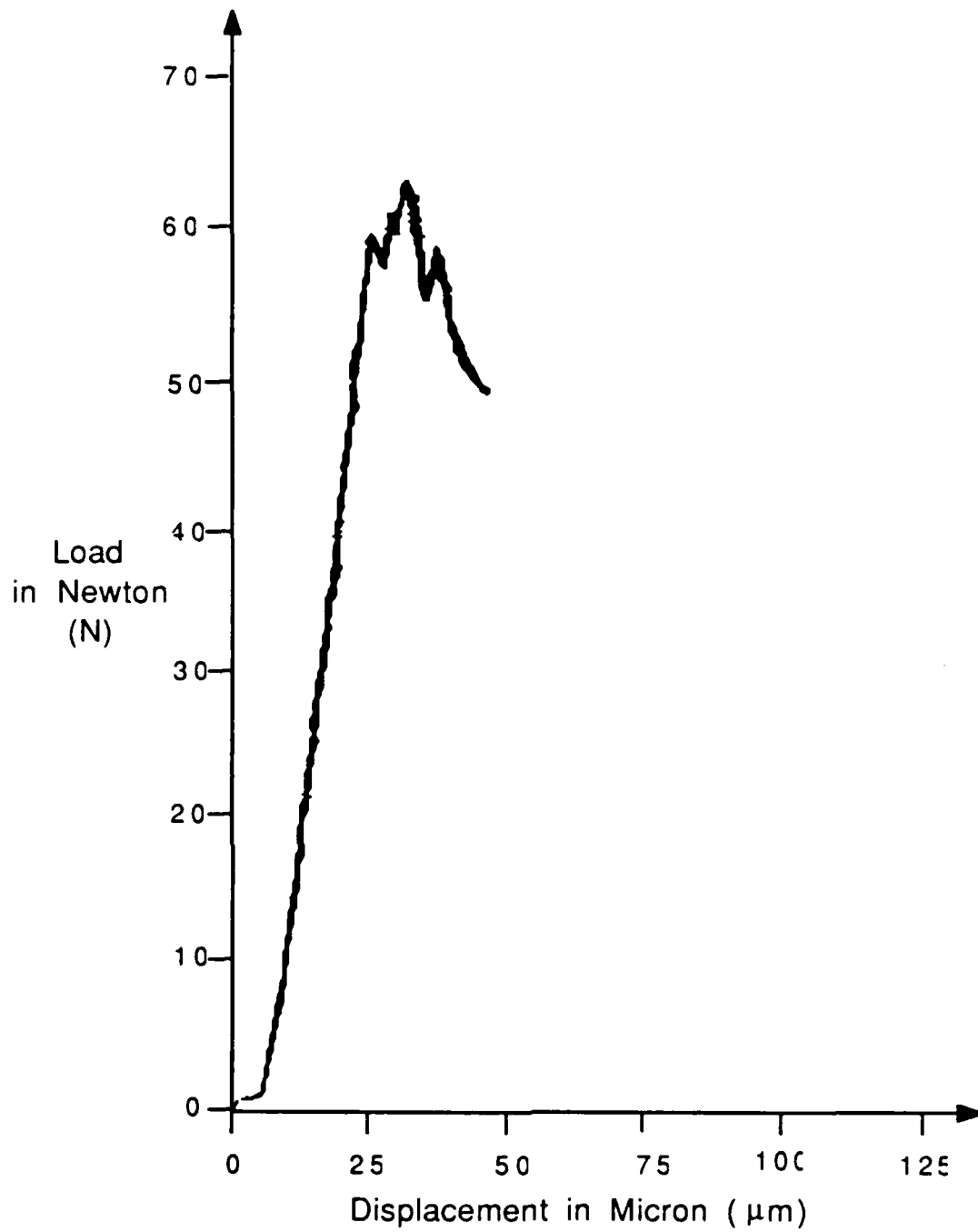


FIGURE A4: Load-Displacement Curve for 15 Vol.% Star SiC Whisker/Aluminum Oxide Matrix Composite at Room Temperature with an Angle of 69.44 Degree at the Base of the Chevron Notch.

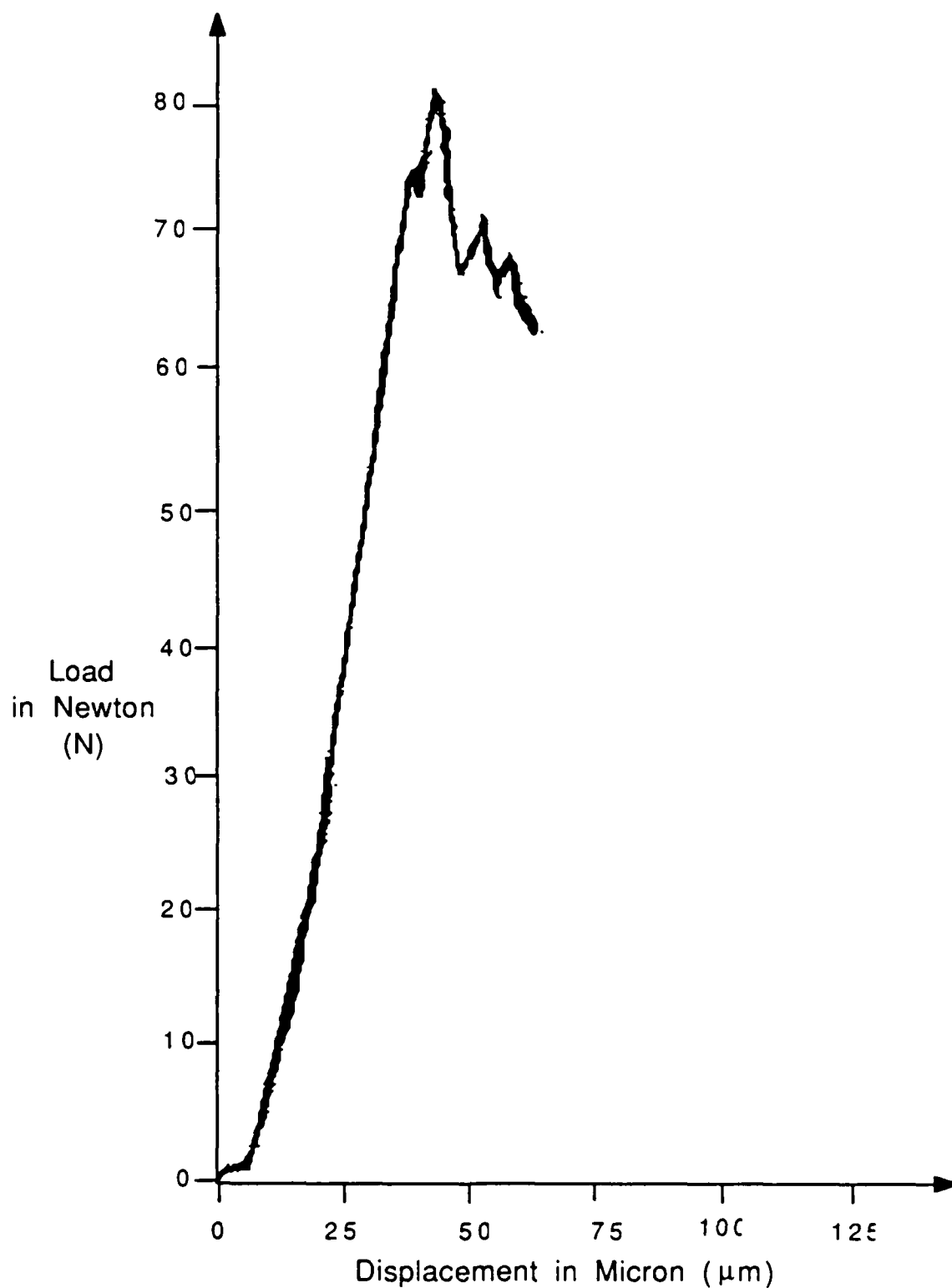


FIGURE A5: Load-Displacement Curve for 30 Vol.% Star SiC Whisker/Aluminum Oxide Matrix Composite at Room Temperature with an Angle of 69.44 Degree at the Base of the Chevron Notch.

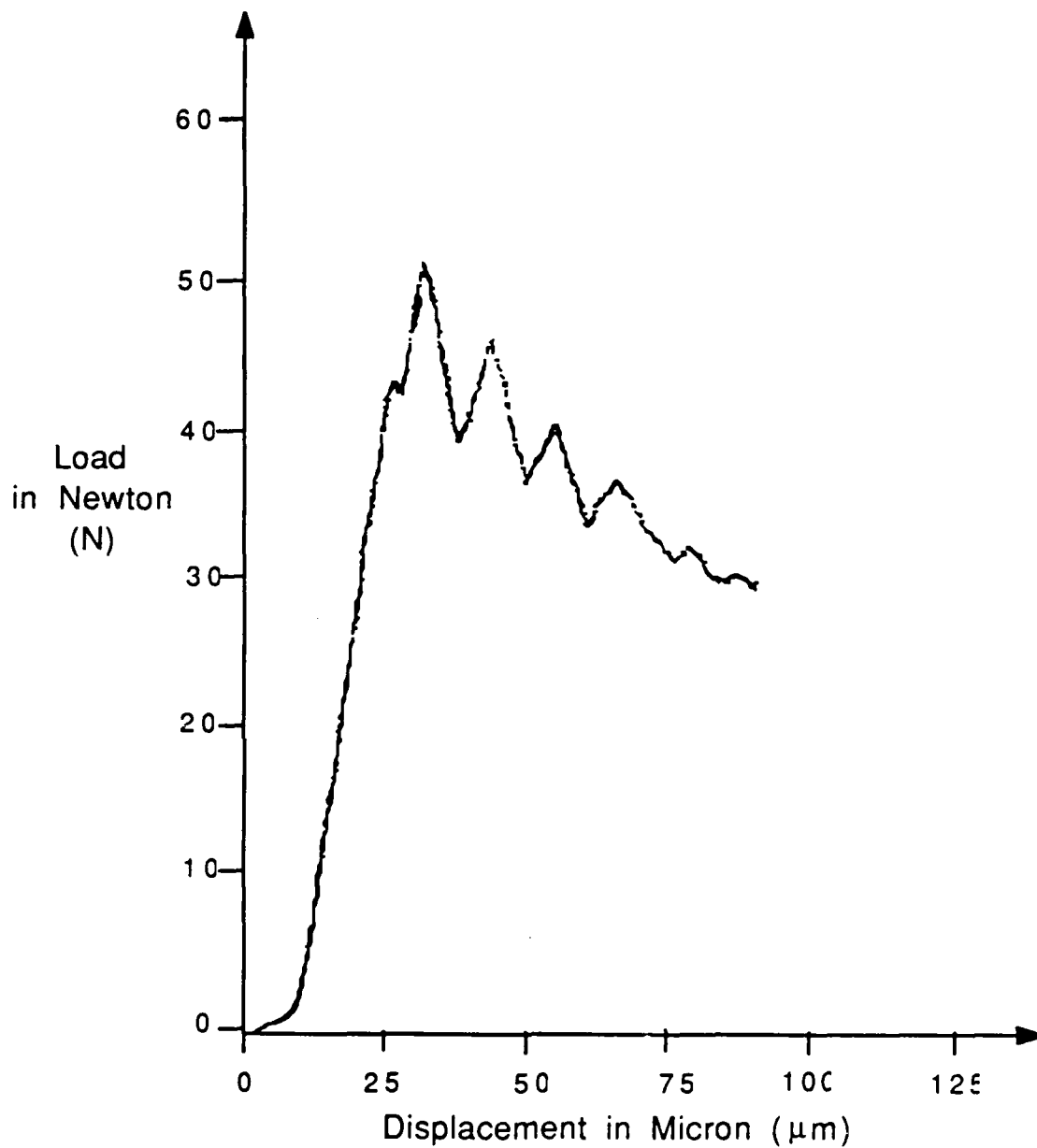


FIGURE A6: Load-Displacement Curve for 45 Vol.% SiC Whisker/Aluminum Oxide Matrix Composite at Room Temperature with an Angle of 69.44 Degree at the Base of the Chevron Notch.



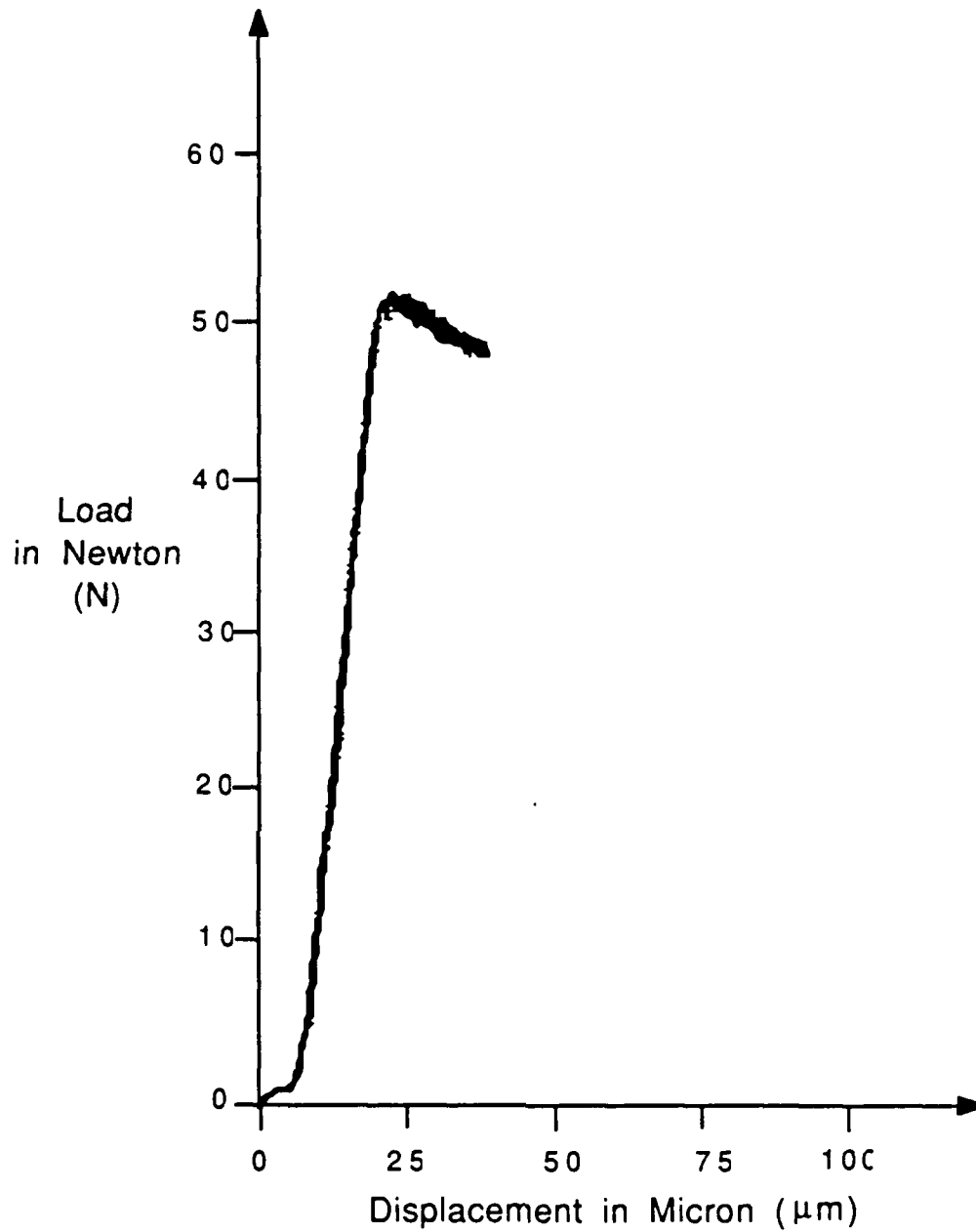


FIGURE A7: Load-Displacement Curve for Monolithic Aluminum Oxide at Room Temperature with an Angle of 69.44 Degree at the Base of The Chevron Notch.

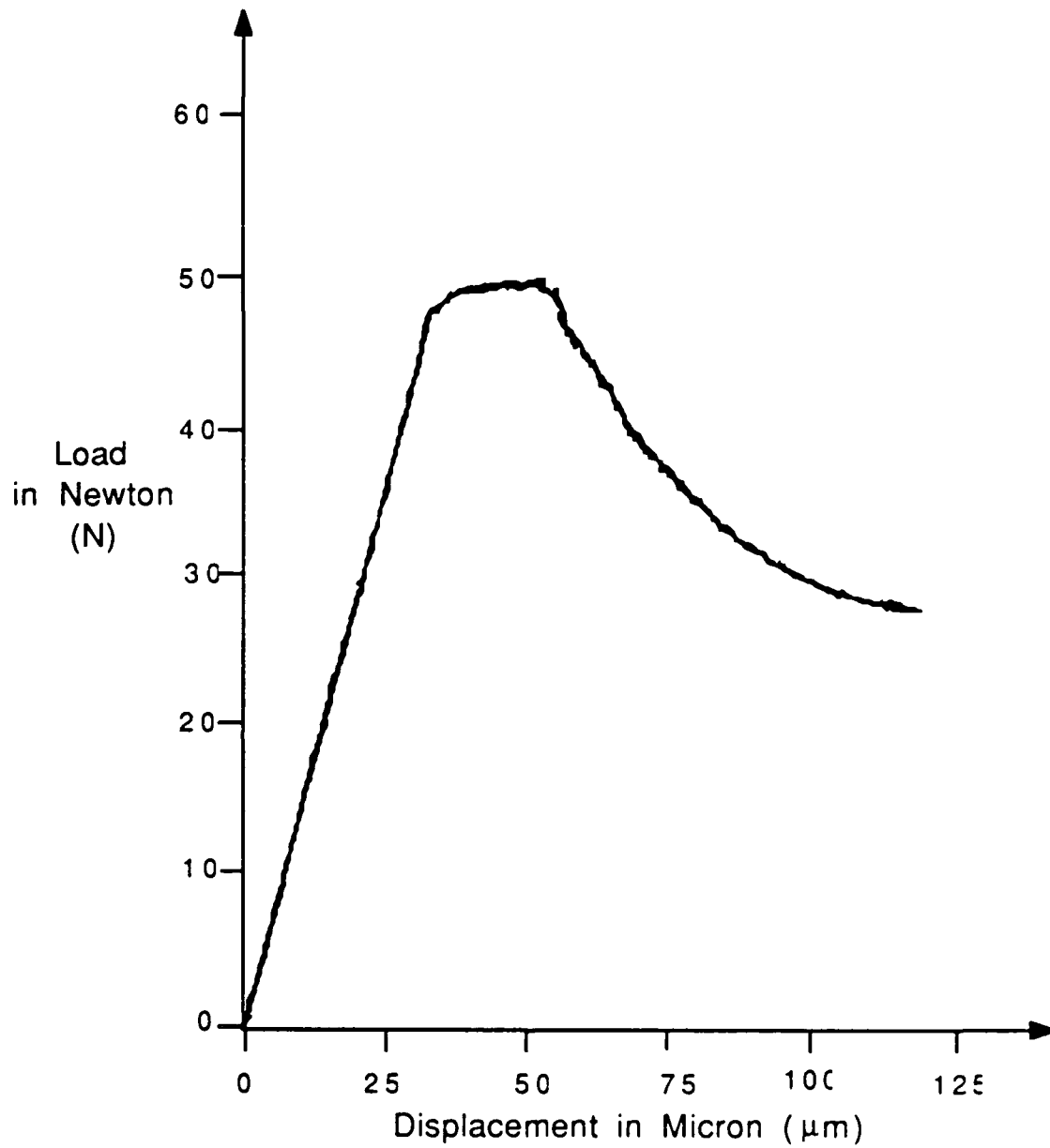


FIGURE A8: Load-Displacement Curve for 15 Vol.% Tateho SiC Whisker/Aluminum Oxide Matrix Composite at Room Temperature with an Angle of 45 Degree at the Base of the Chevron Notch.

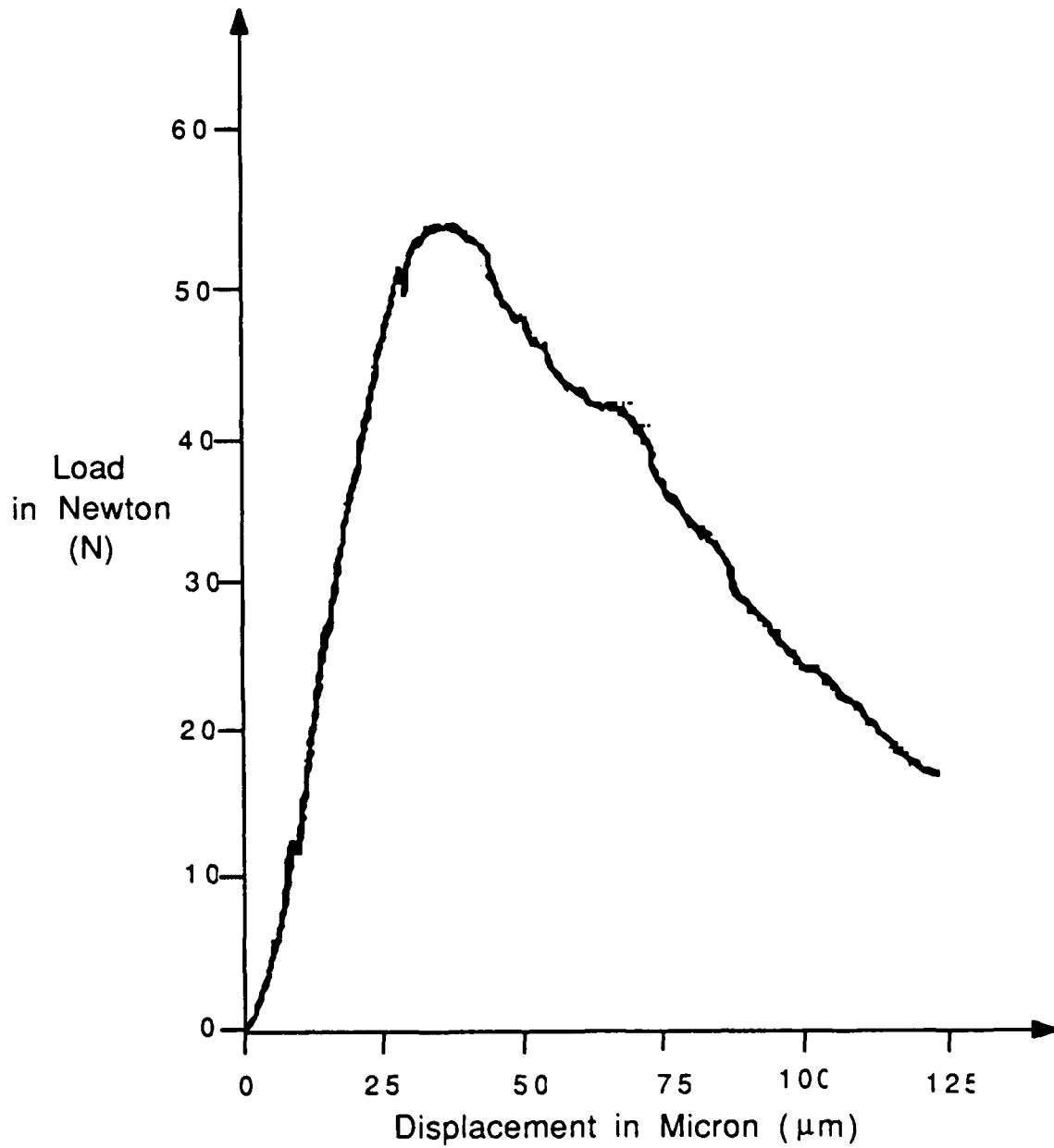


FIGURE A9: Load-Displacement Curve for 30 Vol.% Tateho SiC Whisker/Aluminum Oxide Matrix Composite at Room Temperature with an Angle of 45 Degree at the Base of the Chevron Notch.

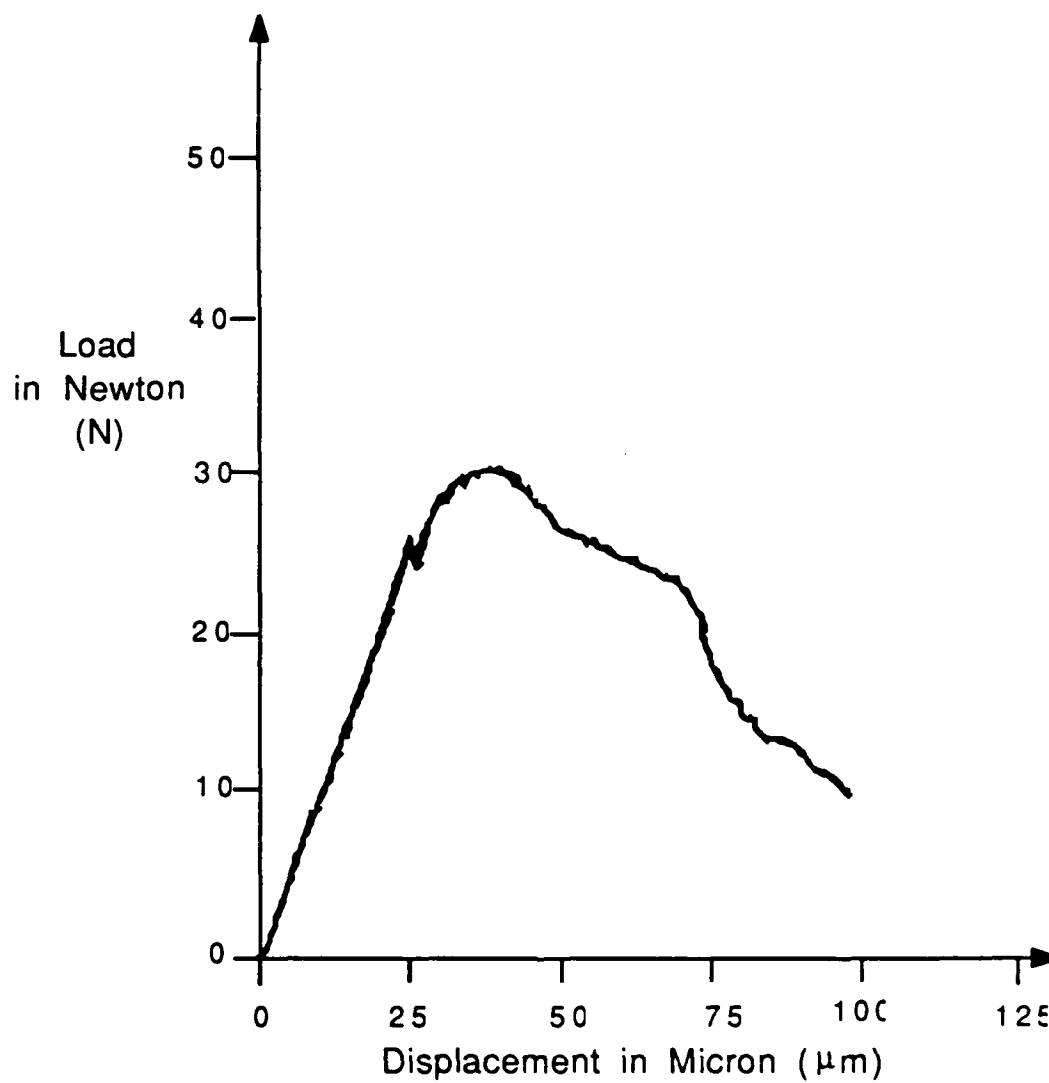


FIGURE A10: Load-Displacement Curve for 45 Vol.% Tateho SiC Whisker/Aluminum Oxide Matrix Composite at Room Temperature with an Angle of 45 Degree at the Base of the Chevron Notch.

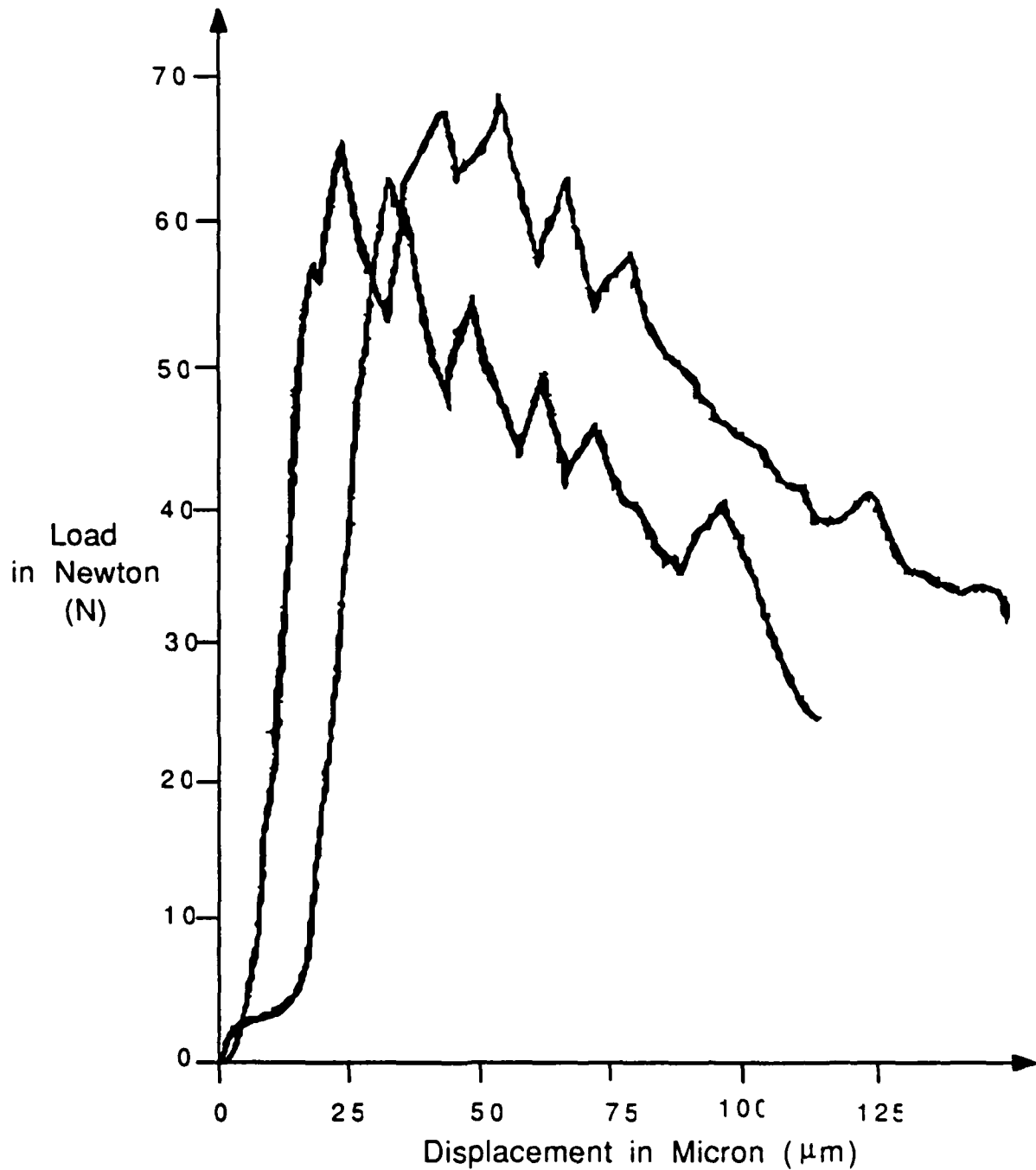


FIGURE A11: Load-Displacement Curves for 15 Vol.% Silica/SiC Whisker/Aluminum Oxide Matrix Composite at Room Temperature with an Angle of 45 Degree at the Base of the Chevron Notch.

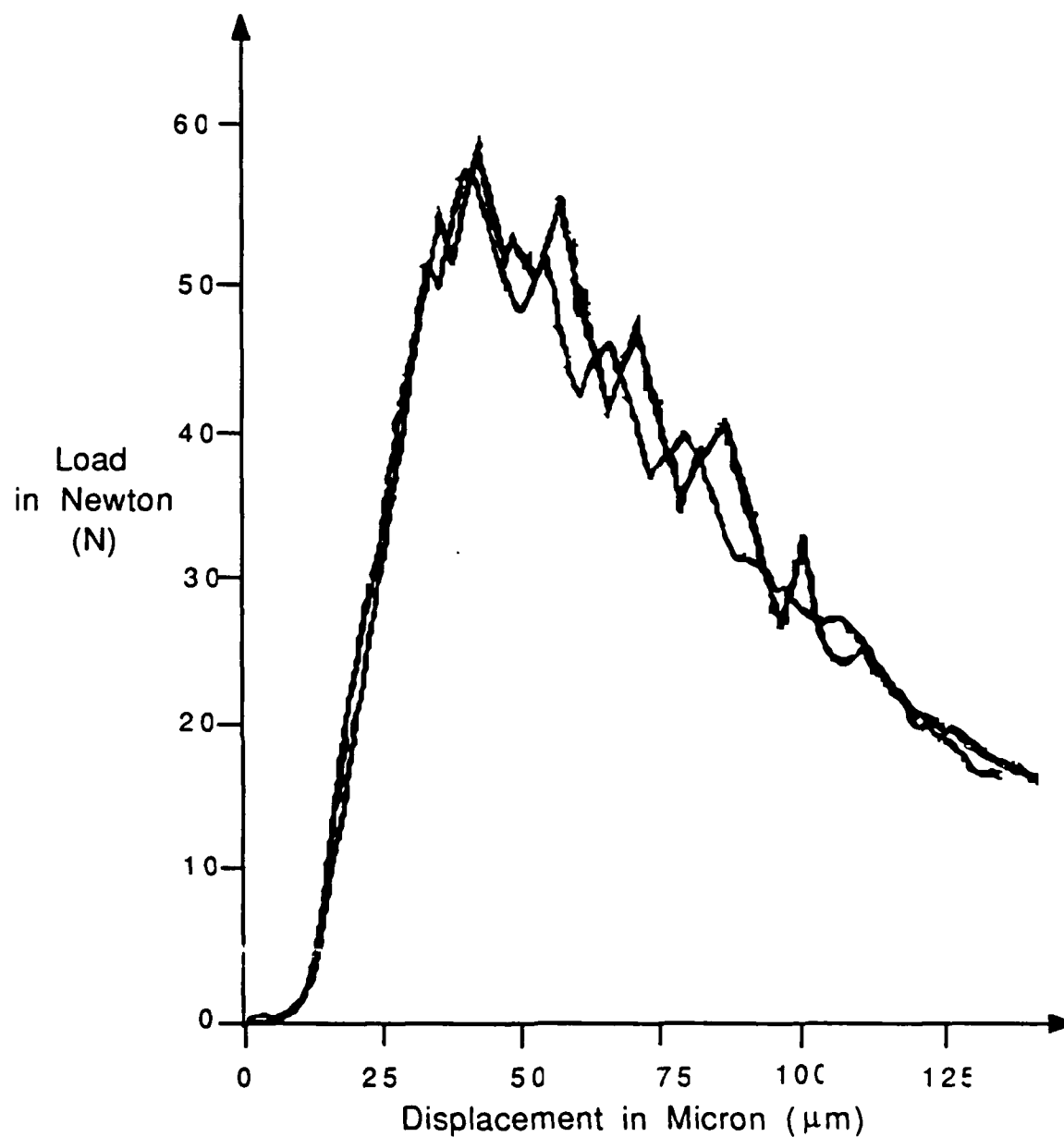


FIGURE A12: Load-Displacement Curves for 30 Vol.% Silar SiC Whisker/Aluminum Oxide Matrix Composite at Room Temperature with an Angle of 45 Degree at the Base of the Chevron Notch.

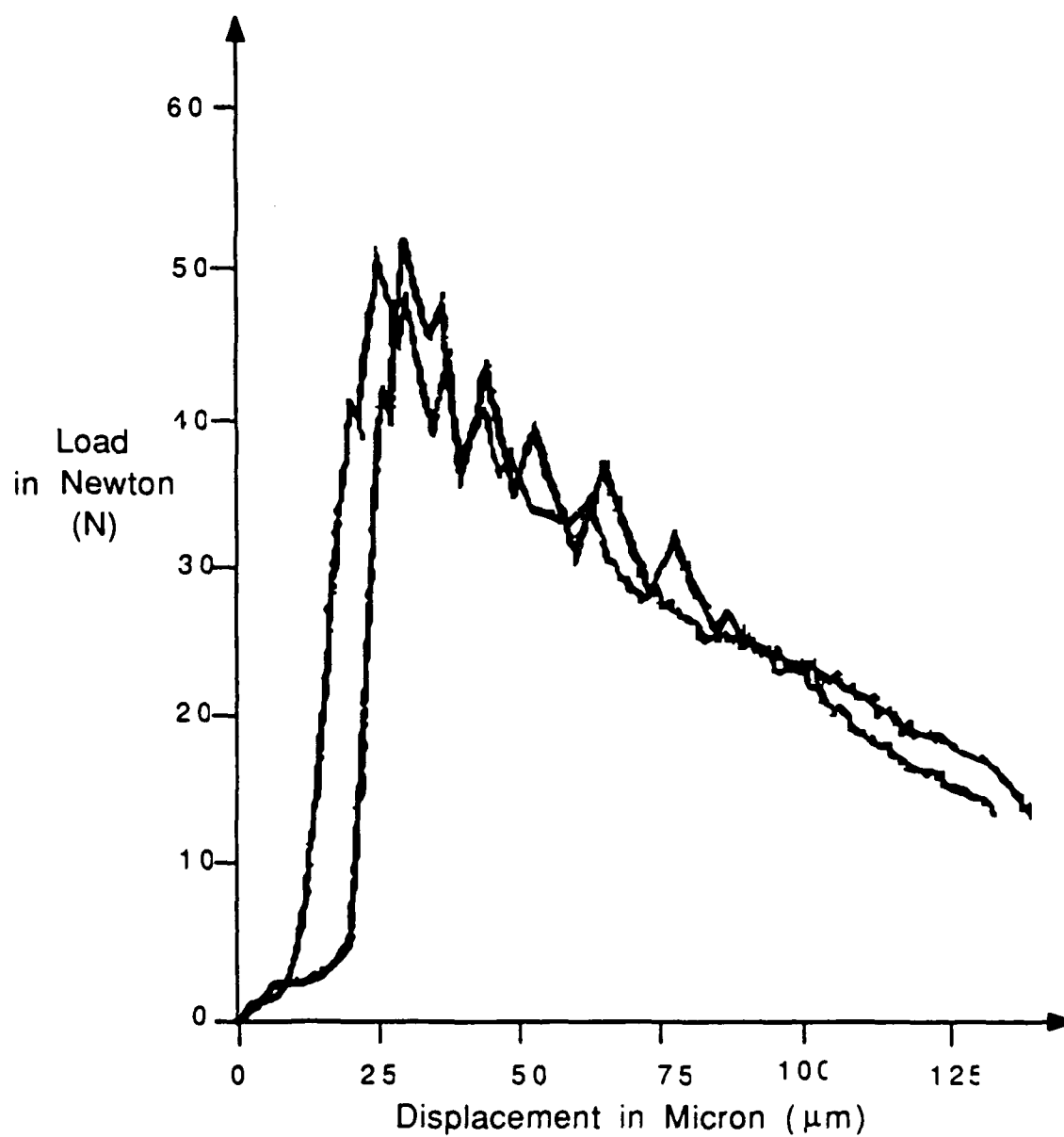


FIGURE A13: Load-Displacement Curves for 45 Vol.% Silar SiC Whisker/Aluminum Oxide Matrix Composite at Room Temperature with an Angle of 45 Degree at the Base of the Chevron Notch.

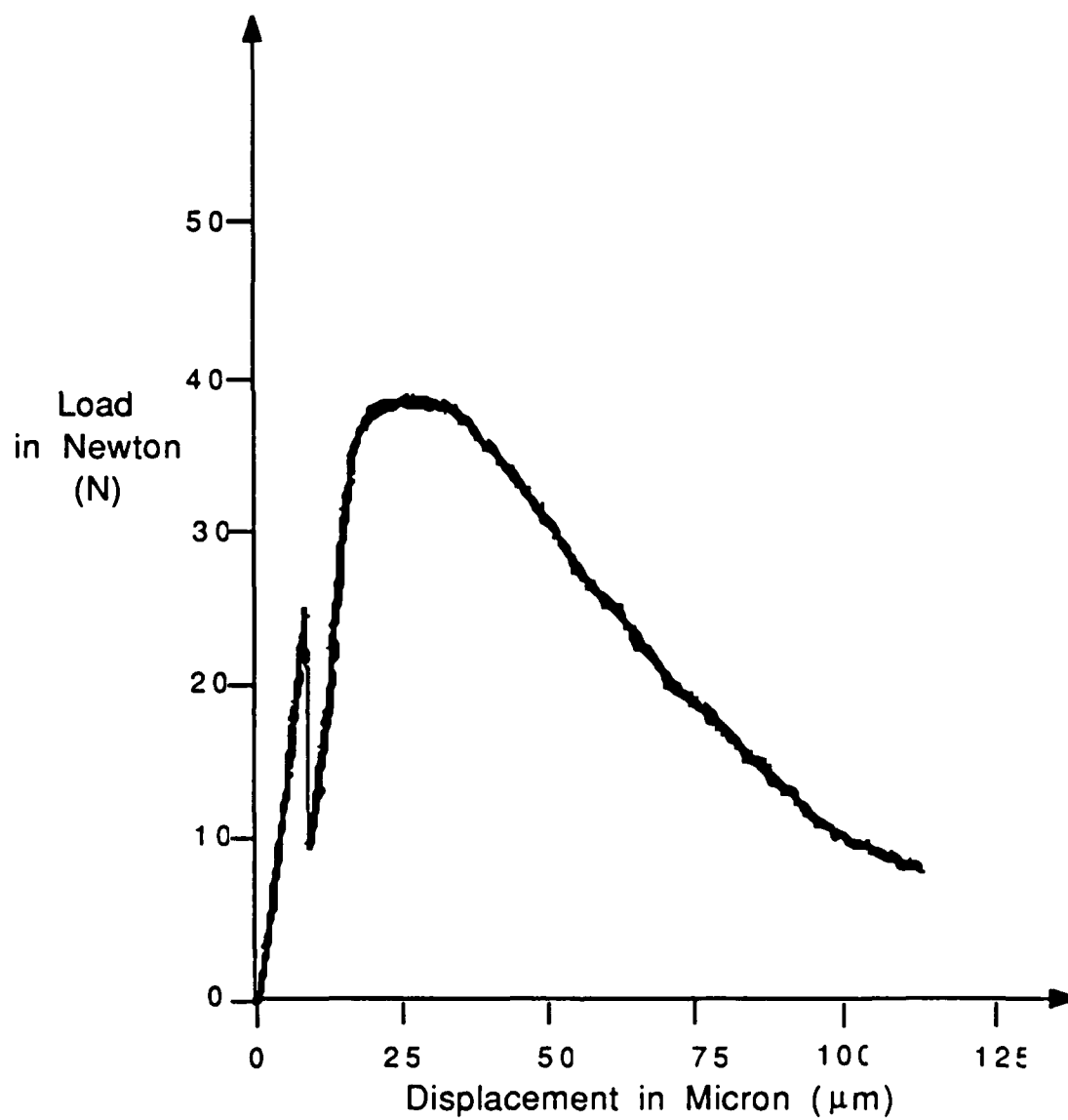


FIGURE A14: Load-Displacement Curve for Monolithic Aluminum Oxide at Room Temperature with an Angle of 45 Degree at the Base of the Chevron Notch.



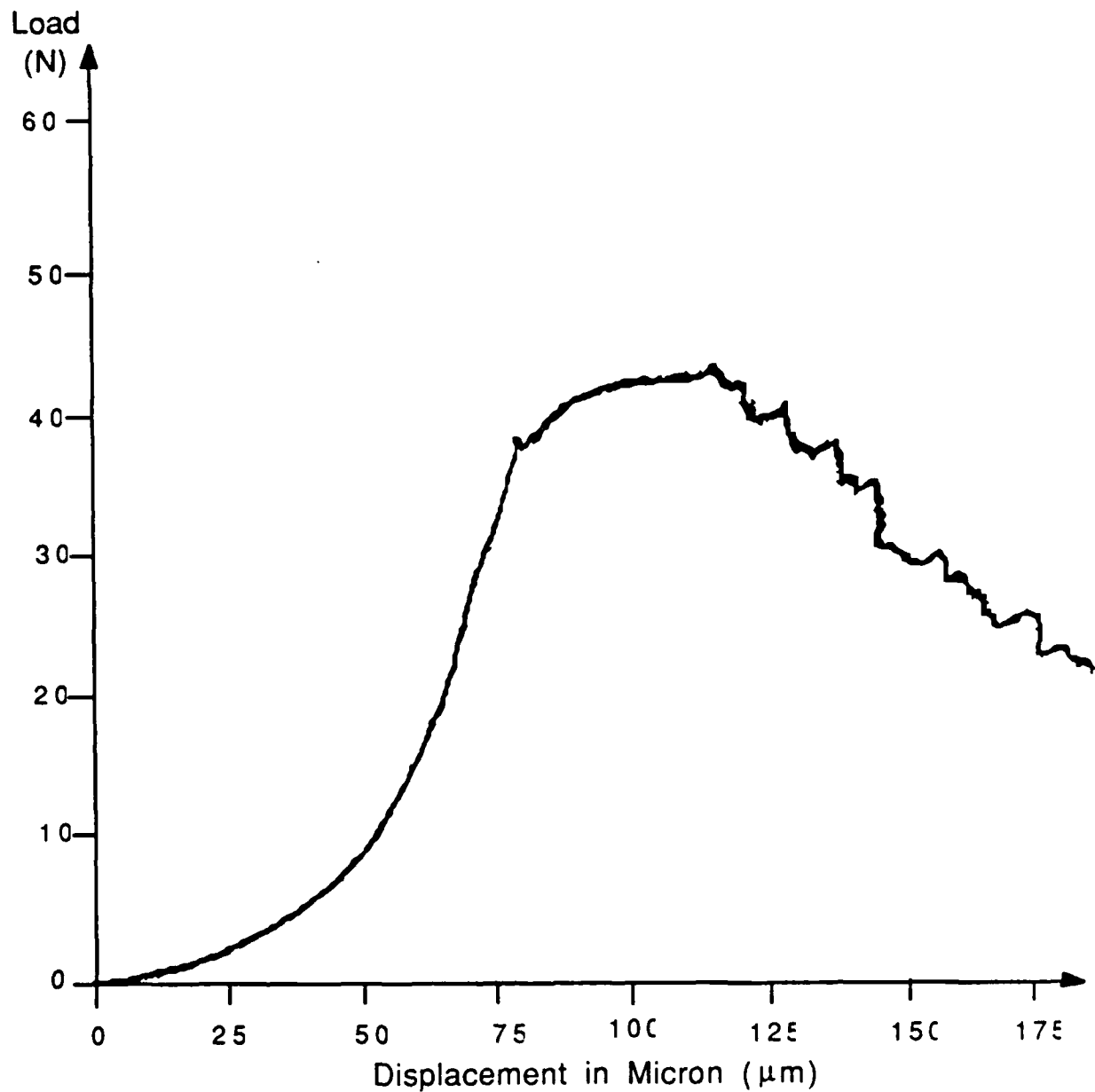


FIGURE A15: Load-Displacement Curve for 15 Vol.% Tateho SiC Whisker/Aluminum Oxide Matrix Composite at High Temperature (1000 Degree Celsius) with an Angle of 45 Degree at the Base of the Chevron Notch.

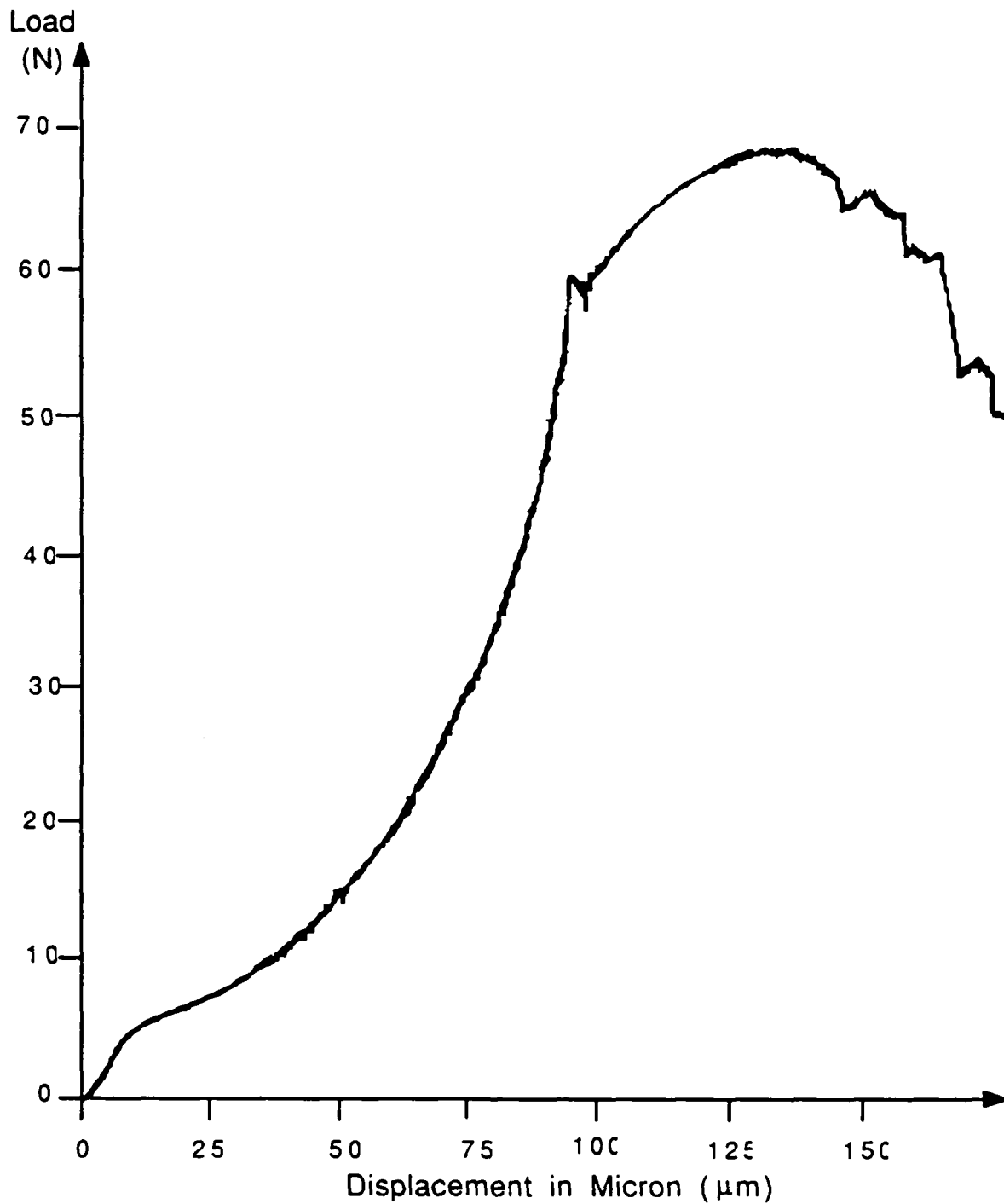


FIGURE A16: Load-Displacement Curve for 30 Vol.% Tateho SiC Whisker/Aluminum Oxide Matrix Composite at High Temperature (1000 Degree Celsius) with an Angle of 45 Degree at the Base of the Chevron Notch.

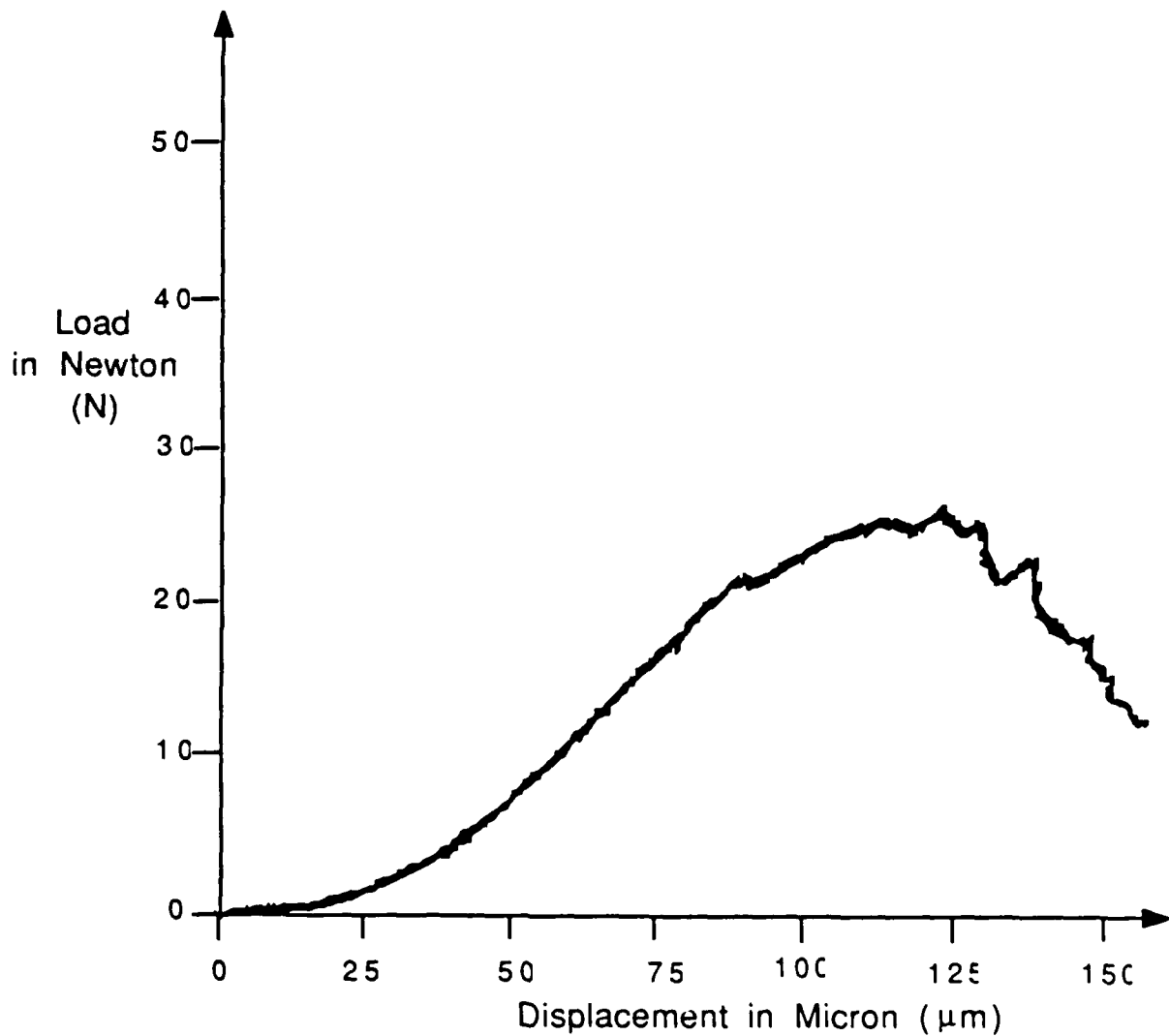


FIGURE A17: Load-Displacement Curve for 45 Vol.% Tateho SiC Whisker/Aluminum Oxide Matrix Composite at High Temperature (1000 Degree Celsius) with an Angle of 45 Degree at the Base of the Chevron Notch.

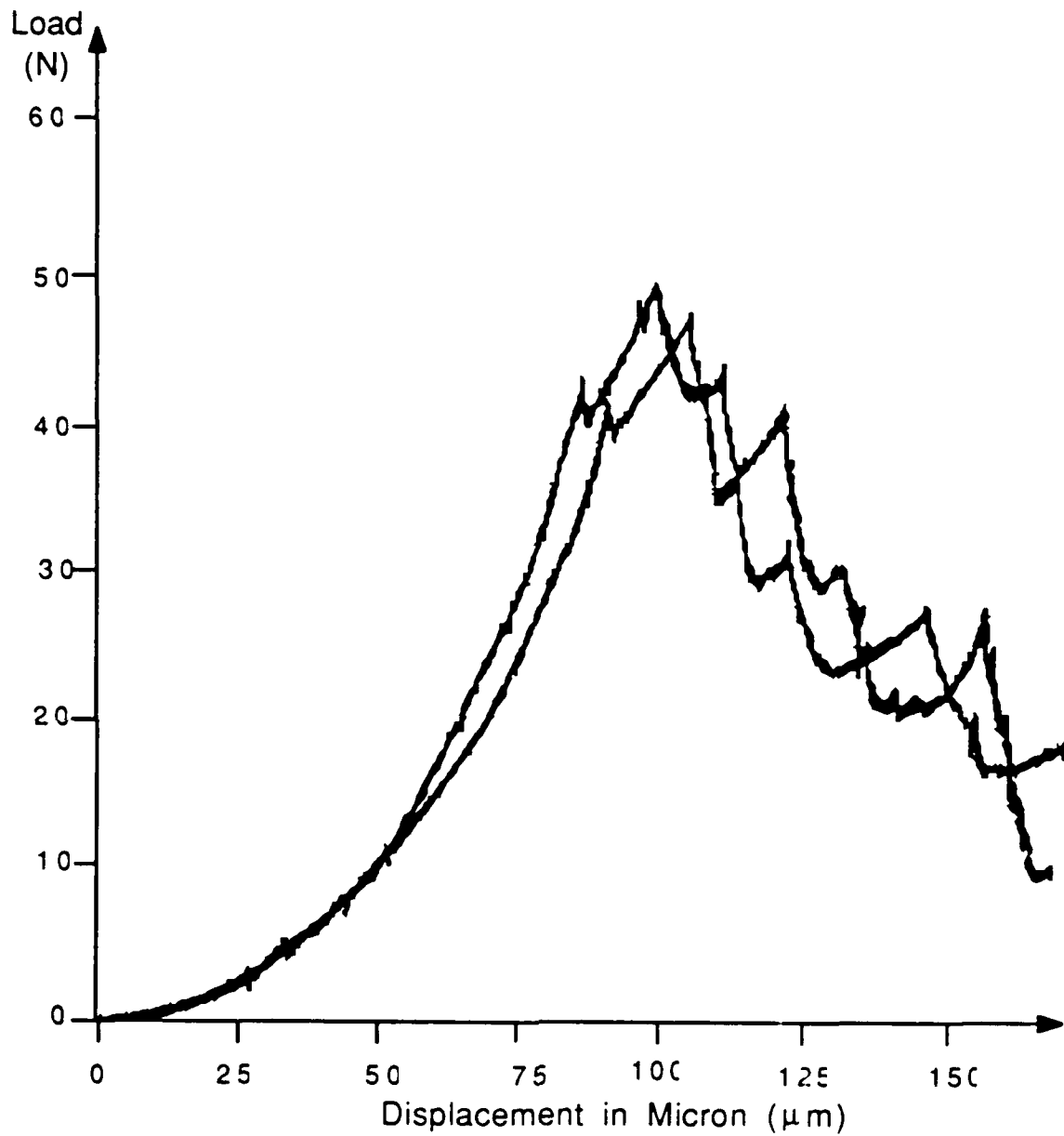


FIGURE A18: Load-Displacement Curves for 15 Vol.% Silar SiC Whisker/Aluminum Oxide Matrix Composite at High Temperature (1000 Degree Celsius) with an Angle of 45 Degree at the Base of the Chevron Notch.

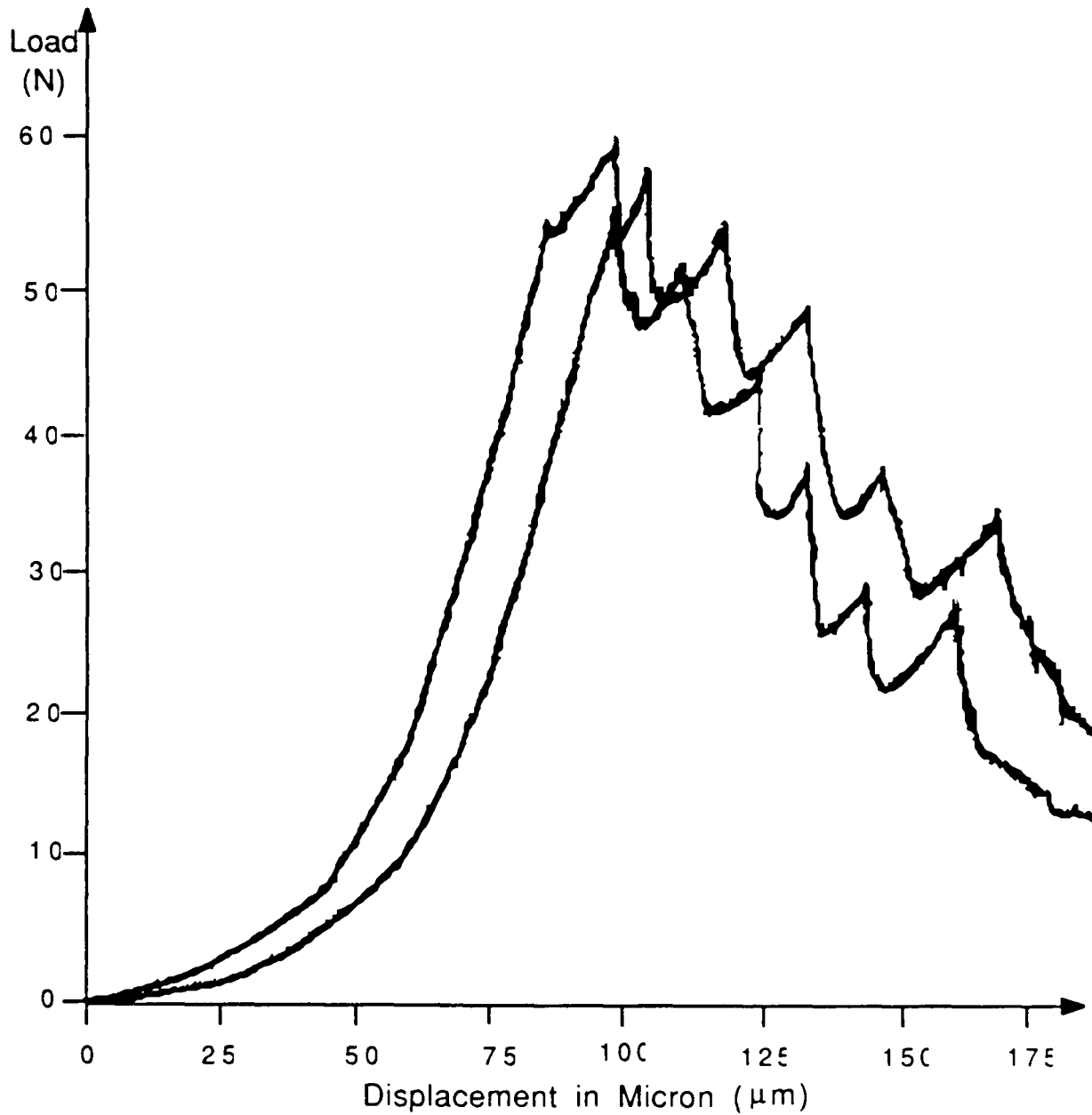


FIGURE A19: Load-Displacement Curves for 30 Vol.% Silar SiC Whisker/Aluminum Oxide Matrix Composite at High Temperature (1000 Degree Celsius) with an Angle of 45 Degree at the Base of the Chevron Notch.

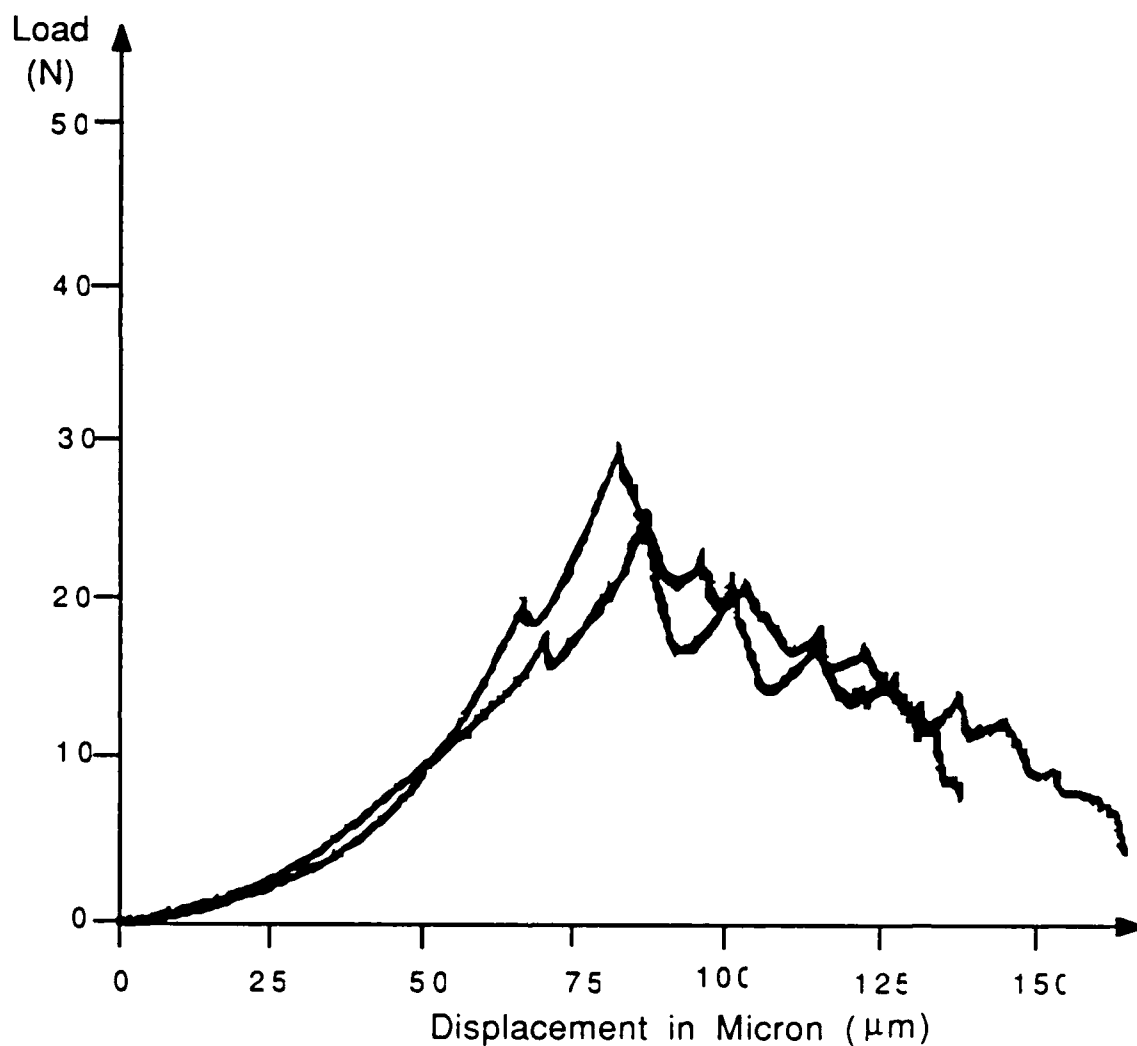


FIGURE A20: Load-Displacement Curves for 45 Vol.% Silar SiC Whisker/Aluminum Oxide Matrix Composite at High Temperature (1000 Degree Celsius) with an Angle of 45 Degree at the Base of the Chevron Notch.

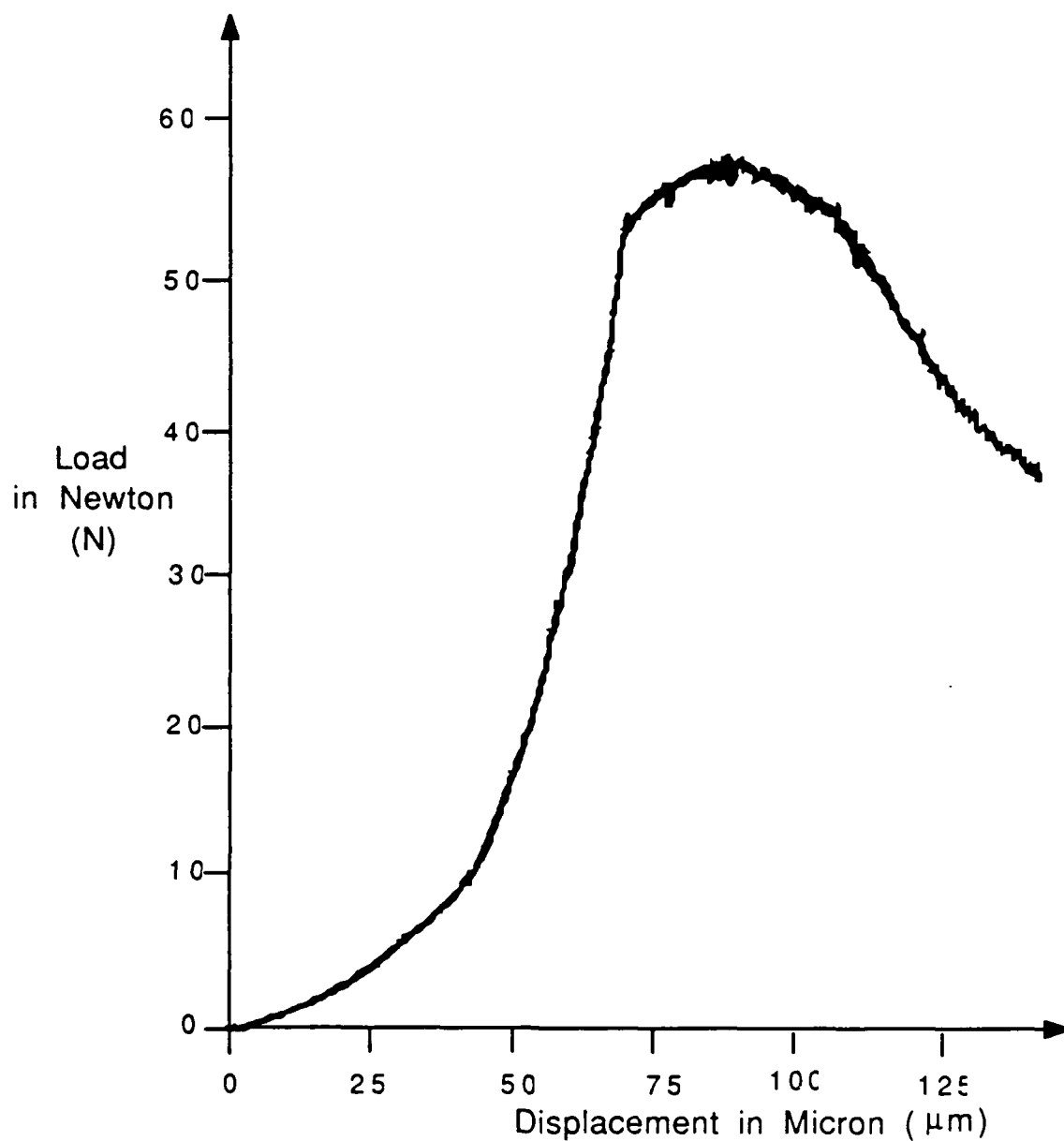


FIGURE A21: Load-Displacement Curves for Monolithic Alumina at High Temperature (1000 Degree Celsius) with an Angle of 45 Degree at the Base of the Chevron Notch.

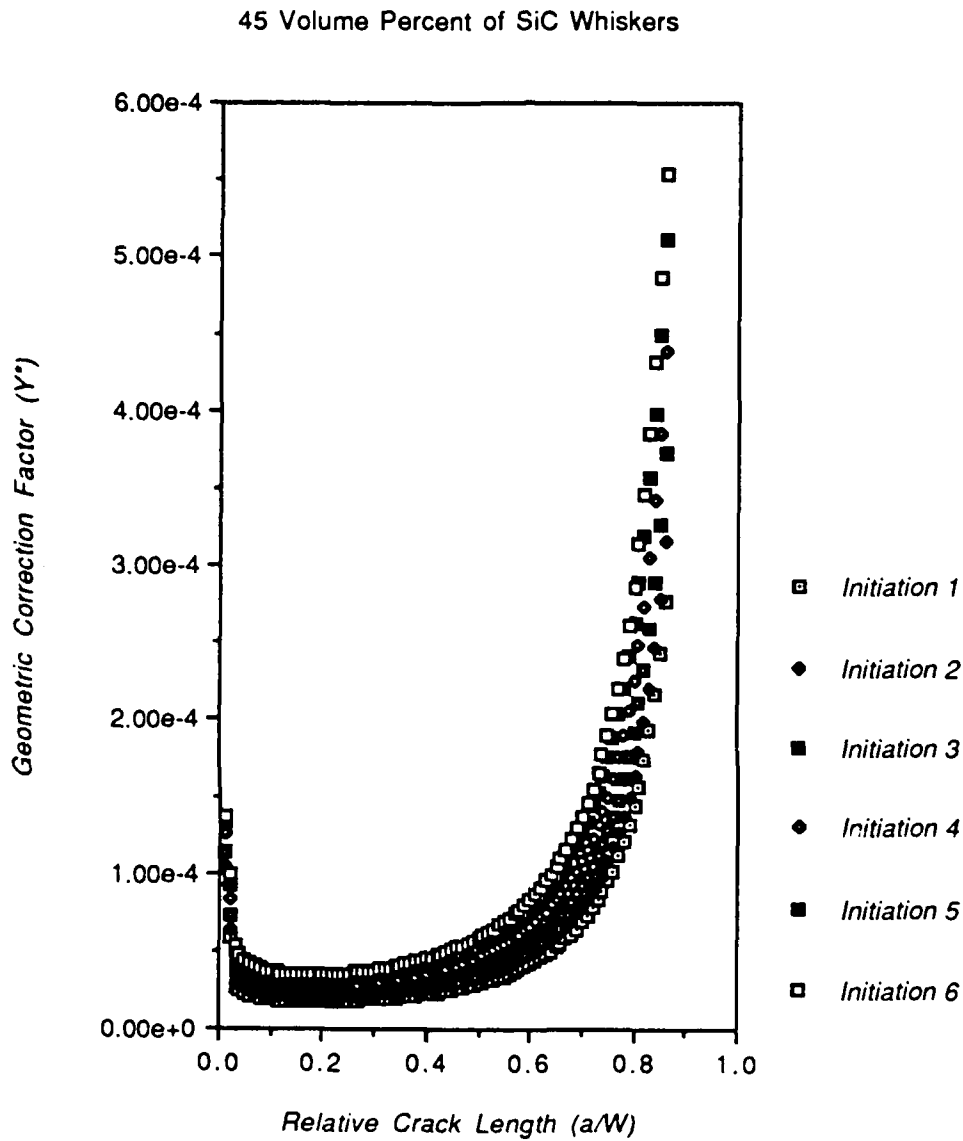


FIGURE B1: Typical Behavior of the Geometric Correction Factor ( $Y^*$ ) for the Chevron Notch Angle of 69.44 Degree in Silar SiC Whisker/ $Al_2O_3$  Matrix Composite.



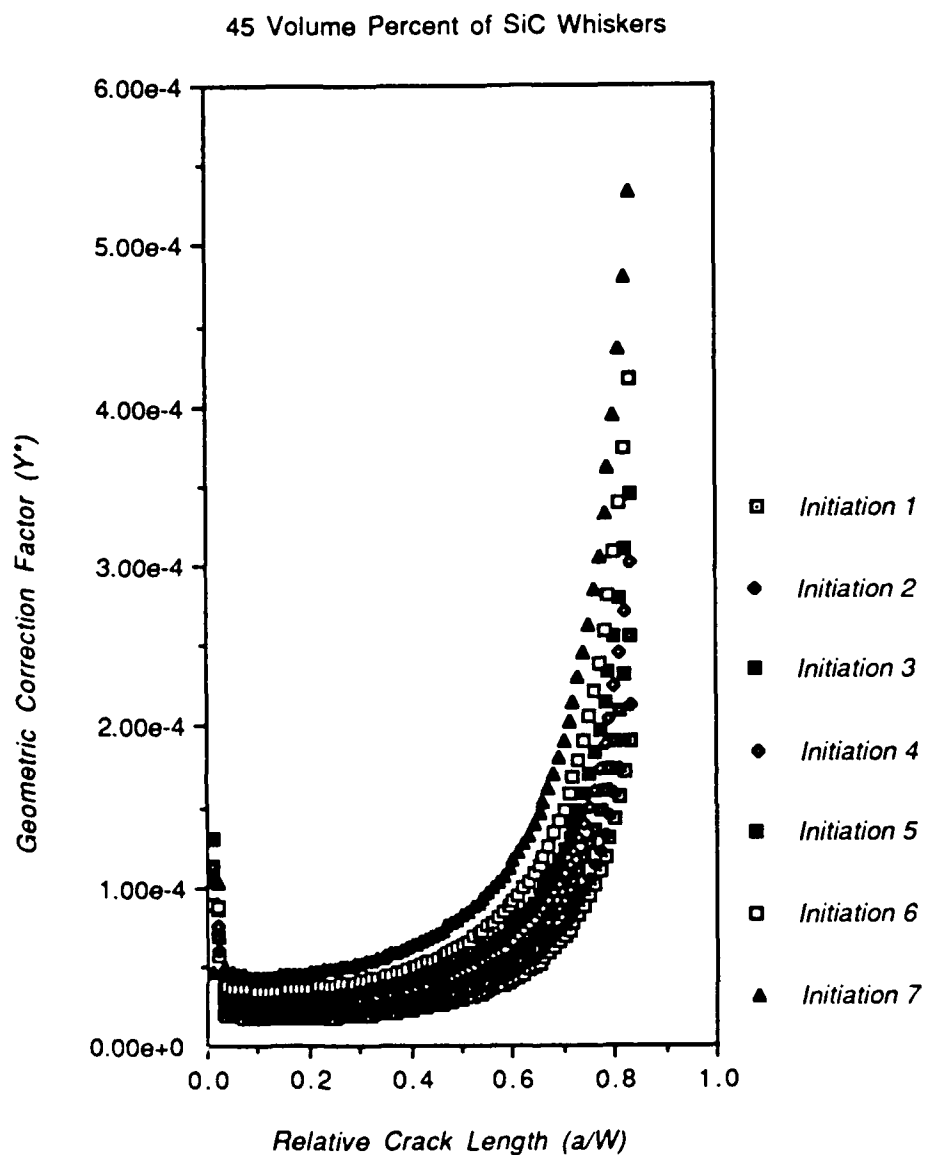


FIGURE B2: Typical Behavior of the Geometric Correction Factor ( $Y^*$ ) for the Chevron Notch Angle of 45 Degree in Silar SiC Whisker/ $Al_2O_3$  Matrix Composite.

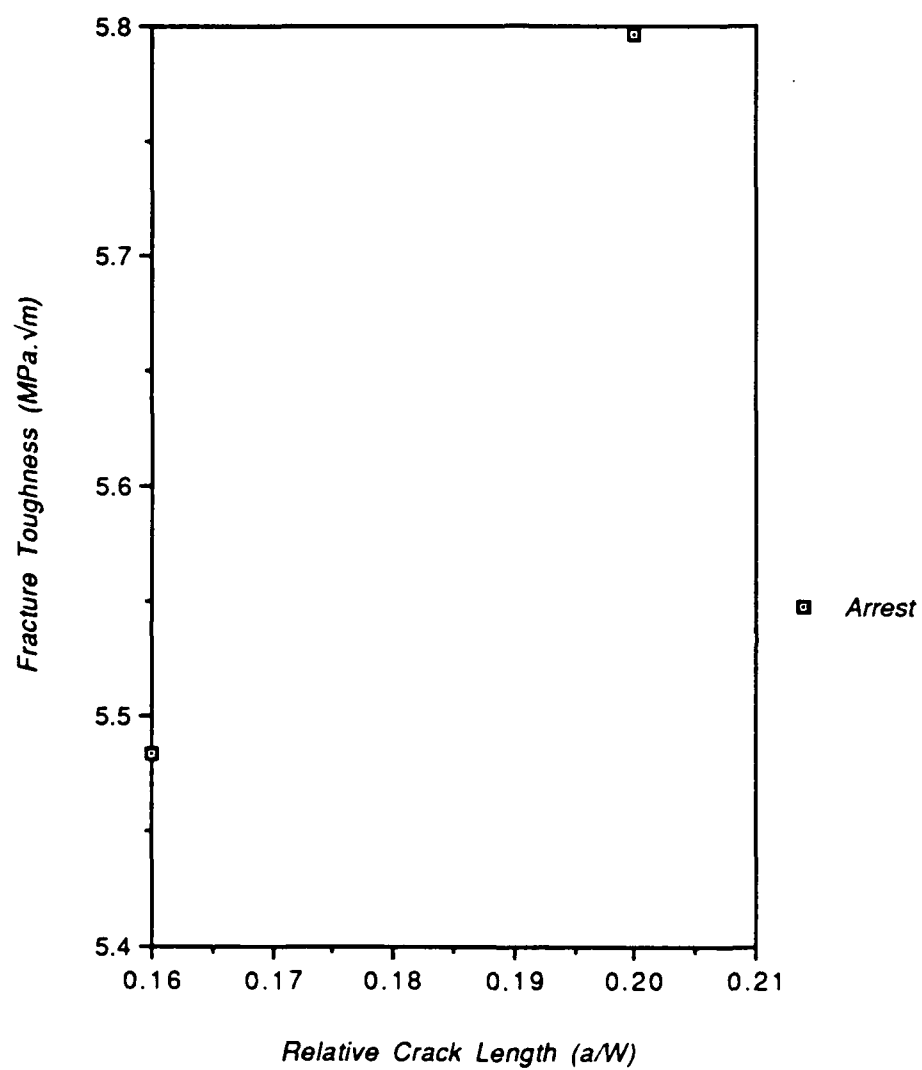


FIGURE C1: R-Curve Behavior in 15 Volume Percent Silar SiC Whisker/ $\text{Al}_2\text{O}_3$  Matrix Composite at Room Temperature with an Angle at the Chevron Notch of 69.44 Degree.

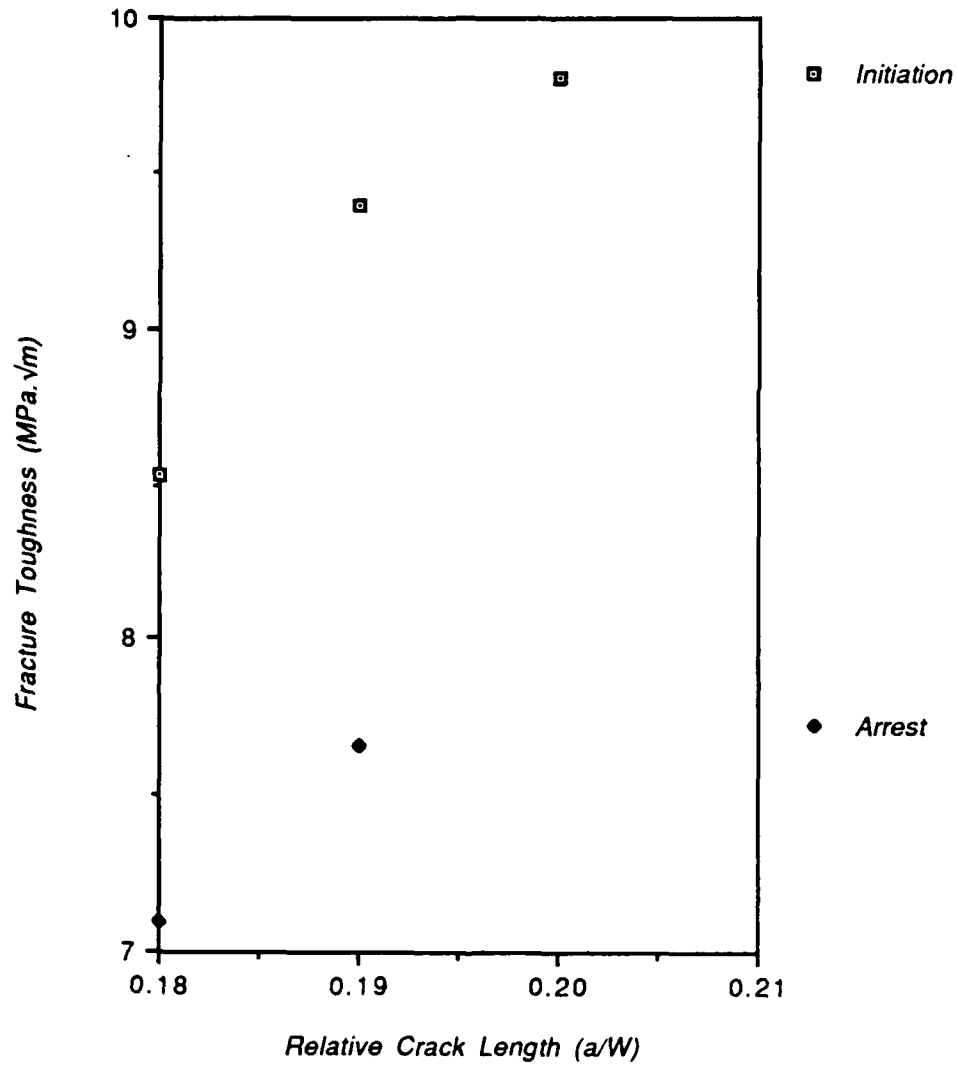


FIGURE C2: R-Curve Behavior in 30 Volume Percent Silar SiC Whisker/ $\text{Al}_2\text{O}_3$  Matrix Composite at Room Temperature with an Angle at the Chevron Notch of 69.44 Degree.

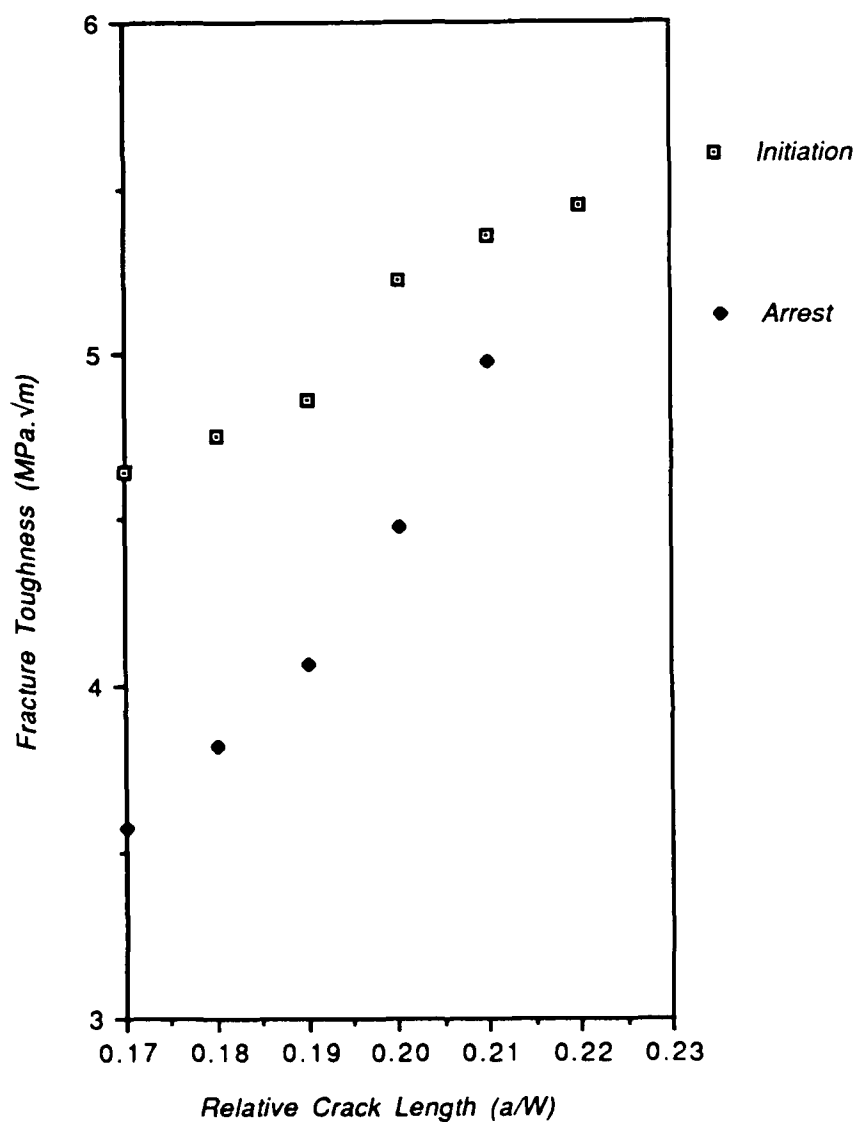


FIGURE C3: R-Curve Behavior in 45 Volume Percent SiC Silar Whisker/ $\text{Al}_2\text{O}_3$  Matrix Composite at Room Temperature with an Angle at the Chevron Notch of 69.44 Degree.

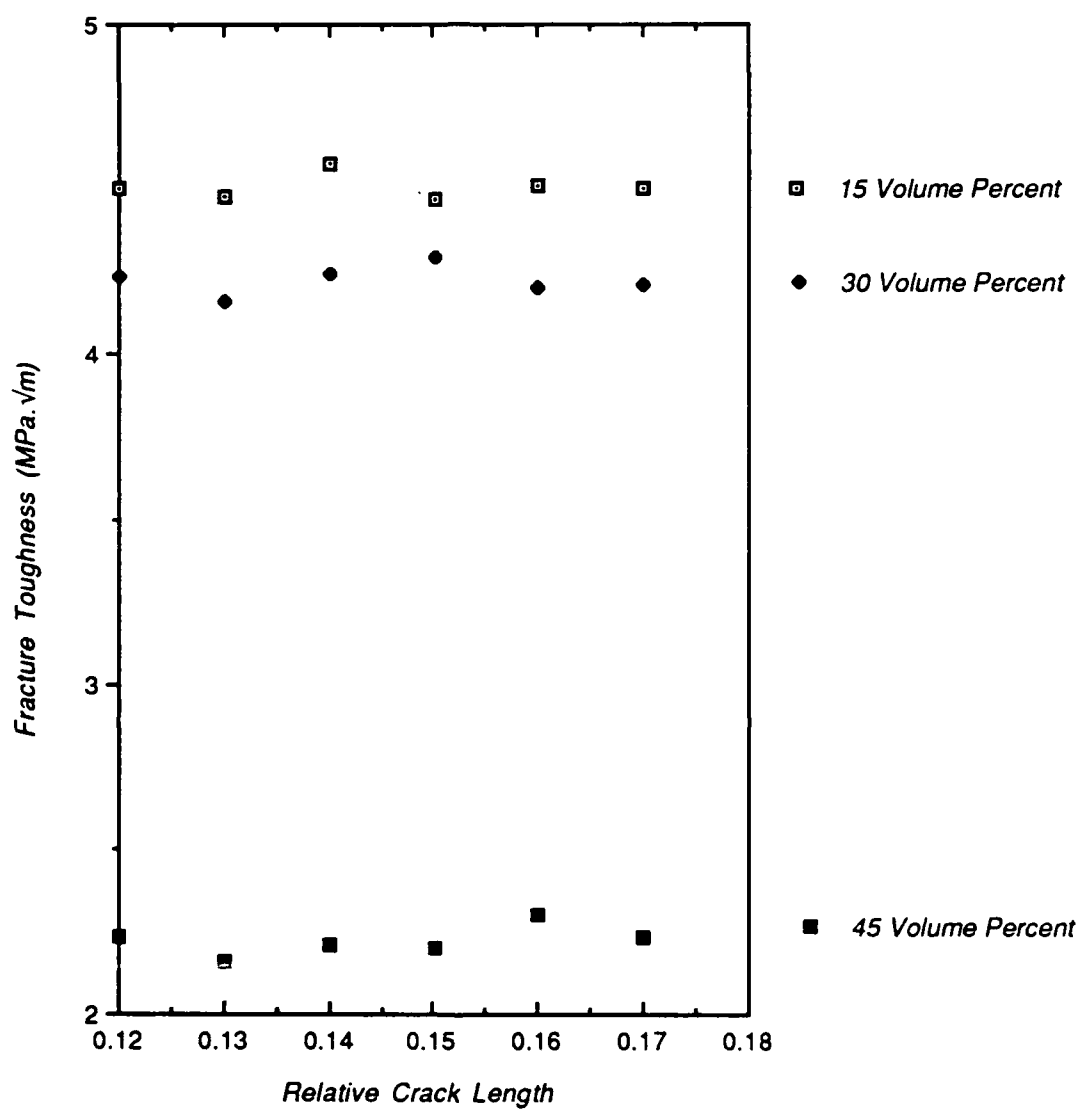


FIGURE C4: R-Curve Behavior in Tateho SiC Whisker/ $\text{Al}_2\text{O}_3$  Matrix Composite at Room Temperature with an Angle at the Chevron Notch of 45 Degree.

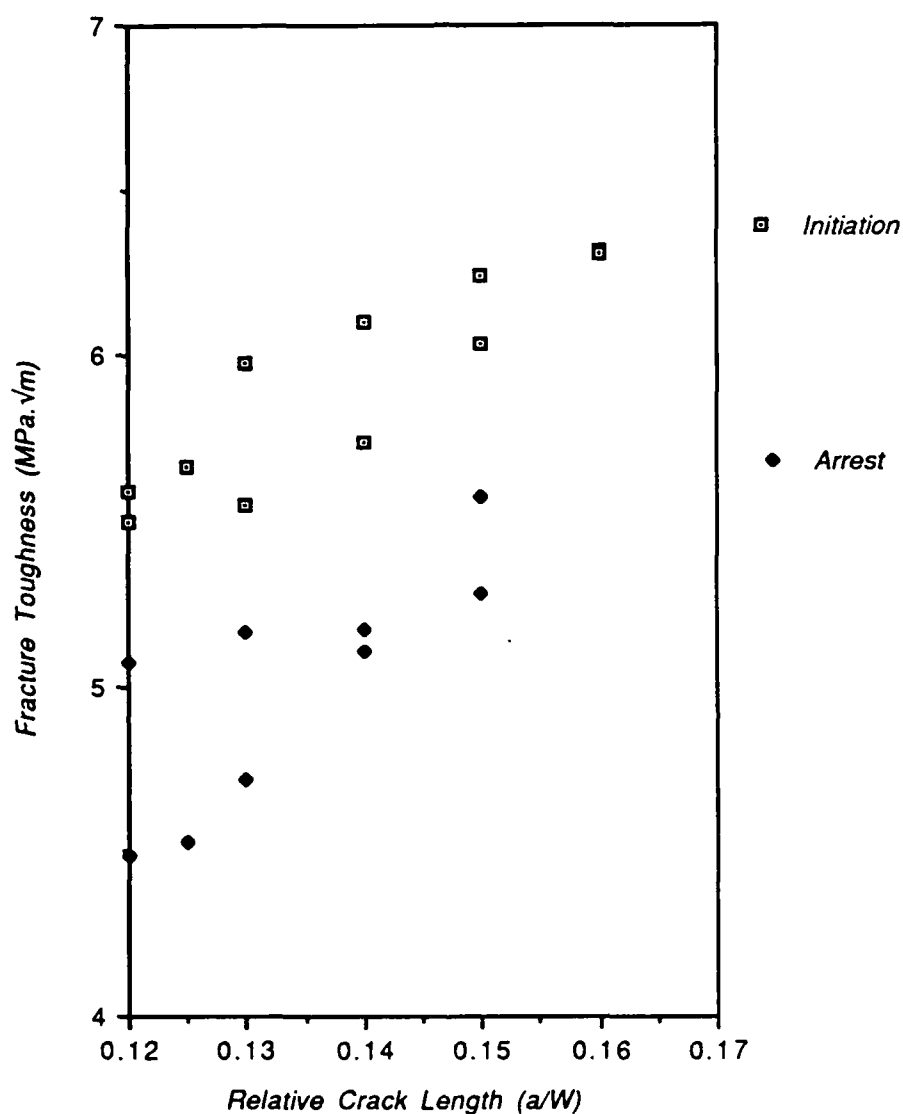


FIGURE C5: R-Curve Behavior in Silar 15 Volume Percent SiC Silar Whisker/ $\text{Al}_2\text{O}_3$  Matrix Composite at Room Temperature with an Angle at the Chevron Notch of 45 Degree.

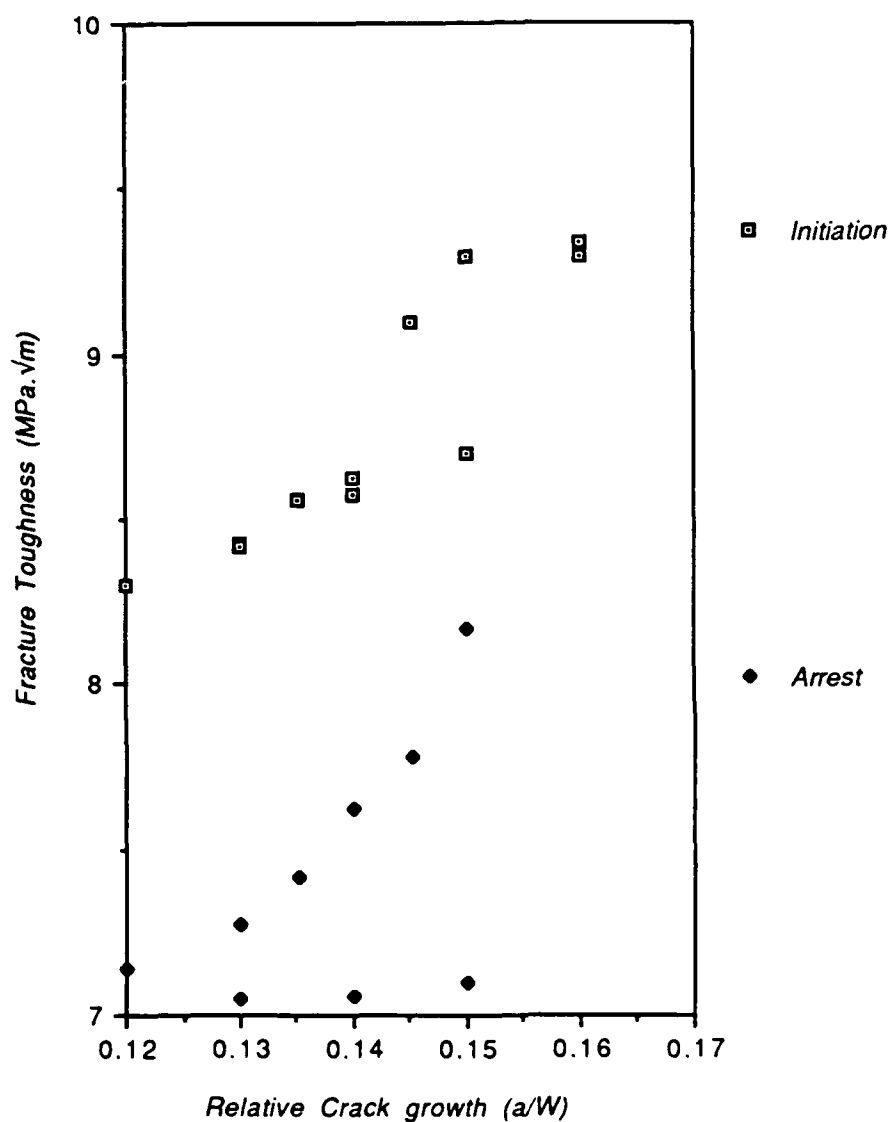


FIGURE C6: R-Curve Behavior in Silar 30 Volume Percent SiC Silar Whisker/ $\text{Al}_2\text{O}_3$  Matrix Composite at Room Temperature with an Angle at the Chevron Notch of 45 Degree.



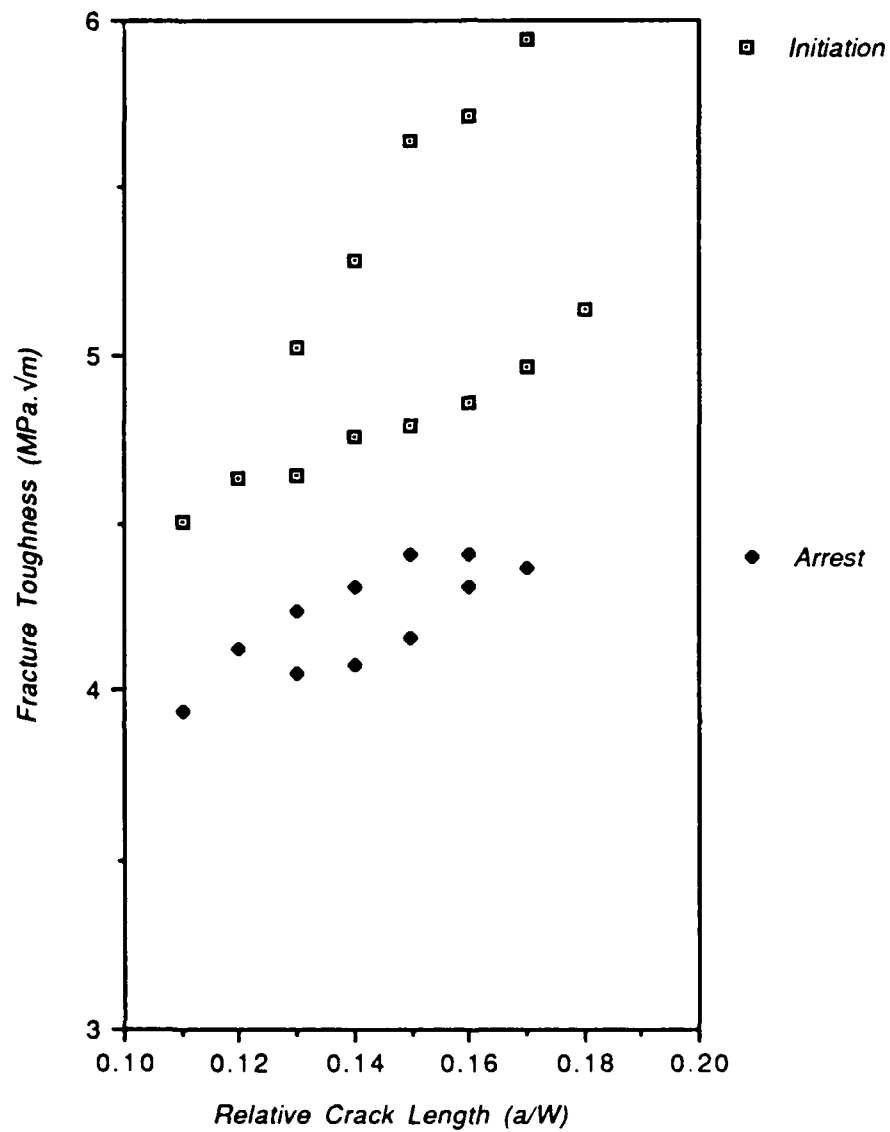


FIGURE C7: R-Curve Behavior in Silar 45 Volume Percent SiC Silar Whisker/ $\text{Al}_2\text{O}_3$  Matrix Composite at Room Temperature with an Angle at the Chevron Notch of 45 Degree.

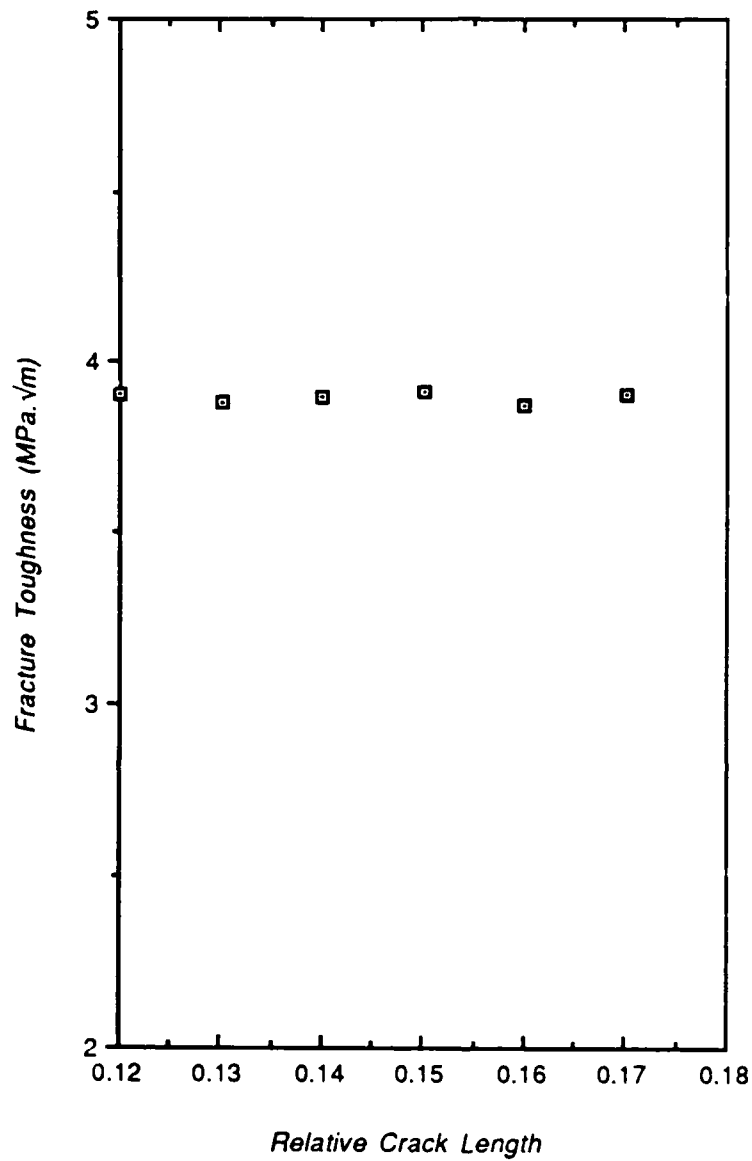


FIGURE C8: R-Curve Behavior in Monolithic  $\text{Al}_2\text{O}_3$  at Room Temperature with an Angle at the Chevron Notch of 45 Degree.

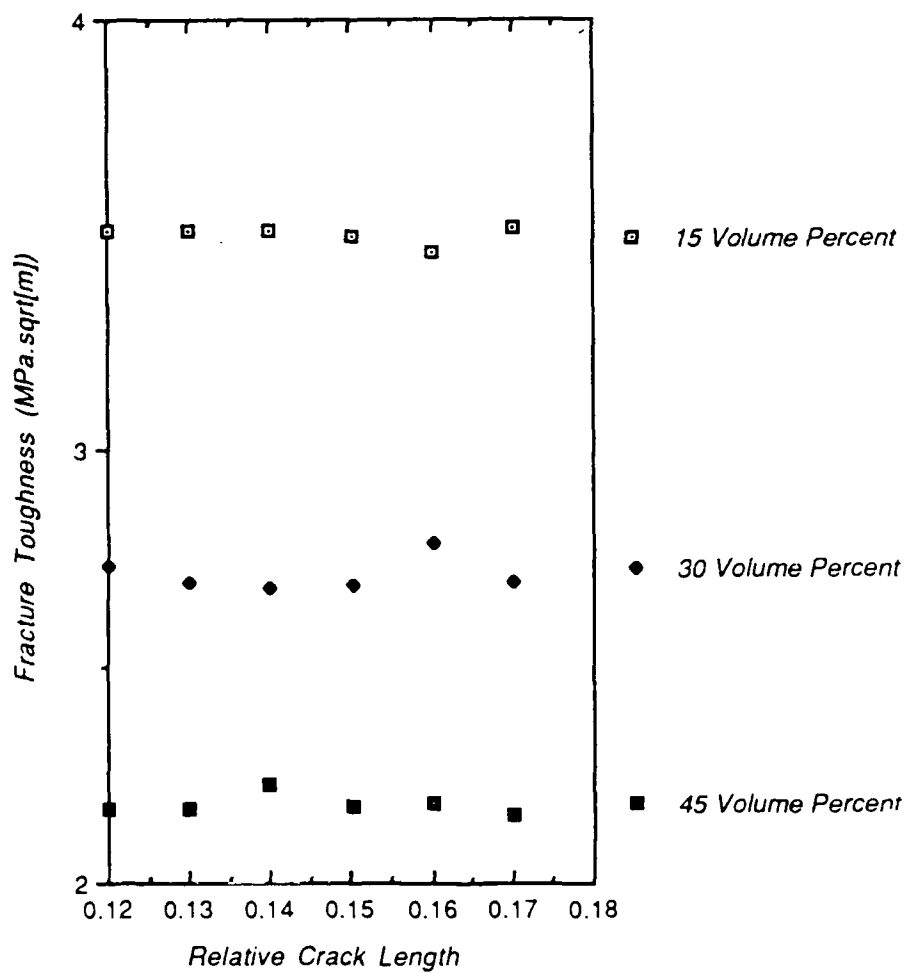


FIGURE C9: R-Curve Behavior in Tateho SiC Whisker/ $\text{Al}_2\text{O}_3$  Matrix Composite at High Temperature ( $1000^\circ\text{C}$ ) with an Angle at the Chevron Notch of 45 Degree.

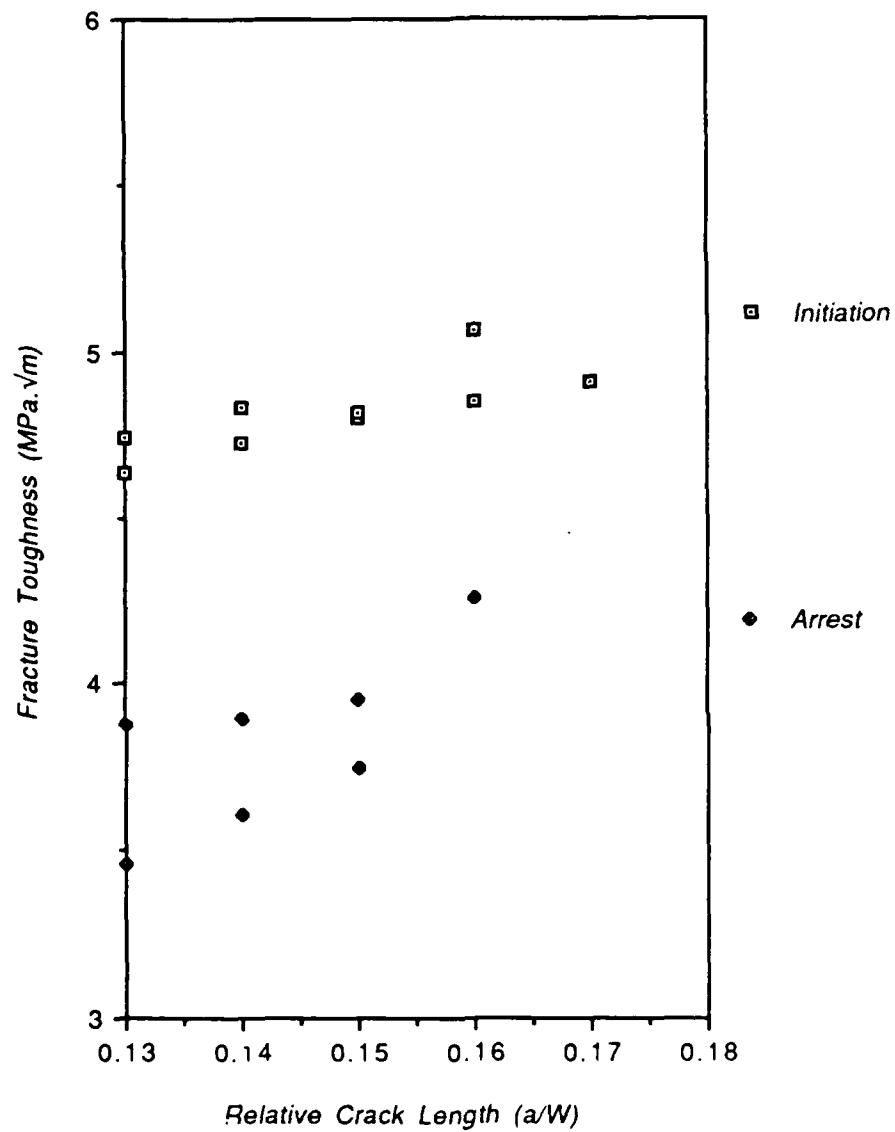


FIGURE C10: R-Curve Behavior in Silar 15 Volume Percent SiC Silar Whisker/ $\text{Al}_2\text{O}_3$  Matrix Composite at High Temperature ( $1000^\circ\text{C}$ ) with an Angle at the Chevron Notch of 45 Degree.

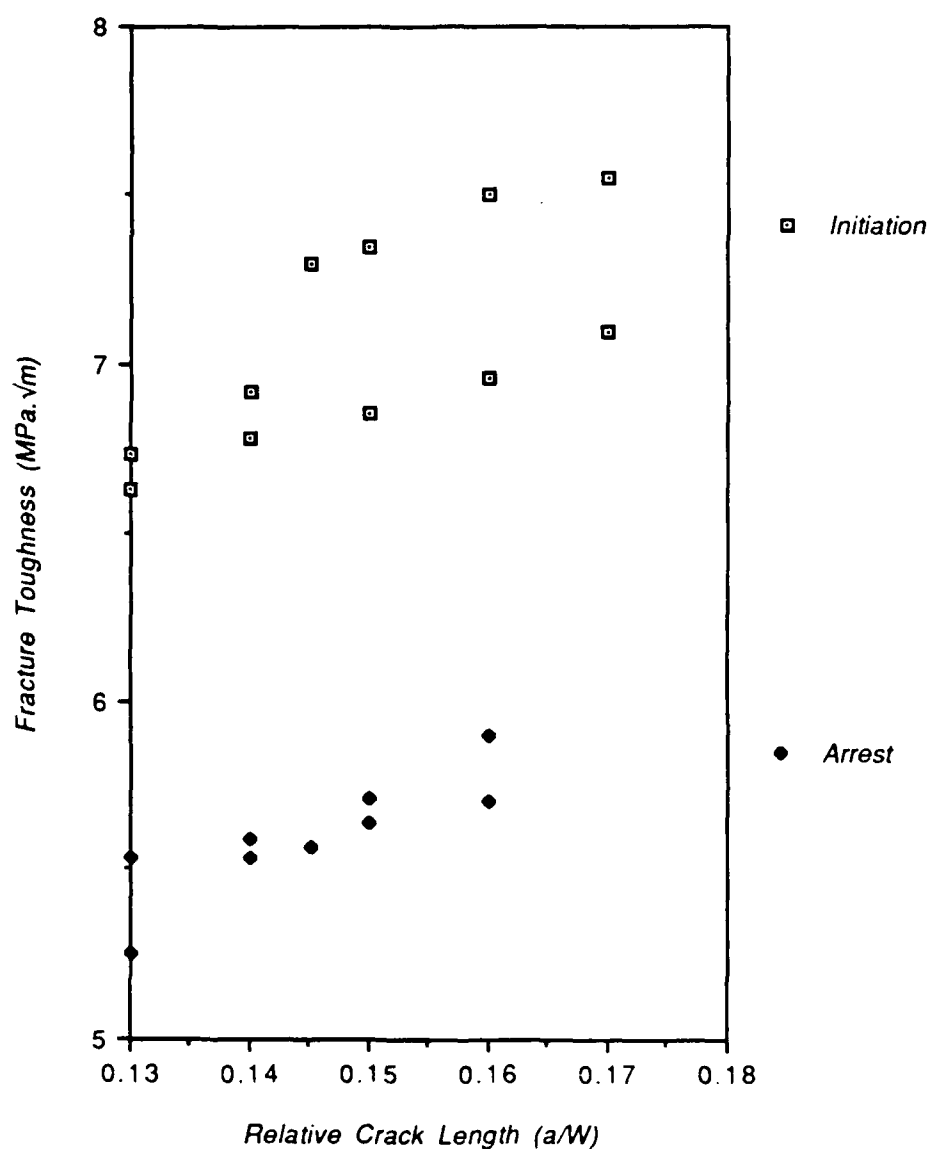


FIGURE C11: R-Curve Behavior in Silar 30 Volume Percent SiC Silar Whisker/ $\text{Al}_2\text{O}_3$  Matrix Composite at High Temperature ( $1000^\circ\text{C}$ ) with an Angle at the Chevron Notch of 45 Degree.

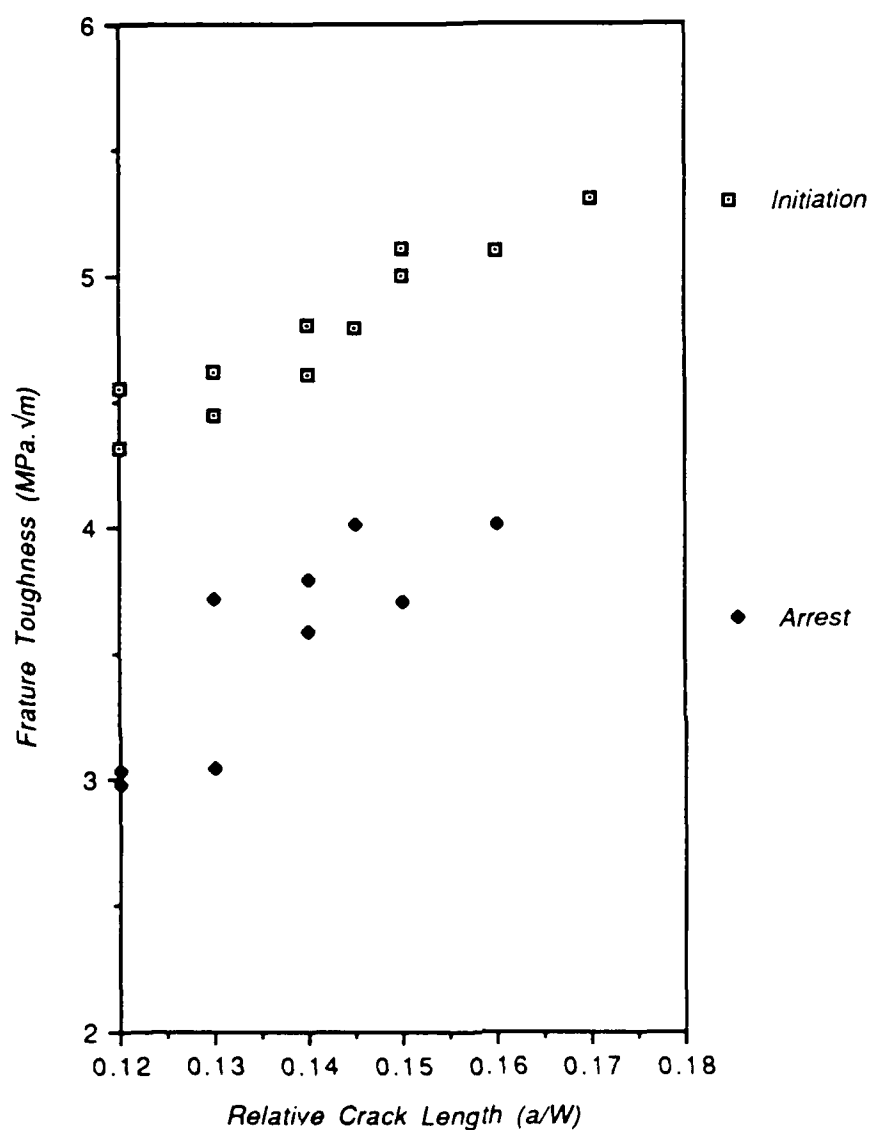


FIGURE C12: R-Curve Behavior in Silar 45 Volume Percent SiC Silar Whisker/ $\text{Al}_2\text{O}_3$  Matrix Composite at High Temperature ( $1000^\circ\text{C}$ ) with an Angle at the Chevron Notch of 45 Degree.

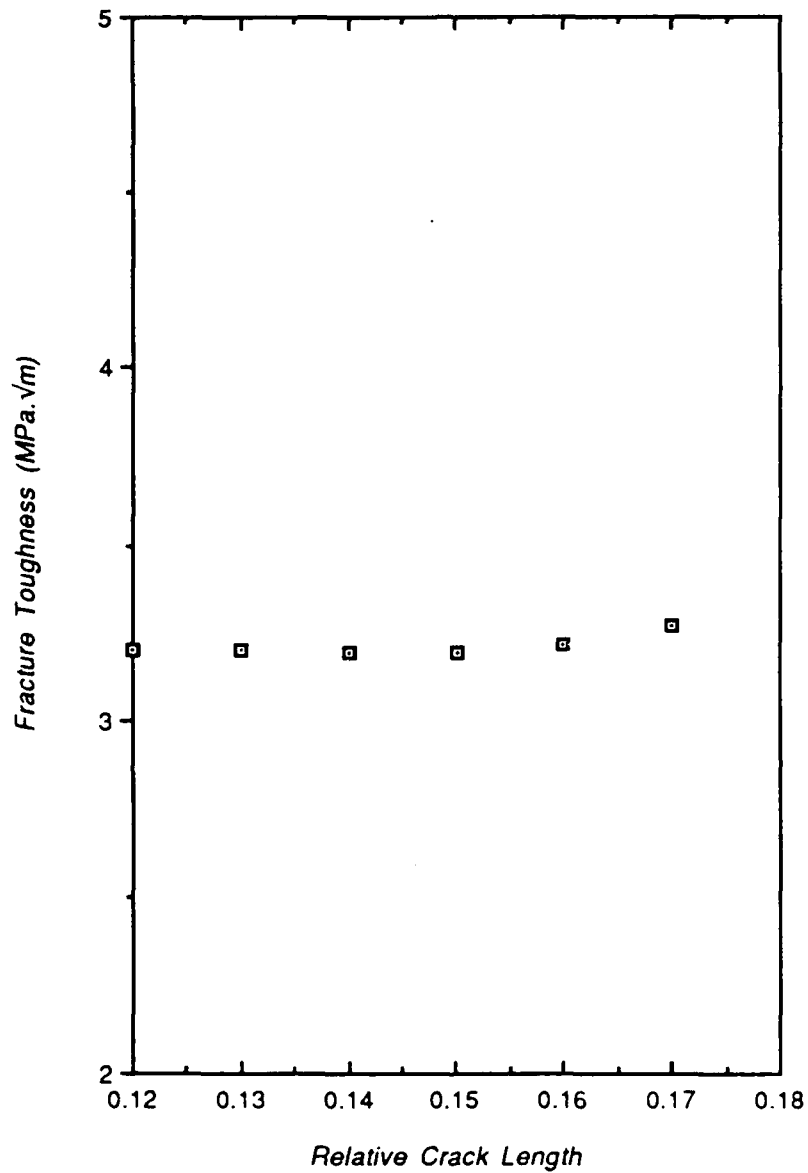


FIGURE C13: R-Curve Behavior in Monolithic  $\text{Al}_2\text{O}_3$  at High Temperature ( $1000^\circ\text{C}$ ) with an Angle at the Chevron Notch of 45 Degree.